Materials Advances



REVIEW

View Article Online
View Journal | View Issue



Cite this: *Mater. Adv.*, 2020, 1, 1506

Catalytic conversion of CO₂ to chemicals and fuels: the collective thermocatalytic/photocatalytic/electrocatalytic approach with graphitic carbon nitride

Subhajyoti Samanta 🕩 * and Rajendra Srivastava 🕩 *

Rapid industrial development and the excessive use of fossil fuels have produced a significantly large volume of CO2 in the atmosphere. The efficient conversion of CO2 to useful chemicals and fuels is an important step towards reducing the concentration of CO2. To overcome the thermodynamic and kinetic barriers involved in CO₂ activation and conversion, an effective heterogeneous catalyst and a suitable form of energy, such as thermal, photochemical, and electrochemical, are necessary. Considering a wide variety of catalytic materials for CO₂ conversion using all forms of energy resources discussed above, earth-abundant carbon materials have exhibited the capability to catalyze the thermal, photo-assisted, and electrochemically mediated conversion of CO2. Among carbon-based materials, graphitic carbon nitride $(q-C_3N_4)$ is an inexpensive and sustainable catalyst that can be effectively used for CO₂ conversion. The chemical reactivity and optoelectronic properties of g-C₃N₄ can be finely tailored for its use as a conventional catalyst or photocatalyst or photoelectrocatalyst. This article aims to summarize the synthetic strategies to prepare various types of g-C₃N₄ materials as conventional catalysts/photocatalysts/electrocatalysts for the improved conversion of CO2 to chemicals and fuels. This article reviews the utilization of CO₂ as a feedstock for chemical and fuel synthesis via insertion, carboxylation, and reduction reactions. Further, an in-depth understanding of the catalytic mechanism of various reactions discussed in this article will help in the design of a new generation of heterogeneous catalysts for CO2 conversion. Special emphasis is placed on the various parameters influencing the photocatalytic and electrocatalytic CO2 reduction. Finally, the underlying challenges and outlook for the future development of catalysts for CO2 conversion to specialty chemicals and fuels are discussed.

Received 10th May 2020, Accepted 15th June 2020

DOI: 10.1039/d0ma00293c

rsc.li/materials-advances

1. Introduction

 ${\rm CO_2}$ is one of the major variable components in the troposphere that significantly influence human life. A large amount of ${\rm CO_2}$ is present in the soil as ${\rm CaCO_3}$. However, only gaseous ${\rm CO_2}$ present in the troposphere is responsible for global warming. The effect of carbon dioxide on Earth is being discussed at every forum and international meeting. A closer look reveals that several activities by millions of living entities (plants, animals, and human beings) have raised the ${\rm CO_2}$ level in the atmosphere by 280 ppm in the last few centuries. However, after the industrial revolution, the ${\rm CO_2}$ level in the atmosphere has risen from 280 ppm to 400 ppm and it is expected to reach up to 500 ppm by the 22nd century, which would raise the mean

Catalysis Research Laboratory, Department of Chemistry, Indian Institute of Technology Ropar, Rupnagar, Punjab-140001, India.

E-mail: subhajyoti.samanta@iitrpr.ac.in, rajendra@iitrpr.ac.in;

temperature of the Earth by 1.9 °C.4 Today, each and every second of our life is dependent on energy resources. The energy dependency can be taken care of with the use of renewable and alternative resources such as wind, water, radioactive, and solar energy, which do not increase the CO2 level in the atmosphere and provide a CO₂ emission-free environment.⁵ In recent times, several alternative energy generation systems, such as fuel cells, are being developed which do not emit CO2.7 However, the H2 required in fuel cells is produced by steam reforming, which produces a large amount of CO2 in the atmosphere.6 Future energy demands and current technologies suggest that it is a long journey and by that time a significant amount of CO₂ will be released into the atmosphere. If the CO₂ concentration increases beyond 600 ppm it would be difficult for human beings to breathe because it is difficult for the human respiratory system to operate in the presence of a greater concentration of CO₂ even though an excess of O₂ is present in the atmosphere. Thus, there is a high priority in developing strategies to reduce the CO₂ concentration in the environment. This can be achieved via two

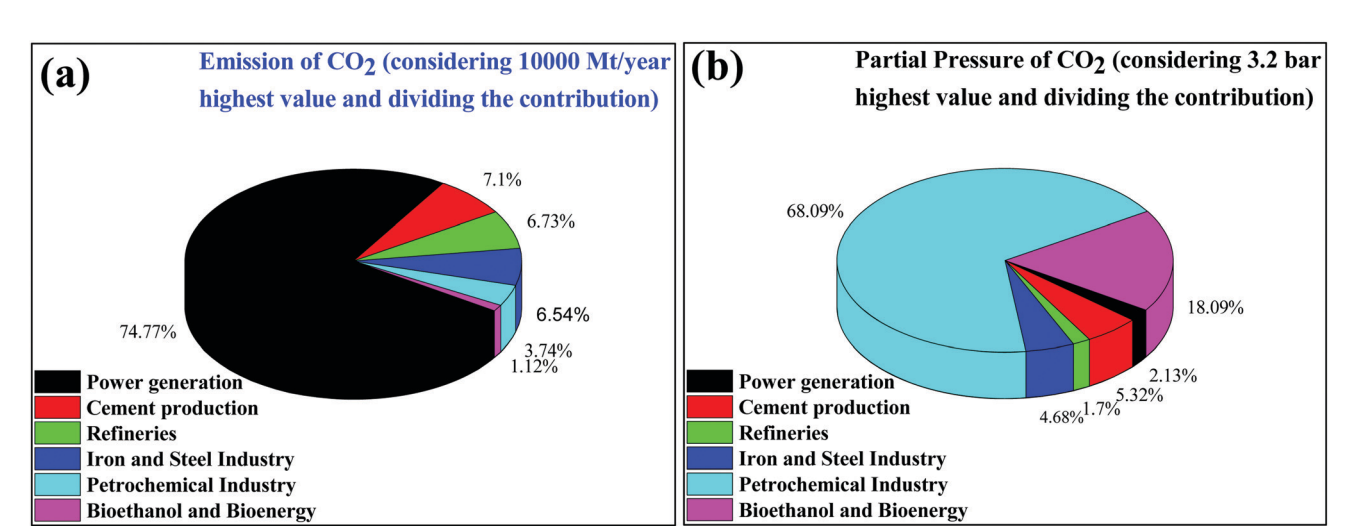


Fig. 1 (a) Emission of CO₂ and (b) partial pressure of CO₂ emitted from different stationary sources.

strategies: (1) CO₂ capture and storage (CCS) and (2) CO₂ capture and utilization (CCU) to useful chemicals and fuels. This article is focused on the CO₂ conversion to useful chemicals and fuels; therefore, only a brief discussion is provided for CO₂ capture and storage.

The various types of stationary plants and their corresponding CO₂ emission (amount and partial pressure) are summarized in pie charts (Fig. 1). It is very easy to capture CO₂ from point sources where the CO₂ concentration is high but it is very difficult to capture CO₂ from low concentration sites, such as on city roads

or houses where the concentration ranges fall at the ppm level.8 Besides being the most desirable task, direct CO₂ capture and storage are undoubtedly challenging. 9,10 In general, liquid CO2 scrubbers and metal oxides are used to absorb CO2 from flue gases. 11-20 Aqueous amine based liquid CO2 scrubbers are commonly used but their associated energy consumption and cost remain a constraint for further development. Similarly, solid materials such as alkali metal oxides, layered double hydroxides, solid amines, etc. are widely explored materials for CO₂ adsorption.¹⁴ However, CO₂ absorption using the CO₂



Subhajvoti Samanta

Mr Subhajyoti Samanta received Science Master of Chemistry from Guru Ghasidas Central University, Chhattisgarh, India in 2011 after completion of his bachelor's degree with honors in Chemistry from Vidyasagar University, West Bengal, India in 2009. Since July 2014, he has been working under the supervision of Dr Rajendra Srivastava in the Department of Chemistry at the Indian Institute of Technology Ropar (IIT Ropar), Punjab, India.

Prior to joining his Ph.D. research, he had also worked as a project Junior Research Fellow at CSIR-IIMT, Bhubaneswar, India (June 2013-January 2014). His research concentration circumvents the area of nano-engineering metal oxides and their composites with carbon materials for their applications in heterogeneous catalysis. He has particularly developed materials for a variety of photocatalytic oxidation reactions, CO2 reduction, and water oxidation by both electrocatalytic and photocatalytic methods. He has published 15 research articles in the Journals of International repute to his credit. He has also been recognized as a young scientist and participated in the Global Young Scientist Summit-2020, Singapore.



Rajendra Srivastava

Dr Rajendra Srivastava joined the Department of Chemistry, IIT Ropar in 2009 as an Assistant Professor, headed the department from March 2015 to May 2018, and is currently working as an Associate Professor. He acquired his Ph.D. degree from CSIR-National Chemical Laboratory, Pune, India where his doctoral work won him the best thesis award of 2006, conferred by the Catalysis Society of Afterward, he worked as a

postdoctoral research fellow in KAIST, South Korea (2005-2007) and as a JSPS fellow in the Hokkaido University, Japan (2007-2009). He received the NASI-SCOPUS Young Scientist Award 2017, The Catalysis Society of India Young Scientist Award 2018, and Midcarrier Faculty Research and Innovation Award 2019 by IIT Ropar. His fields of interest include designing and synthesis of nanostructured functional materials for catalytic applications, including electrocatalysis (actuators, sensors, supercapacitors and energy harvesters), and photocatalysis. He has published more than 130 peer-reviewed original research articles in reputed international journals and has filed 8 patents.

scrubbers and solid materials discussed above is energetically reversible due to the strong bonding of CO₂ to these materials. Several types of nanoporous materials based on zeolites, 17,18 metal-organic frameworks, 17-19 and carbon 20,21 have been developed for this purpose. All of those above-mentioned materials have functional amines and metal sites for the efficient adsorption of CO2 over other gases present in flue gas. Apart from tuning the chemical properties, tailoring textural properties such as the surface area, pore size and porous architecture can improve the CO2 adsorption capabilities. It is noteworthy that materials having a pore size greater than 0.33 nm and lower than 0.35 nm would be ideal for CO_2 adsorption over other gases present in flue gas (the kinetic diameters of CO2, O2, and N2 are 0.33 nm, 0.345 nm, and 0.36 nm, respectively).²² However, such a fine porous material with specific requirements is yet to be developed. Therefore, high surface area materials having dense CO2 adsorption sites with pore sizes in the range of 0.3 to 2 nm are being prepared. 20,23,24 Thus the direct capture of CO2 from the air (in which the O₂/CO₂ ratio is more than 500 or even more) is very demanding but challenging for research scientists and engineers. However, plants do this job very efficiently when the present CO₂ level is <400 ppm. Plants abstract CO₂ from the atmosphere and convert it to carbohydrate with the aid of

Materials Advances

sunlight and grow and liberate O2. The most efficient strategy to reduce the concentration of CO₂ in the atmosphere is to convert CO₂ to useful chemicals and fuels. CO2 is a thermodynamically inert molecule with a high C=O bond dissociation energy of 750 kJ mol⁻¹ which is much higher than the C-O bond (327 kJ mol⁻¹) and even higher than the C-C (336 kJ mol⁻¹) and C-H (441 kJ mol⁻¹) bonds.²⁵ Due to such high stability, it is difficult to transform CO₂ into useful chemicals. The energy gap between its highest occupied molecular orbital and lowest unoccupied molecular orbital is 13.7 eV and the electron affinity of CO_2 is $(-0.6 \pm 0.2 \text{ eV})$, which leads to a very negative redox potential for one-electron transfer $CO_2 + e^- \rightarrow CO_2^- (E_{redox}^0 = -1.90 \text{ eV } \nu s. \text{ NHE}).^{26,27} \text{ Such a high}$ energy requirement for electron transfer to generate active species for CO2 conversion makes photocatalytic and electrocatalytic processes highly challenging tasks. Due to such a high energy requirement, only a few chemicals have been commercialized, which utilizes a large amount of CO2 to give useful chemicals such as urea, methanol, salicylic acid, cyclic carbonates, and dimethyl carbonate (Scheme 1). Synthesis of urea and cyclic urea is not a 100% atom economic process because water is formed as a by-product. In an atom economic process, the total number of atoms present in the reactants is incorporated into the product. Synthesis of cyclic carbonates takes place by an insertion reaction in which CO2 is inserted into a three-membered epoxide ring to produce a five-membered cyclic carbonate via a 100% atom economic process. 28,29 Dimethyl carbonate (DMC), a solvent, can be produced by the reaction of methanol and CO₂. 30,31 DMC reacts with phenol using a Pb(OPh)₂ catalyst to produce diphenyl carbonate (DPC). Then DPC reacts with bisphenol-A to produce a polycarbonate via a melt polymerization method (Scheme 1).32 Salicylic acid is manufactured

by the reaction of phenol and CO₂ in a strongly basic medium.³³ Another bulk chemical is methanol, which is produced annually at a rate of 100 million tons by utilizing 2 million tons of CO₂³⁴ (Scheme 1). Industrial processes for chemical synthesis using CO2 as a reactant are operated at high temperature and pressure due to the thermodynamic stability and inertness of CO₂. Such reactions can be catalyzed under mild conditions if the CO2 is efficiently activated. Since CO2 is an acidic molecule, therefore it can be activated using basic catalysts such as alkali and alkaline earth metal-based oxides and hydroxides. Various organic amines (N-heterocyclics, DBU, guanidine, melamine, phthalocyanine, and porphyrins) and polyamines have also been used in chemical synthesis utilizing CO₂ as the reactant. In general, organic amines are more reactive than inorganic bases and thus various ionic liquids, metal-organic frameworks, silica, and zeolite based materials with functional amine groups have been utilized for chemical synthesis involving CO₂ as a reactant. Nitrogen-containing carbon materials, such as carbon nitrides, are a unique class of materials which can be prepared with economical nitrogen and carbon-containing precursors. Since these materials have a large nitrogen content, they can be used for CO2 activation and adsorption.

In this review, we will present the advances, challenges, and prospects of carbon nitride based catalysts, photocatalysts, and electrocatalysts in CO2 conversion to chemicals and fuels. After a brief introduction to CO₂ conversion, the requirements of CO2 storage and conversion, the industrial process for CO2 to chemicals, and the types of materials required for CO2 activation and conversion are described in Section 1. Sections 2-6 focus on carbon nitride-based catalysts in the conventional catalytic conversion of CO₂ to chemicals and photocatalytic and electrocatalytic conversion of CO2 to C1 fuels. Section 2 presents a brief description of nitrogen-containing carbonbased materials, types of carbon nitride, and the structural elucidation of g-C₃N₄ for catalytic applications. Section 3 deals with the synthesis strategy adopted for the preparation of g-C₃N₄ for improved catalysis and photocatalysis involving CO2 as a reactant. Sections 4 and 5 provide detailed information about photocatalytic and electrocatalytic CO2 conversion to C₁ fuels, respectively, their basic concepts, the influence of various parameters influencing the CO₂ conversion and C₁ fuel selectivity, deep insight into the reaction mechanisms via in situ characterization techniques and product identification, catalytic activity assessment and result presentation, and the experimental set-up required for photocatalytic and electrocatalytic measurements. Finally, this review will be concluded with a summary, underlying challenges, and opportunities for the future development of catalysts for CO2 conversion to chemicals and fuels.

This focused review aims to concisely cover almost all the important points, starting from the requirements of CO_2 conversion, fundamentals of CO_2 activation, strategies adopted for $g\text{-}C_3N_4$ preparation for improved CO_2 conversion, structure elucidation of $g\text{-}C_3N_4$, and structure–activity relationship, followed by critical operational parameters for collective 'thermo-photo-electro'-chemical CO_2 conversion focusing on the $g\text{-}C_3N_4$ catalyst,

➤ NH₂COONH₄ $NH_2CONH_2 + H_2O$ (Willion Tool)/(Year) 100 100 80 60 40 Ammonium carbamate Urea Produced Utilized 20 Cyclic urea **(2)** 80 70 70 60 50 40 30 Cyclic carbonate Produced Utilized 10 dialkyl carbonate (R = -CH₃, -C₂H₅, -C₃H₅, -C₆H₅) Bisphenol-A carbonate Produced (3)Salicylic acid Carbon dioxide Produced Utilized Salicylic acid 100 (4) (Million Ton)/(Year) 09 08 08 08 08 08 **→** CH₃OH + H₂O Methanol

Scheme 1 CO₂ based commercial processes and amount of CO₂ utilized vs. product formed in the given process

which is not available in a single article hitherto reported in the literature.

2. Carbon nitride, a versatile material for CO₂ adsorption and conversion: structural elucidation for catalysis

Among porous materials, carbon materials have a high surface area, tunable porosity, hydrophobicity for CO2 adsorption under hydrated conditions, high thermal and chemical stability, and functional ability.35-37 Activated carbon is the most economical and widely available carbon material having micropores,

mesopores, and macropores.³⁸ Due to the porous architecture and high surface area, it can significantly adsorb large amounts of CO₂ by the physisorption process but it finds difficulty in the activation and utilization of CO2 in chemical synthesis due to the inability to chemisorb and activate CO2. 39 Biomass pyrolysis and KOH activation can produce high surface area activated carbon, suitable for CO₂ physisorption. 40 N-Doped microporous carbon prepared with coconut shell and urea has exhibited high CO2 adsorption and CO2/N2 selectivity at 1 bar, confirming that N-doping has improved the CO₂ adsorption. 41 Similar to inorganic porous materials, sol-gel methods have been applied for the synthesis of porous carbon materials in water and/or ethanol medium followed by acid activation

Produced

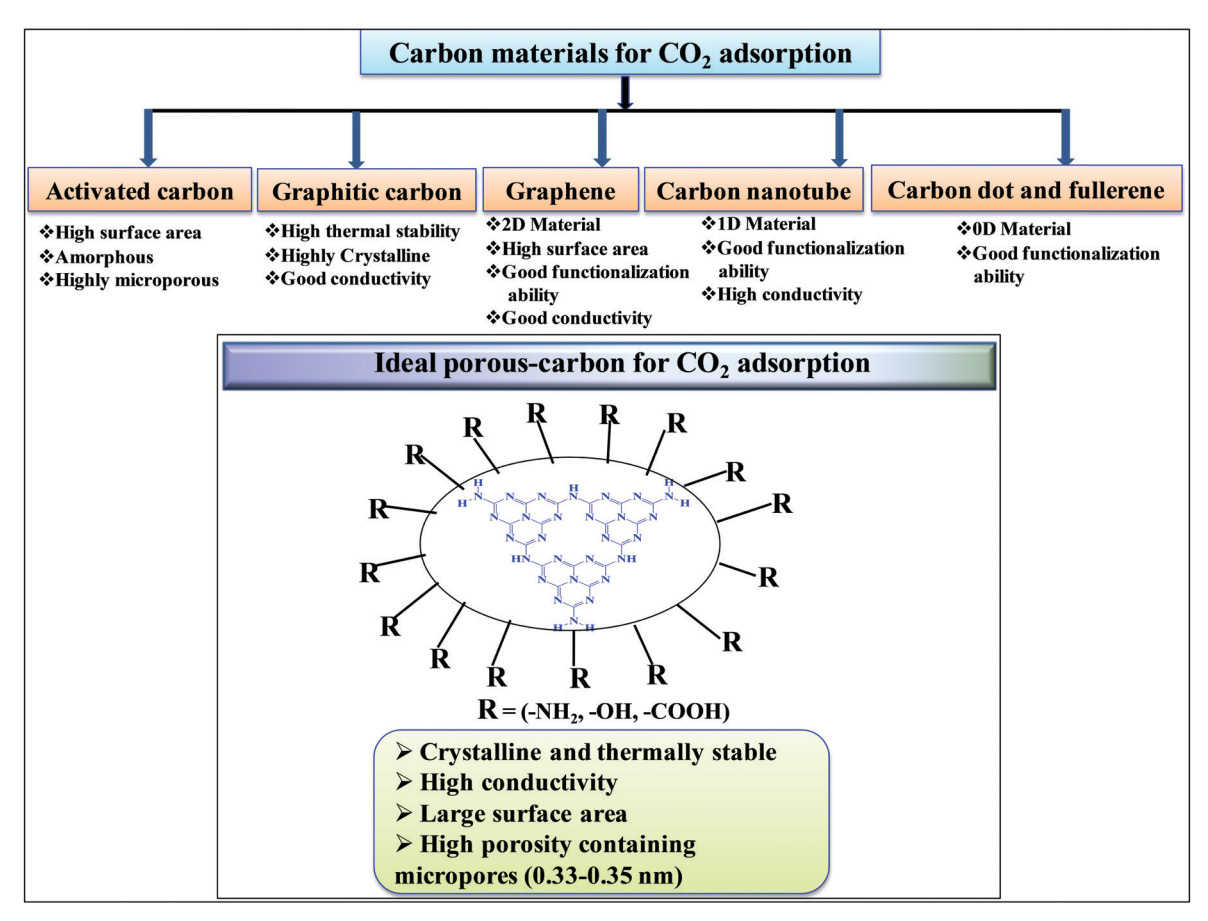
Carbon dioxide

Utilized

Materials Advances Review

leading to the formation of porous carbon with high surface area and pore volume. 42,43 Hydrothermal polymerization is employed to prepare porous carbon materials with higher surface area after chemical activation. 44 The hydrothermal method provides the opportunity to prepare carbon materials with functionalized carbon in the presence of other functional organic compounds. Such functionalized materials (carboxyl rich carbon materials) have exhibited high CO₂ capture performances at 1 bar and under flue gas conditions. 45 Hard template 46 and soft template 47 methods have been developed for the preparation of mesoporous carbon. The carbon materials discussed above are amorphous porous carbon. It is also possible to synthesize crystalline carbon materials with different allotropy. 0D carbon dots and fullerenes, 1D carbon nanotubes, 2D graphene, and 3D graphite are the various allotropic forms of carbon materials (Scheme 2). In general 3D graphitic carbon can be prepared by heating a carbon precursor at a very high temperature 2000-3000 °C. However, such graphitic carbon possesses very low surface area and porosity. Metal catalyst mediated synthesis produces graphitic carbon at a very low temperature of 700-800 °C with higher surface area and porosity.⁴⁸ Moreover, microwave mediated, metal activated synthesis produces graphitic carbon with very high surface area and porosity. 49 Graphene, carbon nanotubes, and fullerenes have been prepared under varying controlled conditions using a unique vapor deposition method

in the presence and absence of metal catalysts. Due to the high surface area and surface to volume ratio, these materials can be easily functionalized using various amines for the efficient adsorption of CO₂. ^{50,51} These porous carbons have varied surface area, morphology, and porosity and, thus, the extent of CO2 adsorption over these materials varies depending on their tunable textural properties. However, the adsorption and chemisorption capability improves if nitrogen-doped or nitrogencontaining carbon materials are considered. Nitrogen-containing carbon materials induce interactive forces between CO2 and nitrogen groups present in the material. CO2 is a weak Lewis acidic molecule because the carbon atom in CO2 is electrondeficient. Nitrogen-doped carbon atoms are negatively charged and nitrogen sites act as electron donors and behave like a Lewis base; therefore, nitrogen-containing carbon materials have acid-base interactions through which CO2 molecules are chemisorbed. The strong dipolar C=O bond generates an electric quadrupole moment in the CO₂ molecule, whereas nitrogen doping induces local polarization in the porous carbon matrix.52 Notably, N2 has a lower electric dipole moment than CO2. Hence, the interaction between the CO2 molecular quadrupole moment and high electrostatic potential of N-doped carbons enhances the CO2 adsorption energy, leading to selective and higher CO2 adsorption from flue gases. Experimental and computational studies have shown that surface hydroxyl



Scheme 2 Porous carbon materials for CO₂ adsorption.

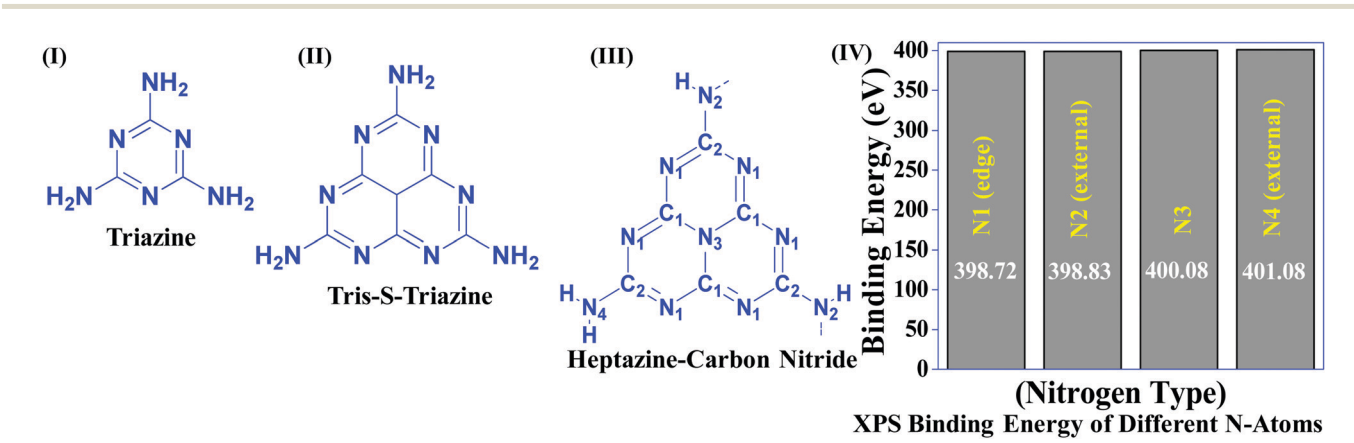
Table 1 Nitrogen-containing carbon materials and their CO2 uptake capacity⁴⁴

E. no.	Material	$S_{ m BET} \over ({ m m}^2{ m g}^{-1})$	Nitrogen content (%)	CO ₂ uptake mmol ⁻¹ g ⁻¹ (298 K)
1	NMC-600	272	6.33	3.90
2	NMC-700	518	6.06	3.60
3	AC-600-0.5	508	6.70	3.00
4	AC-600-2	966	4.50	3.64
5	AC-800-2	2448	3.90	3.00
6	Sk-0.5-700	1060	0.48	4.24
7	SK-4-700	2792	0.18	3.05
8	PGC-K	1143	8.30	4.00
9	FCP-1-KC	800	0.60	5.20

groups present in the N-doped carbon skeleton enhance the interaction between -OH and -NH functionalities leading to high CO₂ adsorption in N-doped carbon materials.⁵³ Nitrogen doping and surface functionalized amines have different types of interaction. Surface functionalized amines interact with electropositive carbon of CO₂ and form ammonium carbamate leading to high CO₂ adsorption on the surface. ⁵⁴ However, surface and pore blockage and thermal instability of functionalized amines are some of the demerits of surface amine-functionalized carbon materials; therefore, nitrogen-doped carbon is superior over amine-functionalized carbon materials. Based on the varied textural properties and chemical properties (due to N doping and amine functionalization), it can be concluded that high surface area and high nitrogen contents both are important factors contributing to high CO₂ adsorption (Table 1).⁴⁴ Moreover, when CO₂ activation and utilization for chemical synthesis are considered both these factors play important roles.

Table 1 suggests that a large number of framework substituted N atoms in a carbon matrix is required for high CO2 adsorption. The graphitic carbon framework provides high thermal stability and conductivity, which would be good for photocatalysis and electrocatalysis. An ideal porous carbon material and its properties are listed in Scheme 2. Based on these characteristic features, a unique carbonaceous material known as graphitic carbon nitride (g-C₃N₄) can best serve this purpose. When a simple nitrogen-rich organic compound (such as urea, melamine, cyanamide, dicyandiamide, etc.) is thermally-

polymerized in the temperature range of 500-700 °C, it produces carbon nitride. This material was synthesized way back in 1834 by Berzelius;⁵⁵ however its potential as a catalyst⁵⁶ and photocatalyst⁵⁷ was realized in 2006 and 2009, respectively. This crystalline material exists in seven allotropes: α-C₃N₄, β -C₃N₄, cubic C₃N₄, pseudocubic C₃N₄, g-h-triazine, g-o-triazine, and g-h-heptazine with bandgaps of 5.49, 4.85, 4.30, 4.13, 2.97, 0.93, and 2.88 eV, respectively.⁵⁸ These allotropes vary in their nitrogen environment and nitrogen contents. Theoretically, carbon nitride is predicted to have a C/N ratio of 0.75 without any surface functional groups and hydrogen content but the reality is far from this prediction. Carbon nitrides have been actually obtained with varied C/N ratios using different nitrogen-containing organic compounds at varied reaction temperature. It is possible to synthesize carbon nitrides such as C_3N , C_3N_2 , $C_{10}N_3$, C_5N , C_3N_5 , C_3N_6 , C_3N_7 , etc., having different nitrogen contents than the theoretically predicted ideal C_3N_4 and those are termed as nitrogen-rich (C/N < 0.75) and nitrogen lean (C/N > 0.75) C₃N₄.⁵⁹ Whenever a six-membered conducting atomic-scaffold is envisaged, structures such as those of benzene or borazine pop-up in our minds. Based on this perception, the triazine-like structure of C₃N₄ can be predicted (Scheme 3(I)). But it has been found that triazine or tri-s-triazine units (Scheme 3(II)) (also known as tectonic units) propagate in three dimensions to produce allotropes of g-C₃N₄ (Scheme 3). Computational studies based on Density Functional Theory (DFT) suggest that the tri-s-triazine unit is more stable than the triazine unit by 30 J mol⁻¹.60 Later, 2,5,8-triamine, tri-striazine (C₆N₁₀H₆) has been isolated, which confirms the building units of g-C₃N₄.61 Theoretical g-C₃N₄ should have an ideal C/N ratio of 0.75 and should not possess any H or O atoms; however, XPS and elemental analysis suggest that it has H and O atoms in small quantities in addition to C and N. Notably, H and O atoms are observed due to terminal amine groups and surface adsorbed water and (C=O), (O-N), and (C-OH) groups, for which the details are provided in Scheme 3. Various types of C and N are designated in one pictorial representation of a terminal tri-s-triazine unit of g-C₃N₄ (Scheme 3). The structure clearly shows that it has two different types of C represented as C1 and C2 (Scheme 3(III)). Similarly, four different types of

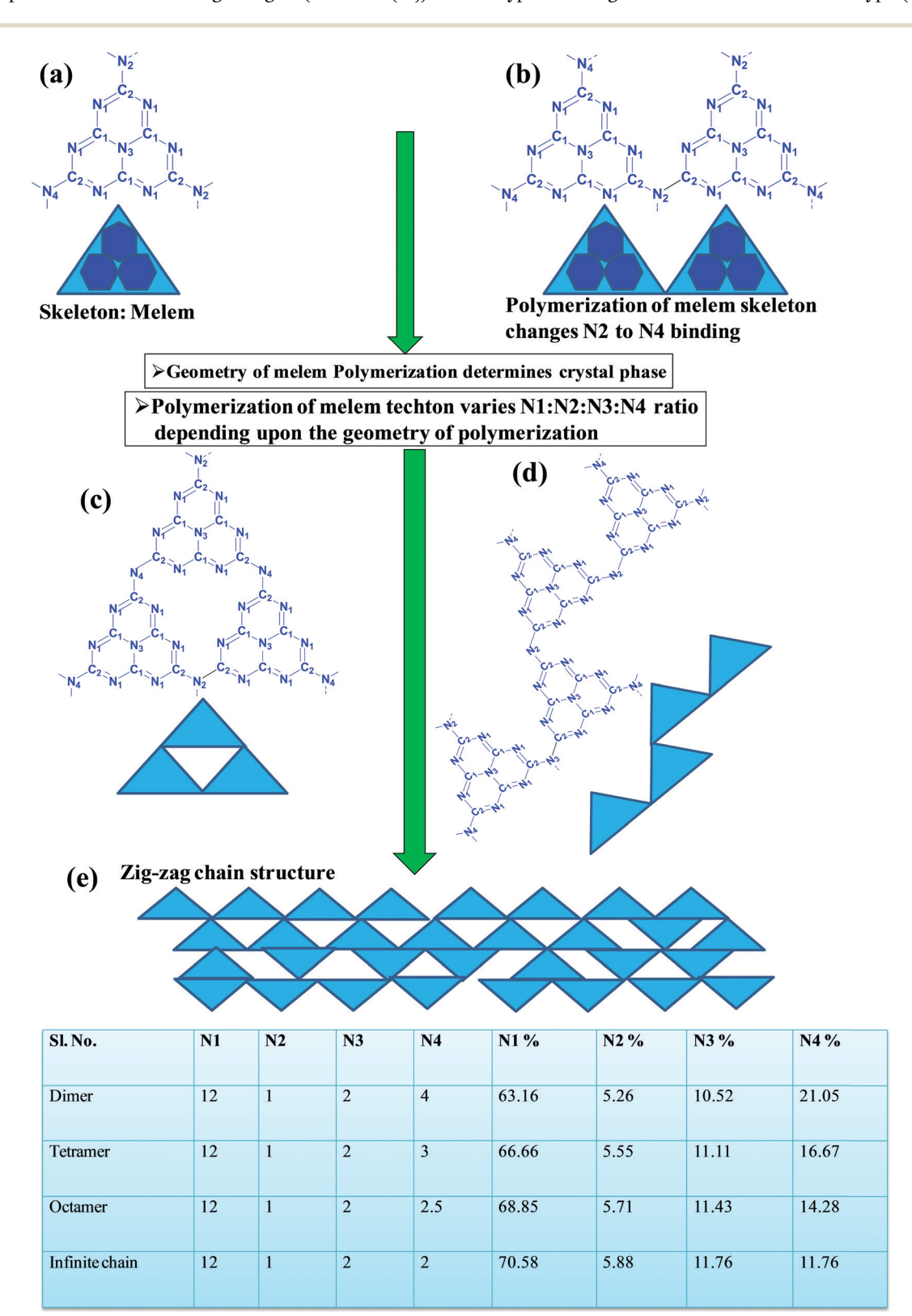


Scheme 3 Chemical structure of (I) triazine, (II) tris-s-triazine, and (III) heptazine units of carbon nitride, and (IV) various N types and their binding energies.

Materials Advances Review

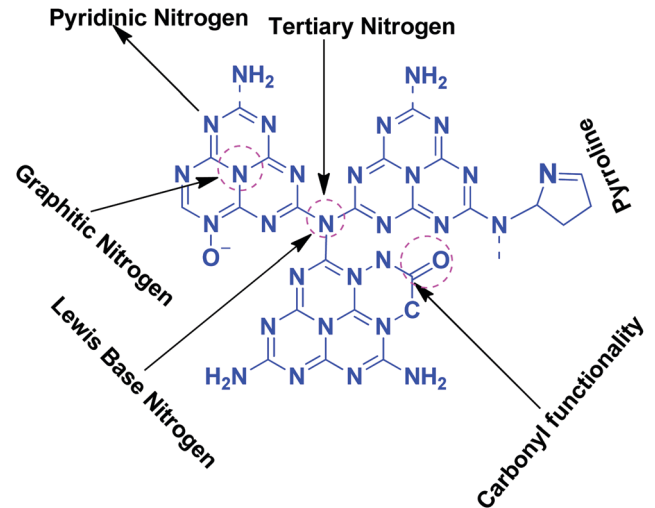
nitrogen atoms are designated as N1 (pyridinic), N2, N3 (graphitic-N), and N4 (Scheme 3(III)). They can be easily distinguished from XPS analysis due to different electronic environments that provide different binding energies (Scheme 3(IV)).62

In a true heptazine building unit (also known as melem), N2 is absent and N1: N3: N4 should be present in the ratio 6:1:3 (Scheme 4a). When the melem monomer polymerizes, the N4-type of nitrogens are converted to the N2-type (Scheme 4b).



Scheme 4 Evolution of different geometry and N types present in C_3N_4 based on the variation of the linkages of melem units.⁵³

Review **Materials Advances**



Different types of N and O functionalities present in $g-C_3N_4$

The N4/N2 ratio in the melem framework depends on the propagating direction to form g-C₃N₄ (Scheme 4c). Moreover, the stability of g-C₃N₄ also varies depending on the geometry of the final g-C₃N₄ polymer. When melem units are linked and form dimers, tetramers, octamers, and infinite chains, then the % N1 contribution increases. Moreover, the percentage of different N-types varies based on the geometry of their linkages as shown in Scheme 4 (inset table).⁶² The stability of g-C₃N₄ after catalysis can be estimated by the % of different types of N so that the breakage of linkages, chain fragmentation, and different structural changes can be predicted. CO2 adsorption and its activation highly depend on the type of N-moieties present (pyridinic, pyrrolic/ pyridonic, and graphitic nitrogen). Pyridinic and pyrrolic/pyridonic nitrogen groups have lone pair electrons that exhibit Lewis basicity and, thereby, have the capability towards CO2 adsorption and activation. Pyridinic nitrogen exhibits a higher affinity for CO2 molecules than pyrrolic nitrogen owing to the higher basic strength of the former than the latter (Scheme 5).63,64

Pyridinic-N with a higher negative charge in the 2-D plane retains a lone pair of electrons that can bind CO2 more efficiently than other types of N moieties. 65,66 Quaternary graphitic nitrogen exhibits Lewis acidity. 67,68 Electrons are mostly present in the π^* -antibonding orbital in graphitic-N and thus are less accessible to CO₂ for binding.⁶⁵⁻⁶⁷ Pyridinic-N and graphitic-N can be easily presented in the melem units; however, other types of N-species are formed during un-controlled thermal polymerization in an oxygen lean environment leading to partial terminal uncondensed amines, N-oxide, and pyrrolic N species as shown in Scheme 5. The various N-species discussed above have the ability to impart tunable basicity, H-bonding, and Lewis acidity (frustrated Lewis acid-base pairs) and are thus suitable for various types of catalytic reactions involving CO2 as a reactant.

3. Synthesis strategies adopted for the preparation of carbon nitrides for improved CO₂ conversion

Based on the discussion so far we have understood that suitable micropores, high surface area, and pyridinic rich N sites are required for high CO₂ adsorption. CO₂ adsorption alone is not sufficient to catalyze various types of CO2 based reactions because reactive partners also need to be efficiently adsorbed and suitably activated to synthesize various CO2 derived chemicals. Further, bandgap and band edge positions can be finely tuned depending on the doping and crystallinity for lightinduced CO₂ conversion. Thus, synthetic strategies, types of precursors, the temperature for synthesis along with the environment, and other parameters influence the physicochemical properties of g-C₃N₄. The following section describes the various synthesis strategies reported for the preparation of g-C₃N₄ for improved CO2 activation.

3.1 Template free synthesis for improved catalysis and photocatalysis

Nitrogen-rich organic compounds such as melamine, cyanamide, and dicyandiamide are heated in semi-closed systems in oxygen-lean conditions to form g-C₃N₄ (Scheme 6). g-C₃N₄ is formed by various condensation steps in which the first melamine is formed at lower temperatures (<350 °C) followed by removal of NH₃ leading to tris-s-triazine at a temperature around 400 °C. The polymerization of tris-s-triazine takes place at around 520 °C to form g-C₃N₄ (Scheme 6).⁶⁹ TGA investigation reveals that this framework is stable up to 550 °C. Even oxygen-containing precursors such as urea also follow the same sequence and form g-C₃N₄ via a melamine intermediate (Scheme 6). The nitrogen content and surface area of g-C₃N₄ depend upon the precursor and the pyrolysis temperature. With the increase in the pyrolysis temperature, the C/N ratio increases whereas the bandgap decreases.⁷⁰ During the polymerization process, the amine groups of tris-s-triazine don't condense completely, which results in the formation of uncondensed amine group-containing g-C₃N₄ with about 2% H content with a C/N ratio less than 0.75. Such a structural defect is important for the adsorption of reactant molecules, which is good for catalytic reactions.71 It may be noted that if the uncondensed groups (discussed above) are present in higher numbers then it might be good for conventional catalysis but is definitely not suitable for photocatalysis due to the less efficient charge transportation and separation of charge carriers. Hightemperature polymerization leads to the formation of crystalline g-C₃N₄, which is better for charge carrier separation and a higher degree of π -conjugation and thus good for photocatalysis.⁷² Moreover, with the increase in the pyrolysis temperature, aggregated bulk g-C₃N₄ changes to a nanosheet and nanoflake like morphology with improved surface area. 73,74 Also, urea and thiourea derived g-C₃N₄ exhibit better surface area due to the removal of CO₂ at higher temperatures, leading to high porosity and improved surface area when compared to the cyanamide precursor.

Propargyl amine
$$O=C=NH$$
 H_2N NH_2 H_2N H_2

Scheme 6 Synthesis of g-C₃N₄ via the melem unit using different precursors.

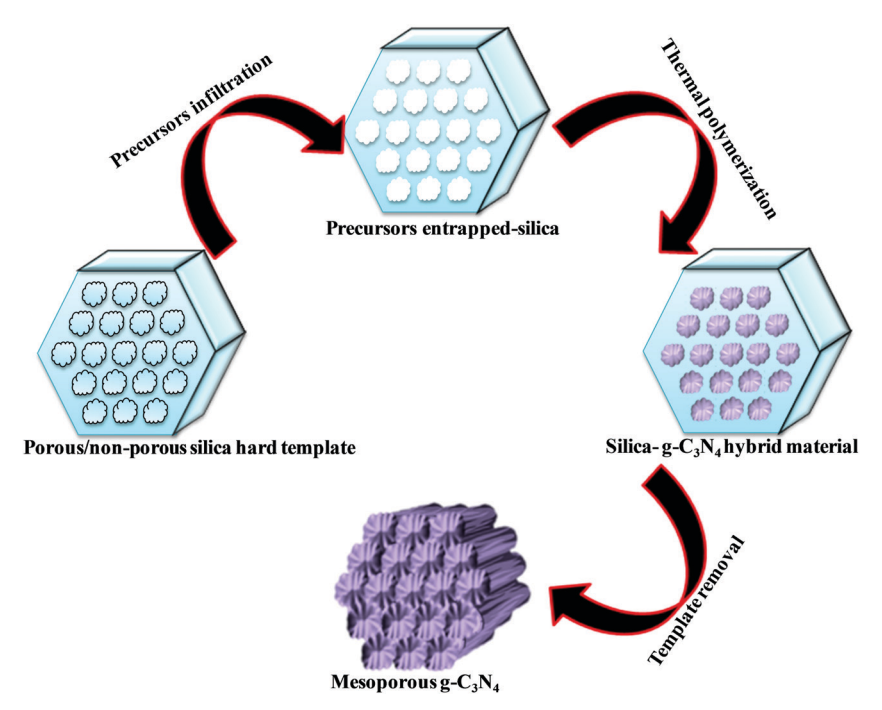
Guanidinium thiocyanate

Further, the surface area of urea derived g-C₃N₄ is improved if the pyrolysis is carried out for a longer time.⁷⁴ During such prolonged heating the layered structure of g-C₃N₄ is exfoliated and splitting takes place to produce low yield g-C₃N₄ with better surface area and photocatalytic activity.75 Inspired by the synthetic paradigm of g-C₃N₄ from urea which has resulted in higher surface area due to the liberation of CO2 during urea pyrolysis, sucrose and melamine have been pyrolyzed together. The reason for selecting sucrose is that it will generate a large amount of CO2 during pyrolysis and produce g-C3N4 with N-deficiency and improved surface area (6 fold higher) and porosity.⁷⁶ The type of N species and surface area can be tailored by selecting different precursors. For example, guanidine hydrochloride or guanidine thiocyanate pyrolysis results in g-C₃N₄ via a melem intermediate and produced materials with high surface area and enhanced photocatalytic activity (Scheme 6).⁷⁷ The bandgap of g-C₃N₄ can be reduced and midgap creation is possible if a nitrogen-vacancy is created in the material. Nitrogen deficiency in g-C₃N₄ leaves additional electrons and creates nitrogen-vacancy related C3+ states leading to a reduced bandgap material. This can be easily achieved by heating the material in an H₂ atmosphere. H₂, being a small molecule, can easily penetrate and diffuse to the interior lattice sites and reduce the lattice N sites and liberate NH₃ and create an N vacancy. In this process, the terminal N sites are more prone to reduction due to the lowest change in the energy of the molecule. Such an N vacancy in the system reduces the bandgap by downshifting of the CB and up-shifting of the VB position. Another situation can also arise in which new C and N sites are generated, which increases the H contents in the material and alters the bandgap of the material. Experimental analysis suggests that a three coordinated N-vacancy and H-substitution at the N sites decrease the bandgap by 0.2 and 0.55 eV.⁷⁸ This lowering in the bandgap is due to the formation

of additional band states below the CB by the defect C sites leading to lowering the bandgap values. The N-vacancy moves the VB energy to more negative values and H-substitution lowers the CB to more positive values and improves the visible light absorption capacity. The surface area of g-C₃N₄ can be improved by exfoliating bulk g-C3N4 in different solvent media such as water, ethanol, acetone, IPA, and NMP. Among these solvents, NMP has been found to be the best choice. 79 However, it is difficult to remove NMP from the exfoliated g-C₃N₄. Thus IPA has been explored as the next most desirable solvent to exfoliate bulk g-C₃N₄, so as to produce high surface area g-C₃N₄ of the order of 300-400 m² g⁻¹. For exfoliation of bulk g- C_3N_4 , aqueous alkaline and acidic solutions have also been explored with the aim of obtaining higher surface area. 80,81 Although an improvement in the surface area is observed by varying the precursors, reaction temperatures, and pyrolysis environment, however, the materials still remain nonporous in nature. In order to introduce porosity in the material, template-assisted synthetic strategies have also been adopted as discussed below.

3.2 Template-mediated synthesis strategy to produce $g\text{-}C_3N_4$ with high surface area and porosity for improved CO_2 adsorption

Various hard template-mediated synthetic strategies utilize silica-based mesoporous materials (SBA-15, SBA-16, KIT-6, MCM-41, and MCM-48) as the template (Scheme 7). Nitrogencontaining organic precursors or carbon and nitrogen precursors are infiltrated into the porous architecture of silica materials *via* the incipient wet impregnation or wet impregnation method followed by pyrolysis, which results in the formation of g-C₃N₄/silica hybrid materials. Finally, the silica template is removed by chemical etching using various etching agents, for example, NaOH, HF, and NH₄HF₂. The final material has the same architecture as that of the original silica material. ⁸²



Scheme 7 Hard template mediated synthesis of mesoporous q-C₂N₄

Even silica nanoparticles have produced porous g-C₃N₄ with an average pore diameter of 12 nm, which is equivalent to the original silica nanoparticles.83 In general, the pore diameter of the resulting material is smaller than the porous silica materials due to volume shrinkage of g-C₃N₄ filled inside the pores during the condensation.84 The surface area and porosity significantly depend on the Si/precursor, hard template, and etching agent. The surface area can be further improved if the original silica material is treated with acid to enhance the surface reactivity, which allows a large number of organic precursors to in-filter, which improves the surface area of the resultant material.85 This synthetic strategy produces a low yield of g-C₃N₄ and, therefore, is difficult for application in the large scale synthesis of mesoporous g-C₃N₄. Further, hazardous and costly HF and NH₄HF₂ limit its industrial-scale production.⁸⁶ To overcome this problem, CaCO₃ has been used as a hard template in which the template is removed with dilute HCl after polymerization, leading to the formation of high surface area g-C₃N₄ with improved photocatalytic activity.⁸⁷

Large scale synthesis of mesoporous g-C₃N₄ can be achieved using the soft template method. Since the soft template is a carbon-based compound, therefore g-C₃N₄ with higher C/N is formed with diverse functionality. Ionic liquids and block copolymer-based soft templates have been widely used to prepare mesoporous g-C₃N₄. Among the soft templates, only a few templates such as Triton-100 and ionic liquids have produced g-C₃N₄ with large surface area and porosity.⁸⁷⁻⁸⁹ Ionic liquids act as soft modifiers for the thermal polymerization, leading to tunable textural properties, morphology, and reactivity. Anions of the ionic liquids participate in the growth process via C-N condensation. 90 Dual templating methods and cooperative assembly of two surfactants lead to formation of a

mesophase, which results in the formation of nanostructured materials. A similar strategy can be applied to synthesize mesoporous g-C₃N₄. Cooperative supramolecular assembly of surfactants, or a reactant and a surfactant, or reactants induced by hydrogen bonding and other weak electrostatic forces can act as a template to form mesoporous g-C₃N₄. Nitrogenrich organic precursors can easily form hydrogen bonding with "O" containing organic compounds to form self-assembled porous g-C₃N₄. For example, melamine can form hydrogen bonding with cyanuric acid in DMSO and form stable aggregates that easily precipitate out (Scheme 8). Such precipitates can be thermally polymerized to form mesoporous g-C₃N₄.91 In fact, supramolecular aggregates can be formed by the hydrogen bonding between three reactants such as melamine, cyanuric acid with urea/barbituric acid/caffeine, etc. in a different solvent medium, which results in different morphology of mesoporous g-C₃N₄ on thermal polymerization with different textural properties and photophysical characteristics (Scheme 8). 92-94 Template mediated synthesis strategies can provide materials with high surface area and porosity but it is difficult to tune the N contents and type of nitrogen due to the specific use of a suitable template and nitrogen precursor. Thus more work is needed to develop soft-template mediated synthesis recipes with variable N contents and functional amine sites using a diverse range of C and N containing precursors for the appointed applications.

3.3 Strategies to functionalize and dope elements to improve catalytic activities and light absorption properties

Template-mediated synthetic strategies can improve the surface area and porosity. However, for tuning the catalytic activities relating to the efficient adsorption of reactants and

Scheme 8 Supramolecular assembly of precursors leading to formation of mesoporous g-C₃N₄.

light absorption, suitable doping and functionalization are required. By varying the nitrogen precursors, the C/N ratio can be tailored, but for doping other elements such as O and S, suitable precursors containing O and S should be used during the synthesis of g-C₃N₄. Just by H₂O₂ treatment, O doped g-C₃N₄ with high surface area is obtained, which exhibits efficient charge carrier separation, and a red-shift in the absorption spectra. ⁹⁵ An oxygen group containing melamine precursor also produces O doped g-C₃N₄. ⁹⁶ Organic surfactant mediated synthesis produces C doped g-C₃N₄. ⁹⁷ Diammonium hydrogen phosphate, hexachloro-cyclotriphosphazene, 2-aminoethylphosphonic acid, *etc.* have been used as a P source to dope P into the g-C₃N₄ framework. ⁹⁸⁻¹⁰⁰ H₂S treatment, thiourea, and

tri-thiocyanic acid precursors are known to dope S in the g- C_3N_4 framework. $^{101-103}$ B-Doped g- C_3N_4 has been prepared by heating melamine and B₂O₃ above 520 °C to introduce B into the g- C_3N_4 framework. 104 BH₃NH₃ and sodium-tetraphenyl boron have been used as precursors to prepare B-doped g- C_3N_4 . 105,106 Recently, it has been reported that exfoliation of g- C_3N_4 (prepared by urea and thiourea) with concentrated H₂SO₄ aqueous solution at 80 °C has produced –SO₃H functionalized g- C_3N_4 . 107 Furthermore, it has been found that a small quantity of 2-methyl imidazole can be treated with urea-thiourea to produce O and C co-doped g- C_3N_4 . 108 Thus, the choice of precursor and the treatment conditions can introduce desired elements and functionality in g- C_3N_4 to impart the desired catalytic activity.

4. Synthesis of chemicals and fuels from CO_2 using $g-C_3N_4$ as a catalyst in the conventional thermal catalytic process

Several recent review articles have been published, even using carbon nitrides as catalysts and photocatalysts. $^{109-111}$ In this section, the role of CO_2 as a C_1 source to produce chemicals and fuels is described (Scheme 9). CO_2 can also act as an "O" source and can be utilized as an oxidant. CO_2 can be efficiently reduced to provide various chemicals and fuels. All these processes are non-atom efficient processes. CO_2 can be inserted in organic compounds like epoxides, amines, and alkynyl acids to produce organic carbonate and carbamate in a highly atom efficient process.

4.1 Role of CO₂ as a soft oxidant or promoter in the oxidation reaction

The oxidizing ability of various gases in coke oxidation follows the order: $O_2(105) > H_2O(3) > CO_2(1)$, and thus CO_2 can act as a soft oxidant. 112 Such a weak oxidation ability is suitable in the oxidative dehydrogenation reaction. Oxidative dehydrogenation in the presence of oxygen leads to the generation of a large amount of CO₂ as a by-product due to the strong oxidizing ability of O2. 113 CO2 is a weaker oxidant and, therefore, it requires activation energy. In general, this activation can be achieved with alkali metals such as Li, K, Na, Ba, Ca, and Cs, which activate CO₂ to form MCO₂. 114 The activity of Li is higher among the above-mentioned metals due to the CO2-M valence bond angle, which is favorable for efficient CO2 activation and utilization. In this dehydrogenation reaction, CO2 facilitates the abstraction of hydrogen from hydrocarbons (alkanes, alkenes, alcohols, and alkyl aromatics) via catalytic activation to form CO and O species and suppress the total oxidation. 115

Scheme 9 Synthesis of organic compounds using CO_2 as a reactant or oxidant or promoter and C_3N_4 as a catalyst.

g-C₃N₄ has been reported for the oxidation of benzene to phenol using CO₂ as a mild oxidant.¹¹⁶ CO₂ is activated *via* the secondary amine and pyridinic N of g-C₃N₄. Benzene is adsorbed weakly on g-C₃N₄. CO₂ splits into an Ö diradical, followed by its reaction with weakly adsorbing benzene to form the desired phenol as a product (Scheme 10). CO is eliminated after the reaction to regenerate the active sites for further CO₂ adsorption.¹¹⁶ CO₂ acts as a promoter in the cycloalkene oxidation using O₂ as an oxidant over a g-C₃N₄ catalyst (eqn (3), Scheme 9).¹¹⁷ CO₂ is efficiently adsorbed on g-C₃N₄ to form surface O species and produce CO (confirmed from the FT-IR study). Such surface O assists in the oxidation of cyclic olefins.¹¹⁶

4.2 Carboxylation of terminal alkynes with CO₂

Alkynylcarboxylic acid is an important synthetic intermediate for several important compounds. For this reaction to proceed, both the alkyne and CO2 need to be activated (Scheme 9, eqn (4)). CO₂ can be activated with g-C₃N₄ but for the efficient adsorption and activation of an alkyne, highly disperse active metals such as Cu or Ag are required. Ag NP decorated g-C₃N₄ has been reported for this reaction. 118 This reaction follows the Langmuir-Hinshelwood mechanism in which CO2 is absorbed and activated by g-C₃N₄ and the alkyne is adsorbed and activated by Ag NPs supported on g-C₃N₄. Alkyne acidic hydrogen is activated by the Ag NPs and forms silver acetylide and then this reactive intermediate reacts with activated CO2 to produce silver carboxylate, which can be easily converted into cesium carboxylate with the help of Cs₂CO₃ via a transmetalation step. Finally, by workup with an acidified solution, it forms the desired alkynyl carboxylic acid.

4.3 Insertion of CO₂ into epoxides to form cyclic carbonates

The synthesis of cyclic carbonates by the reaction of CO₂ and epoxides is one of the most widely investigated reactions for CO₂ utilization because it is a 100% atom economic process. The cyclic carbonate product can be used as an intermediate for the production of value-added compounds such as Bisphenol-A carbonate (a synthetic polymer used in the packaging industry) and dimethyl carbonate (a methylating agent and a green solvent), the latter being a good fuel additive and a precursor for various other industrially important chemical transformations. CO₂ can be inserted in the epoxide ring via a nonconcerted process to produce the cyclic carbonate. For this reaction, generally, a catalyst should contain a Lewis basic site, which acts as a nucleophile to activate the 'C=O' bond of the CO2 molecule, while a Lewis acidic site acts as an electrophile for activating the epoxide ring. 119 The Lewis acidic site polarizes the epoxide ring and forms an epoxide anion and then it acts as a nucleophile and attacks the CO₂ molecule, leading to the formation of a carbonate anion intermediate. The next step is either a ring-closing process for the formation of the cyclic carbonate or insertion of one or more epoxides and CO2 molecules into the intermediate, which produces a polycarbonate. 119 g-C3N4 has surface/edge located free -NH2 groups which serve as Lewis basic sites and act as the

Scheme 10 Oxidation of benzene to phenol using CO_2 as an oxidant and $g-C_3N_4$ as a catalyst.

nucleophile to activate CO₂. However, a Lewis acid site is absent to activate the epoxide. The weak activity of g-C₃N₄ towards this reaction is due to surface -OH sites which have the ability to weakly activate the epoxide and produce a very low yield of the product. For this reaction to proceed efficiently, a co-catalyst such as tetra butyl ammonium bromide (TBAB) is used. However, suitable metal-free bi-functional g-C₃N₄ is reported to effectively catalyze this reaction. 107 Production of cyclic carbonates using different g-C₃N₄ based catalysts is summarized in Table 2. Conventional g-C₃N₄ exhibits very low activity (Table 2, entry 1). 120 Mesoporous g-C₃N₄ (prepared with different precursors) has exhibited better activity than conventional g-C₃N₄. Among the prepared materials, mesoporous g-C₃N₄ prepared with melamine exhibits 34% propylene oxide conversion, and 90% propylene carbonate selectivity with a TOF of 3.4 h⁻¹ at moderate reaction conditions in DMF (Table 2, entries 2-4). 121 A mixture of gas (50% O2 and 50% CO2) is used during this reaction and it has been proposed that O₂ plays a promotional role for the activation of the epoxide by supplying additional oxygen during the course of the reaction. 120 Further, to improve the surface area and dispersed active sites, SBA-15 supported g-C₃N₄ is employed for propylene carbonate synthesis under solvent-free conditions in the presence of doped metal ions, which act as Lewis acid sites. Among metal salts, Zn²⁺ exhibits the highest conversion and selectivity of 98.3% and >99%, respectively (Table 2, entries 5-8). 122 The activity of doped Zn2+ is better than the supported ZnCl₂ catalyst (Table 2, entry 9). 123 It is proposed that the C₃N₄ nanosphere inside the mesopore

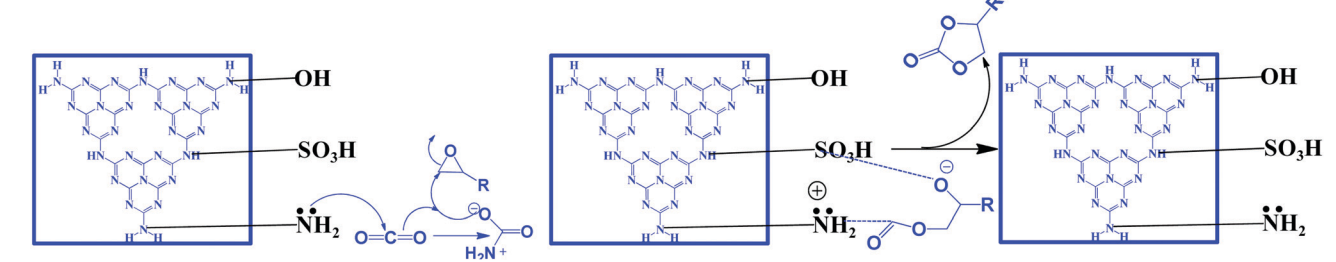
channel of silica supplies the activated CO2 to the epoxide through a transfer mechanism and facilitates cyclic carbonate synthesis via Zn²⁺ activated epoxide species. Porous and amino rich g-C₃N₄ is prepared without using any hard template using urea as a precursor to form defective and edge enriched C₃N₄. The urea derived C₃N₄ produces a wide variety of cyclic carbonates in the absence of any co-catalyst under solvent-free conditions (Table 2, entries 10-13). 124 It is suggested that the edge defects contain both primary amines (-NH2) and secondary amine groups (-C-NH-C) and therefore they are able to activate CO₂. The epoxide is activated by the defective C₃N₄ edge containing -OH groups. Further, it has been revealed that urea derived C₃N₄ exhibits relatively higher surface area (41 m² g⁻¹) than dicyandiamide derived C_3N_4 and a porous nature, and the existence of macropores facilitates mass transfer and enhances the catalytic activity. n-Bromobutane grafted mesoporous g-C₃N₄ exhibits better catalytic activity for solvent-free propylene carbonate synthesis with 88% conversion and 98% selectivity (Table 2, entry 14).125 In this process, the *in situ* depleted Br⁻ acts as the electrophile which activates the epoxide ring, while the defect rich edge positioned -NH2 polarizes the CO₂ molecule leading to the bi-functional nature. Butane in conjugation with halides have been evaluated and it has been found that bromide exhibits the best activity because of its better leaving group ability. The better catalytic activity is attributed to the mesoporous nature (15 nm), high surface area (241 m² g⁻¹), and coexistence of terminal -NH₂ groups in g-C₃N₄ and X⁻ groups, which is even far better than the

Benzene coordinated CO2 adsorbed C3N4 framework

Table 2 Comparative catalytic activity of various g- C_3N_4 based catalysts in the synthesis of cyclic carbonates

E. no.	Catalyst	$S_{\text{BET}} (\text{m}^2 \text{g}^{-1})$	Co-catalyst	Reaction conditions	Conv. (%)	Select. (%)	TOF (h^{-1})	Ref
1.	g-C ₃ N ₄ (prepared with melamine)	64	_	ECH (5 mL), catalyst (50 mg), temp. (150 °C), press. (3.5 MPa),	5.6	96.7	3.3	120
2.	Mesoporous- C_3N_4 (prepared with melamine-2D mesoporous silica)	_	_	time (2 h) PO (1.5 mL), catalyst (20 mg), DMF (10), temp. (100 °C), press.	34.0	90	_	121
3.	Mesoporous-C ₃ N ₄ (prepared with urea-formaldehyde-2D	_	_	(0.55 MPa), time (10 h) PO (1.5 mL), catalyst (20 mg), DMF (10), temp. (100 °C), press.	28.0	92	_	121
4.	mesoporous silica) MS-C ₃ N ₄ (prepared with melamine-glyoxal-2D mesoporous silica)	_	_	(0.55 MPa), time (10 h) PO (1.5 mL), catalyst (20 mg), DMF (10), temp. (100 °C), press. (0.55 MPa), time (10 h)	25.0	98	_	121
5.	Mesoporous-C ₃ N ₄ (prepared with dicyandiamide-SBA-15)	586	_	SO (3 mL), catalyst (100 mg), temp. (150 °C), press. (3.5 MPa), time (1.5 h)	28.8	99	4.8	122
6.	Mesoporous- C_3N_4 (prepared with dicyandiamide-SBA-15)	585	Zn ²⁺ (0.8 wt%)	SO (3 mL), catalyst (100 mg), temp. (150 °C), press. (3.5 MPa), time (1.5 h)	94.5	99	15.8	122
7.	Mesoporous- C_3N_4 (prepared with dicyandiamide-SBA-15)	585	Zn ²⁺ (0.8 wt%)	PO (3 mL), catalyst (100 mg), temp. (150 °C), press. (3.5 MPa), time (1.5 h)	97.1	99	16.2	122
8.	Mesoporous- C_3N_4 (prepared with dicyandiamide-SBA-15)	585	Zn ²⁺ (0.8 wt%)		98.3	99	16.4	122
9.	$10\% ZnCl_2/mesoporous\ C_3N_4$	206	Zn^{2+}	EO (7 mL), DMF (3 mL), catalyst (200 mg), temp. (140 °C), press. (2.5 MPa), time (6 h)	73.0	99.4	5.6	123
10.	$g\text{-}C_3N_4$ (prepared with urea and heated at 480 $^{\circ}\text{C})$	40.8	_	(21.5 km d), catalyst ECH (21.5 mmol), catalyst (100 mg), temp. (130 °C), press. (3.5 MPa), time (4 h)	99.6	96.4		124
11.	g-C $_3N_4$ (prepared with urea and heated at 480 $^{\circ}\text{C})$	40.8	_	(3.5 Mra), time (4 m) EO (21.5 mmol), catalyst (100 mg), temp. (130 °C), press. (3.5 MPa), time (4 h)	91.7	99.3		124
12.	g-C $_3N_4$ (prepared with urea and heated at 480 $^{\circ}\text{C})$	40.8	_	time (4 h) SO (21.5 mmol), catalyst (100 mg), temp. (130 °C), press. (3.5 MPa), time (4 h)	98.0	99.8		124
13.	g-C $_3N_4$ (prepared with urea and heated at 480 $^{\circ}\text{C})$	40.8	_	PO (21.5 mmol), catalyst (100 mg), temp. (130 °C), press. (3.5 MPa),	99.3	99.6		124
14.	n -ButBr doped mesoporous C_3N_4 (prepared with cyanamide and 12 nn silica spheres)	248	Br ⁻	time (24 h) PO (10 mL), catalyst (200 mg), temp. (140 °C), press. (2.5 MPa), time (6 h)	88.0	99.7	9.6	125
15.	H ₂ SO ₄ treated g-C ₃ N ₄ (prepared with melamine)	32	_	ECH (5 mL), catalyst (50 mg), temp. (130 °C), press. (3.5 MPa),	99.1	99.5	58.1	120
16.	H ₂ SO ₄ treated g-C ₃ N ₄ (prepared with urea-thiourea)	10	_	time (2 h) ECH (63 mmol), catalyst (50 mg), Temp. (100 °C), press. (1.0 MPa), time (4 h)	93.5	99		107
17.	P-Doped g- C_3N_4 (prepared with melamine-hexachlorotriphosphazene)	_	$\mathrm{Bu_4NBr}$	Hille (4 II) PO (28.6 mmol), catalyst (150 mg), Bu ₄ NBr (2.4 mol%), temp. (100 °C), press. (2.0 MPa), time (4 h)	99.8	99.9		126
18.	B-Doped g- C_3N_4 (prepared with melamine-BmimBF ₄)	11.1	_	ECH (14.3 mmol), catalyst (50 mg), temp. (130 °C), press. (2.8 MPa), time (6 h)	89.0	98.0	5.8	127
19.	B-Doped g- C_3N_4 (prepared with melamine-BmimBF ₄)	11.1	_	(2.8 MPa), time (6 II) PO (14.3 mmol), catalyst (50 mg), temp. (130 °C), press. (2.8 MPa), time (6 h)	31.0	99.9	1.5	127
20.	B-Doped mesoporous g-C ₃ N ₄ (prepared with dicyandiamide– B(OH) ₃ -SBA-15)	123	_	SO (1 mL), catalyst (30 mg), temp. (130 °C), press. (3.0 MPa), time (24 h)	97.8	96.8	_	129
21.	g-C ₃ N ₄ (prepared with melamine)	_	$\mathrm{Bu_4NBr}$	Light assisted method, ECH/SO (13.7 mmol), catalyst (50 mg), Bu ₄ NBr (1.8 mol%) temp. (105 °C), press. (1 atm, balloon), time (20 h)	100	100		130

ECH = epichlorohydrin, PO = propylene oxide, SO = styrene oxide, TOF = turnover frequency, conv. = epoxide conversion, selec. = cyclic carbonate selectivity, S_{BET} = surface area.



Scheme 11 Synthesis of cyclic carbonates using bi-functional $g-C_3N_4$, reproduced with permission, Copyright Royal Society of Chemistry, ref. 107.

externally induced *n*-bromobutane to carbon nitride during the course of the reaction (Table 1, entry 14). 125 Huang et al. have reported H₂SO₄ treated, protonated acidic functionality containing carbon nitride, which has been investigated for the solvent-free cycloaddition of CO2 with epichlorohydrin for the synthesis of the corresponding carbonate (Table 2, entry 15). 126 This protonation process has altered the electronic and textural properties and surface chemistry, which results in the incorporation of hydroxyl groups and amine groups into the bulk urea derived carbon nitride, which provides 17 fold higher catalytic activity. Surface hydroxyl groups (-OH) and amine groups (-NH2) are responsible for this improved reactivity. Inspired by this work, Samanta et al. have synthesized urea and thiourea derived carbon nitride CN-(UTU), which exhibits moderate catalytic activity better than the counterparts urea/thiourea under solvent-free cyclic carbonate synthesis from epichlorohydrin without any co-catalyst (Table 2, entry 16) (Scheme 11). 107 Further, to improve the catalytic activity, the resultant materials have been chemically exfoliated with H2SO4, which results in the simultaneous incorporation of -SO₃H and -NH₂ groups into the melem framework (Scheme 11).

The bi-functional catalyst (which is ideal for the CO₂ activation reaction) has been investigated in the CO₂ insertion reaction by varying the epoxide under very mild conditions (100 °C and 1 MPa). Excellent conversion and selectivity are achieved over this bi-functional CN-(UTU) catalyst. The simultaneous introduction of -NH2 groups (that act as basic sites for activating CO₂) and -SO₃H groups (that polarize the epoxide ring) has been confirmed from CO₂/NH₃-TPD. The synergistic participation of -NH2 and -SO3H groups during the reaction is the main reason for obtaining the excellent product yield. Moreover, doping with non-metals (such as P and B) over g-C₃N₄ is also reported for the synthesis of cyclic carbonates, which is found to be very effective for this reaction. 126-129 The -B(OH) and -P(OH) groups are found to be responsible for the catalytic activity enhancement (Table 2, entries 19-20). All the reactions discussed above require CO₂ pressure higher than one atmosphere. Only one report is available in which a cyclic carbonate is synthesized at 1 atm pressure under solvent-free conditions but in the presence of external co-catalyst (1.8%) TBAB (Table 2, entry 22). 130 Therefore, more work should be carried out to synthesize efficient catalysts that can catalyze this reaction under solvent-free conditions at atmospheric pressure.

5. Photocatalytic CO₂ reduction reaction (CO₂ photoreduction)

Photocatalytic CO_2 reduction is a surface catalytic reaction which employs light-induced holes and electrons generated over the surface of the catalyst and protons from the reaction medium. In ideal conditions, CO_2 reduction follows some fundamental steps, like other light assisted reactions such as water splitting, N_2 reduction, and organic transformations. The basic operating steps involved in the photocatalytic CO_2 reduction reaction are summarized in two categories, namely optoelectronic and physicochemical steps, that are complementary to each other:

- (A) Optoelectronic steps (Scheme 12A):
- (1) Creation of charge carriers (e⁻-h⁺) on the semiconductor surface by illumination with light having energy greater than the bandgap: $E_{h\nu} \geq E_{g}$.
- (2) Light-induced charge carrier dissociation and migration on the catalytic surface.
- (3) Charge-carrier recombination followed by the dissipation of energy in the form of heat.
- (4) The transported electrons participate in CO_2 reduction whereas holes participate in the oxidation of H_2O to O_2 , and H^+ or any other reducing agents to their corresponding oxidized products.
 - (B) Physicochemical steps (Scheme 12B):
 - (1) Adsorption of CO₂ on the catalyst surface.
- (2) CO_2 activation by the inherent functional groups of the catalyst.
- (3) Intermediate species adsorption and desorption of the products from the catalytically active sites during the reduction reaction.

5.1 Factors and parameters governing the mechanism of ${\rm CO_2}$ photoreduction

Carbon dioxide is the most stable and inert oxidized product, while methane is a completely reduced form of carbon (Scheme 13a). The light-induced conversion of CO_2 to hydrocarbons and oxygenated hydrocarbons depends on various factors and parameters. These factors determine the fate of the reaction as well as the CO_2 conversion and product distribution. Various factors influencing CO_2 reduction, especially with graphitic carbon nitride as a photocatalyst, are discussed in this section.

5.1.1 Thermodynamic factors. CO₂ conversion is a thermodynamically uphill energy process that requires a tremendous

O=C= (2) C₂H₅OH/CH₃OH/CH₄/HCOOH E_{CB} (LUMO) \mathfrak{S} Energy (1) জ H+/O₂ H₂O (A)

Scheme 12 Basic mechanism of the photocatalytic process: (A) optoelectronic steps and (B) physicochemical steps involved in the CO₂ reduction reaction.

energy input because of its stable and inert nature. An energy of 750 kJ mol⁻¹ is required for the splitting of one 'C=O' bond in the CO2 molecule. CO2 has a low electron affinity and a high energy gap of 13.7 eV between its lowest unoccupied molecular orbital (LUMO) and highest occupied molecular orbital (HOMO). 137 CO $_2$ is a linear molecule and electronic accumulation in the empty LUMO (antibonding Π^* orbital) facilitates the transformation of a linear to a bent geometry over the catalyst surface, which in turn expedites the kinetic barrier and enables its smooth conversion to appropriate products. The band edge position of any photocatalyst decides this electron accumulation and, accordingly, the product distributions occur. Particularly, the valence band edge must be positioned at a more negative electrode potential than the standard reduction potential of CO₂ to any other products otherwise the process is not thermodynamically feasible (Scheme 13b). Based on the standard reduction potential, 138 the reduced products are given below, which must be considered to analyze the reaction products after the reaction to establish the plausible mechanism of the reaction (Scheme 13b).

$$CO_2 + e^- \rightarrow CO_2^{\bullet -} [E^0 = (-1.85 \text{ V}) \text{ vs. NHE}]$$
 (1)

$$CO_2 + 2H^+ + 2e^- \rightarrow HCOOH [E^0 = (-0.61 \text{ V}) \text{ vs. NHE}]$$
 (2)

$$CO_2 + 2H^+ + 2e^- \rightarrow CO + H_2O [E^0 = (-0.53 \text{ V}) \text{ vs. NHE}]$$
(3)

$$CO_2 + 4H^+ + 4e^- \rightarrow HCHO + H_2O [E^0 = (-0.48 \text{ V}) \text{ vs. NHE}]$$
(4)

$$CO_2 + 4H^+ + 4e^- \rightarrow HCHO + H_2O [E^0 = (-0.20 \text{ V}) \text{ vs. NHE}]$$
(5)

$$CO_2 + 6H^+ + 6e^- \rightarrow CH_3OH + H_2O [E^0 = (-0.38 \text{ V}) \text{ vs. NHE}]$$
(6)

$$CO_2 + 8H^+ + 8e^- \rightarrow CH_4 + 2H_2O [E^0 = (-0.24 \text{ V}) \text{ vs. NHE}]$$
(7)

(B)

$$2H^{+} + 2e^{-} \rightarrow H_{2} [E^{0} = (-0.42 \text{ V}) \text{ vs. NHE}]$$
 (8)

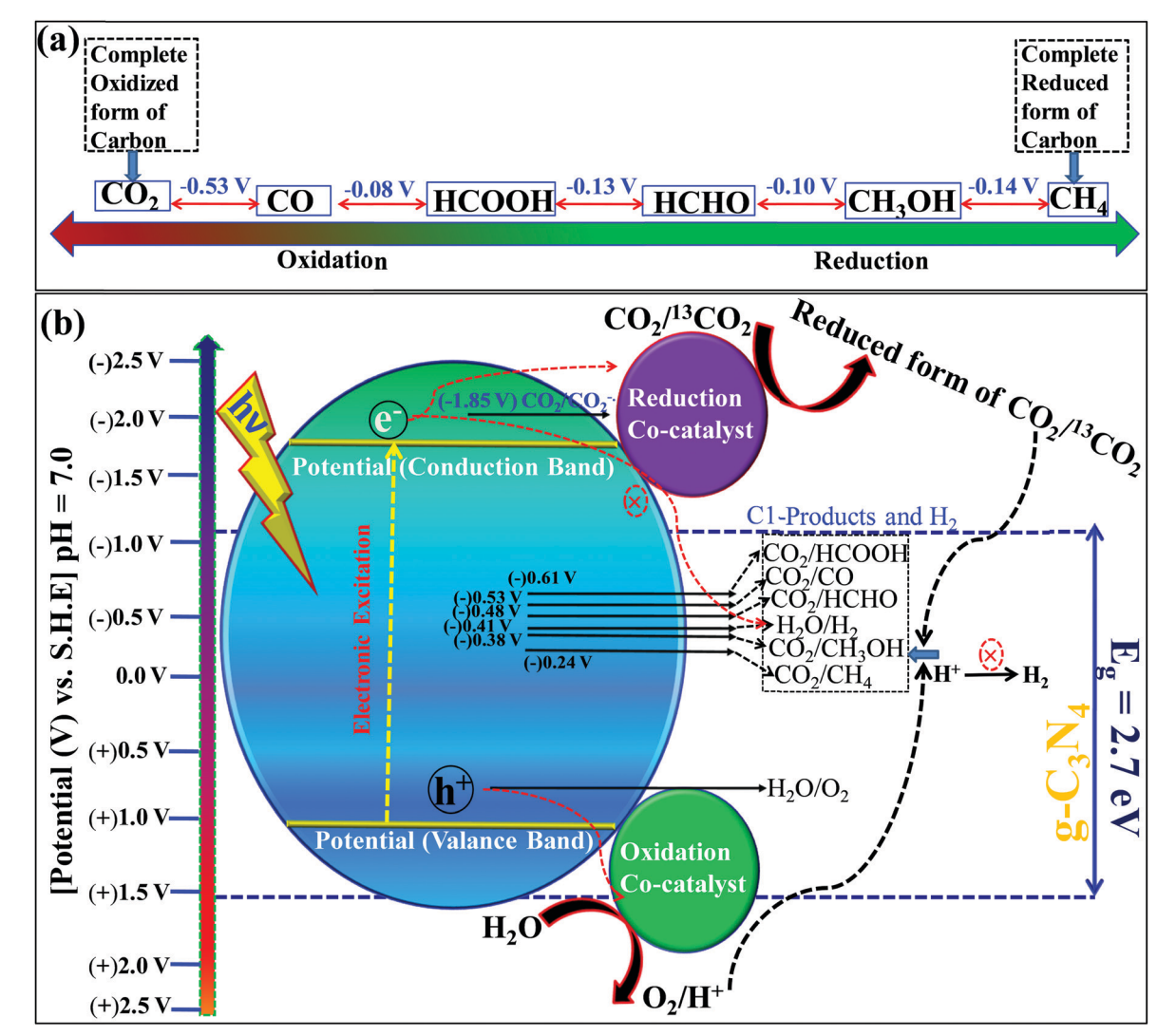
$$2H_2O + 4h^+ \rightarrow O_2 + 4H^+ [E^0 = (+0.81 \text{ V}) \text{ } \nu\text{s. NHE}]$$
 (9)

$$2\text{CO}_2 + 12\text{H}^+ + 12\text{e}^- \rightarrow \text{C}_2\text{H}_5\text{OH} + 3\text{H}_2\text{O} \left[E^0 = -0.329 \right] \quad (10)$$

$$2CO_2 + 12H^+ + 12e^- \rightarrow C_2H_4 + 4H_2O[E^0 = -0.349]$$
 (11)

Among these reactions, eqn (1) is the most unfavorable one and, thus, the proton-coupled electron transfer process always occurs on the catalyst surface with the production of different products.

5.1.2 Reaction mechanism and selectivity control. CO₂ reduction occurs sequentially involving multiple electrons and protons. Also, it requires the splitting of highly stable 'C=O' bonds and the creation of C-H bonds. The complete reduction occurs via the formation of several radical intermediates, which also tend to recombine at different stages during the course of a reaction. 139 The product distribution depends upon the specific set of reaction conditions. The simultaneous and competitive photo-oxidation and reduction reactions bring complexity to CO₂ photoreduction. The most important parameters influencing these reactions include the type of photocatalyst, band edge potentials and bandgap, reaction conditions and medium, co-catalyst, etc., which are briefly described here. The first study reported for CO2 photoreduction involves TiO2 powder under photo-electrochemical conditions. 140 Based on the mechanistic investigation reported in the literature, three possible pathways have been proposed, (I) the formaldehyde pathway forming $CO_2 \rightarrow CH_4$ (fast hydrogenation pathway), (II) the carbene pathway forming CO₂ \rightarrow CH₄ (fast deoxygenation pathway), and (III) the glyoxal pathway (Scheme 14I-III). 131,141 It may be noted that at some stage of the reaction, all the suggested

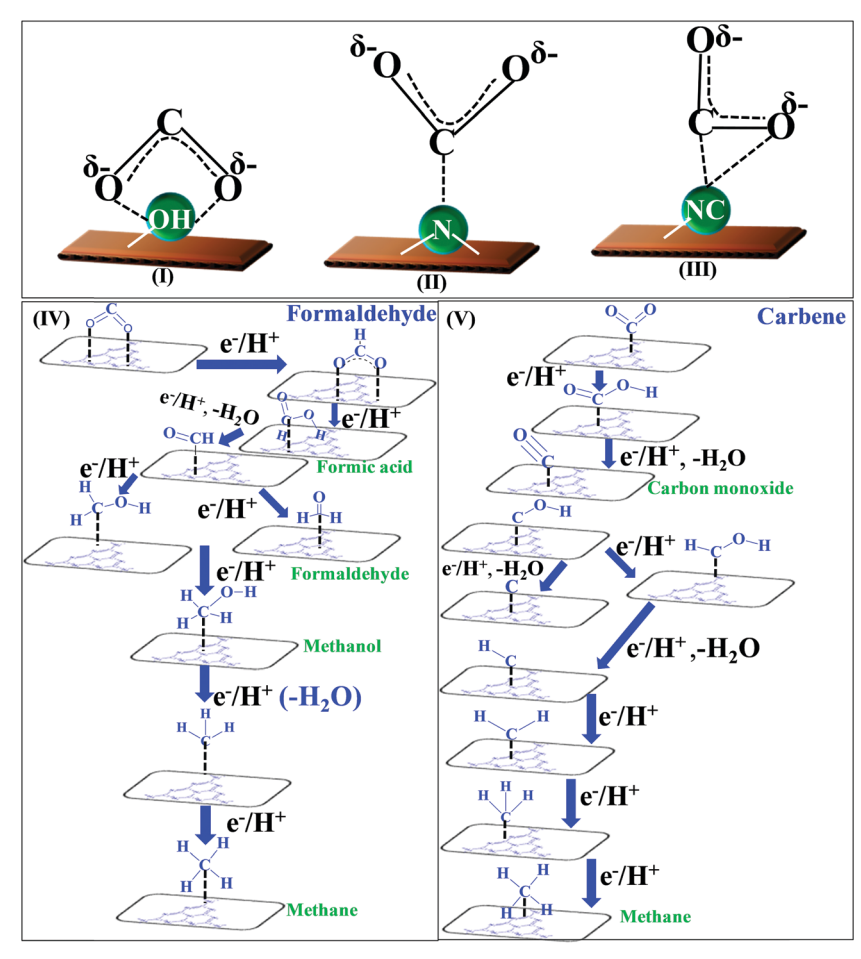


Scheme 13 (a) The different states of carbon with the potential difference, and (b) photocatalytic CO2 reduction with respect to the standard redox potential of different products and band straddling

pathways can equally dominate. The elementary steps based on the specific reaction conditions need more work to establish the possible involvement of several radical species. The abovementioned pathways are specifically discussed here.

The conversion of CO₂ through the formaldehyde pathway involves multiple electrons and protons, which leads to the formation of several products such as HCHO, HCOOH and CH₃OH, and finally the deoxygenated product CH₄. Starting from CO₂ involving 2e⁻/2H⁺, it first produces HCOOH (oxyhydrogenation), followed by involving 2e⁻/2H⁺ again in the next step, which produces HCHO (reductive dehydrogenation). 142 These two species formed during the reaction are intermediates and not side products. They can proceed to form unstable and reactive intermediates like (°CHO)/(°COOH), which in the next step takes up 2e⁻/2H⁺ to produce CH₃OH. CH₃OH can split to form (*CH₃) and (*OH) radicals. (*CH₃) can take one (*H) produced from the cleavage of HCHO to form CH₄ at the end. The formation of CH₃OH/HCHO also depends on the adsorption and desorption energy over the catalyst surface. If the coordination is strong enough and the desorption process is not facile, then CH₃OH/HCHO will be the main product (Scheme 14(IV)). However, a weak binding energy allows this intermediate to produce the completely reduced CH₄. 141 Depending upon the intermediate binding energy, the yields and selectivity are regulated.

If the conversion process of $CO_2 \rightarrow CH_4/CH_3OH$ follows the carbene pathway, then several reactive intermediates can form via de-oxygenation followed by hydrogenation elementary steps. It can propagate like $CO_2 \rightarrow CO \rightarrow ({}^{\bullet}C) \rightarrow ({}^{\bullet}CH_3) \rightarrow CH_3OH/CH_4$. Thus this suggests the following: (1) CO formation and radical formation of (°C) and (°CH₃). (2) In the second step, the competitive reduction tendency between (*CH₃/*C) and (*OH/*H) often determines the product selectivity. In the first step, CO2 is adsorbed on the catalyst surface through carbon co-ordination by the 1e⁻/1H⁺ attachment to form the carboxyl radical (*COOH). After coupling with several e⁻/H⁺, this can undergo decarboxylation to produce the formyl radical (*CHO). In the next step, it can break into (°C) and also can take three protons



Scheme 14 Co-ordination geometry of CO2 over the catalyst surface (I-III), and plausible reaction mechanism of CO2 reduction: formaldehyde pathway (IV), carbene pathway (V).

to produce the (°CH₃) radical intermediate. In the final state, it couples with one H⁺ or (OH) to form CH₃OH or CH₄ as the end product (Scheme 14(V)). 143 The adsorption strength of CO on the catalyst surface also influences the product selectivity. If the CO absorption is very strong then it could lead to the formation of several interim products and, consequently, desorption as different products. But if the absorption is weaker, then the easy desorption produces CO as an exclusive reduced product. In this process, the formation of radical species (*CH₃) and (*C) has been postulated and therefore electron paramagnetic resonance (EPR) measurements are very crucial to obtain a clear understanding of the reaction mechanism.

In the glyoxal mechanism, the first step is the formation of the one-electron reduction of (CO₂^{-•}), which takes 1e⁻/1H⁺ to form the formyl radical (*CHO). This further undergoes dimerization to form the glyoxal product. The complete sequence of the elementary steps involves oxidation and reduction reactions as follows: $(CO_2 \rightarrow CO_2^{-\bullet}) \rightarrow (^{\bullet}CHO) \rightarrow CHO-CHO \rightarrow$ $CH_2OH-CHO \rightarrow (^{\bullet}CH_2-CHO) \rightarrow CHO-CH_3 \rightarrow (CH_3OC^{\bullet}) \rightarrow$ (°CH₃) → CH₄/CH₃OH. However, this process is less explored and not completely understood yet. 144 Various C2 products such as C₂H₅OH or CH₃COOH etc. are believed to proceed through this pathway.

Based on the experimental observation and radical trapping/ detection experiments, mechanistic routes are postulated, which requires further exploration. However, recent theoretical calculations suggest that defects and preferable coordination such as oxygen or carbon binding of the reactant, CO2, over the catalyst frequently determine the selectivity of the obtained product. A defect-less catalyst surface produces CH4 only, while oxygen defect containing g-C₃N₄ catalysts simultaneously form CH₃OH/CH₄. 145,146 This is an interesting observation and more detailed work is required.

5.1.3 Light-harvesting capacity and band straddling. Apparently, 40% is visible radiation within the spectral range of 0.4 to $0.7 \mu m$, 51% is infrared radiation in the spectral region of 0.7 to $4 \mu m$ and 4% is UV radiation of the solar radiation received on the Earth's surface on a sunny day. 147 The total radiation energy emitted by the Sun in unit time remains practically constant. A blue shift of the light-harvesting domain also changes the thermal energy associated with the phonons. However, in a lab-scale reaction system, the most widely used 1.5 AM G light source provides energy equivalent to the energy of 1 Sun, which is 100 mW cm⁻².148 The focus should be on developing materials that absorb in a wide area of the light spectrum and have a bandgap of 1.23 eV or higher so that the kinetic **Materials Advances**

energy to eject electron-hole pairs is sufficient to drive the catalytic reaction. A high light absorption coefficient is also a crucial factor for accelerating the electron-driven reduction reaction. More importantly, if a catalyst possesses a conduction edge position more negative than the standard one-electron reduction potential of CO₂ (eqn (1)), then it would be highly beneficial for this purpose. 149 Moreover, this particular conduction band edge position has been scarcely achieved so far. In standard conditions, the conduction band edge must be located at a more negative potential than the standard reduction potential of $E^0(CO_2/HCOOH) = -0.61 \text{ V } \nu \text{s. NHE, while the}$ valence band edge position should be more positive than the water oxidation potential $E^0(H_2O/O_2) = +0.81 \text{ V } \text{vs. NHE.}^{131}$ Additionally, the competitive H⁺ reduction tendency must be suppressed to achieve better product yield. If the protons derived from water oxidation get reduced simultaneously then the proton coupled electron transfer to reduce CO2 is also hampered. This will be discussed in the latter part. Thus, appropriate band straddling is one of the pivotal criteria in the light energydriven CO2 reduction reaction, similar to the thermal energy provided by heat. The standard electrode potential values for different CO2 reduced products have very little energy difference (Scheme 13b). Therefore, the band edge potentials crucially determine the selectivity of a particular photocatalyst. A generalized tendency is to suppress the back reaction by lowering the valence band position so as to allow the holes to oxidize water molecules efficiently, which provides more electrons to the CO₂ molecules for their effective reduction. Another approach is to make the conduction band more negatively positioned so that competitive reduction could be minimized. Facile and faster hole-electron transfer sometimes appears to be a pivotal factor in the CO₂ photoreduction reaction. If the hole and electron mobility are getting affected, for example, trapping inside the defect sites over the photocatalyst's surface, then they may not reach the reactive sites. This ultimately affects the overall efficiency of the reduction reaction. In general, holes have slower mobility than electrons, which can be tailored by defect site engineering. 150 Accelerating the hole mobility may enhance the OER, which would provide more protons for CO₂ hydro-

5.1.4 Promotional effects of H_2O oxidation. In common practice of CO_2 photoreduction, most of the time the OER is neglected and has been paid less attention. But from a fundamental point of view, it has an equal impact on CO_2 reduction. ¹⁵¹ In ideal conditions, CO_2 behaves as the electron acceptor, while H_2O supplies the electron and proton to the surface-bound partially charged CO_2 . The water oxidation reaction consumes the light-induced holes and, thus, the photogenerated electrons become free to be used in the efficient reduction of CO_2 . Therefore, promoting H_2O oxidation reactions can tune the quenching of light-induced holes, minimizing the charge carrier recombination rate. Thus, sufficient numbers of photogenerated electrons would be made available in CO_2 reduction. Indeed, this promotional OER influences the product selectivity of CO_2 photoreduction.

genation, and thus the selectivity can be controlled.

5.1.5 CO₂-Philicity. CO₂ adsorption on the photocatalyst surface is the very first and crucial step. Higher CO₂ philicity

would provide better catalytic activity. Adsorption is performed at two different temperatures to obtain the CO2 binding energy of a particular photocatalyst. The higher CO2 binding affinity implies its favorable reduction tendency. The adsorption interaction leads to the formation of a partially charged $CO_2^{\delta-}$ species with bent geometry having a lower LUMO level (Scheme 14(I)). 131 Various modes of CO2 adsorption geometry on the surface of photocatalysts are provided in Scheme 14(I)-(III), which are categorized into oxygen coordination, carbon coordination, and mixed coordination. 152 g-C3N4 exhibits bidentate binding with oxygen coordination. Another absorption mode is carbon coordination, resulting in a carbonate-like radical species. When bi-functionality is present in g-C₃N₄, it favors mixed coordination. Different binding modes of $CO_2^{\delta-}$ often decide the reaction pathways. For example, the monodentate binding geometry by the C atom to the Lewis base centers (N atom of -NH2 in g-C3N4) prefers the formation of the carboxyl radical (*COOH). On the other hand, bidentate coordination by two O atoms favors H-bonding to the carbon of CO_2^{δ} , leading to formate anion coordination in bidentate geometry over the catalyst surface. The formation of different interim intermediates greatly influences the reaction mechanism and thus tunes the product selectivity. In g-C₃N₄, surface functionalization with different CO₂-philic molecules like amines, phosphates, sulfates, and hydroxyl groups greatly improves its CO₂ absorption capacity. Moreover, doping or intrinsic surface modification is another promising approach to improve the CO₂-philicity of the g-C₃N₄ photocatalyst.

5.1.6 Effect of the reaction medium. CO₂ photoreduction can be carried out in two different reaction conditions, liquid phase suspension and solid-gas interaction. 153 In the suspension medium, the photocatalyst is dispersed in water medium. In the second one the photocatalyst is immobilized on a solid substrate and then water vapor is introduced through the reactor. In the first case, sometimes a CO₂ miscibility agent like acetonitrile or DMF is used, which is not an ideal reaction condition. The catalyst at the periphery of the reactor would get less light illumination and thus uniform light absorption may not be achieved. Moreover, the symmetrical photocatalyst particle distribution also depends upon mechanical stirring and those particles in the close vicinity of water molecules would contribute more to the resultant catalytic activity. The mixing of acetonitrile or DMF into water raises a question about the actual source of carbon during the CO₂ photoreduction reaction. So in ideal reaction conditions, a solid photocatalyst dispersed in CO2 gas purge-pure water must be considered when performing this reaction to avoid any unwanted products. Besides, in the gas-solid medium, the gaseous CO2 is allowed to react with the immobilized solid catalyst and H2O vapor, which itself is in the gaseous phase. Considering the two states of H₂O and its ease of oxidation either in the liquid state or in the vapor phase, the activity and selectivity are greatly affected. Moreover, in this case, uniform light illumination is reached over the photocatalyst surface. Therefore, the total photons available in the solid-gas interaction are always more than in the case of the liquid-suspension medium. Additionally, the vapor phase of

 $\rm H_2O$ is associated with extra thermal kinetic energy, which is eventually beneficial for overcoming the thermodynamic barriers. While in the first case oxygenated hydrocarbons like $\rm CH_3OH$, $\rm HCOOH$, $\it etc.$ are preferably formed, in the second case complete hydrocarbons ($\rm CH_4$) or oxy-carbons ($\rm CO$) are achieved as products. Thus one should select different reaction media to obtain the desired product.

5.1.7 Impact of the CO₂ source. CO₂ can be directly inserted in the reaction medium from a gas cylinder or it can be in situ generated. The gaseous CO2 is purged into water (pH = 7), which is a typical reaction condition of liquidsuspension medium as discussed in the previous section. It remains in a comparably less activated state than the in situ generated CO₂ from different sources. 139 Moreover, CO₂ can be in situ generated by the reaction between NaHCO₃ and H₂SO₄ or can be activated by employing NaOH. Sometimes elevated temperature and pressure are employed to make the interaction between CO2 and the photocatalyst more kinetically favorable. This, in turn, favors HCO₃ formation and also lowers the pH of the medium (pH < 7). Therefore, the CO₂ reduction follows the proton-coupled-electron-transfer (PCET) mechanism, leading to the formation of a wide range of products. 154 Ideally, employing additional thermal energy or in situ CO2 generation inside the reactor is not a true photocatalytic reaction, but it is preferably used in the electrocatalytic process since NaHCO3 itself acts as a CO2 source as well as an electrolyte.

5.1.8 Influence of the reactor design. The reactor design and fabrication also significantly influence the CO2 photoconversion efficiency. The major aim of designing a suitable photoreactor is to enhance the light-harvesting capacity uniformly, prohibiting the loss of photon energy, facilitating the ease of product separation, and allowing an appropriate interaction between the reactants and light energy with even distribution. 155 Basically, on the lab-scale, photoreactor systems can be classified into two categories: (1) a quartz glass reactor that allows light irradiation from the horizontal direction on the reaction system and (2) a moderately pressurized reactor containing a quartz glass window which can sustain a pressure up to 10 bar CO2 and simultaneously allow light from the vertical direction. In the first case, both the liquidsuspension and the gas-solid system can be operated at atmospheric pressure where the CO2 gas can be purged through a mass flow controller while H₂O vapor is inserted simultaneously. However, in the second case, only the liquid-suspension system can be operated where an external pressure and elevated temperature can be applied to activate the inert CO₂ gas. Since both the reactors involve a difference in their operating process, it is quite obvious that different efficiency and selectivity will be obtained in the two different reactors. 156 In the first case, light is passed through the reactor and therefore the catalyst encountering the light illumination on the front side will exhibit better activity than the backside one. However, in the gas-solid system, it will face the same light illumination with even intensity and so the obtained activity will be uniform. Therefore, the apparent quantum yield would be different depending upon the photoreactor since photocatalysis depends

on the area of illumination and not on the amount of catalyst. Similarly, in the second case, the catalyst at the bottom will get less light exposure and so its activity will be different from the catalyst placed at the top of the reactor. It is not possible to exactly propose the selectivity of the CO₂ photo-reduction products exactly based on the applied reactor. For example, the pressure sustaining reactor allows CO to stay inside the reactor, which may further undergo hydrogenation, leading to the formation of multiple products. On the contrary, in the continuous flow process, lower numbers of reduced products are achieved as it allows the reactant to spend less time inside the reactor.

5.1.9 Effect of sacrificial agents. Ideal CO₂ photoreduction uses water as the medium, where it acts as a sacrificial hole scavenging agent. But this fact totally depends upon the valence band edge position of the catalyst. If the valence band edge potential is more positive than the standard $E^{0}(H_{2}O/O_{2})$, then it can exhibit sacrificial hole scavenging behavior. For the oxidation of one $H_2O \rightarrow O_2$, four holes are required and the produced O2 can act as an oxidizing agent, which has an adverse impact on the CO₂ reduction reaction. ^{141,153} But in several cases, additional sacrificial electron donors like triethanolamine (TEOA), etc. are used to facilitate the hole scavenging process, which makes the electrons free to reduce the CO₂ molecule. The hole induced oxidation of TEOA can also produce CO2 and thus creates a disturbance in the operating reaction conditions. Therefore, the actual source of carbon in the reduced products it inevitably in doubt. Thus, a ¹³CO₂ isotope tracing experiment is also important in those cases where TEOA is used as a sacrificial electron donor. In some cases, H2 gas is used as proton and electron sources respectively. But it is imperative to state that a true CO₂ photoreduction reaction involves H₂O only as a sacrificial electron donor.

5.1.10 Effect of a co-catalyst. Noble metal-based co-catalysts such as Pt, Ag, and Au are widely used over a solid catalyst to add extra momentum to the overall thermodynamics of the CO2 photoreduction reaction. 157,158 This has a severe influence on both the performance and product selectivity of the CO2 photoreduction process. It is well documented that when noble metals like Au, Pt, and Pd are decorated over a photocatalyst, a Schottky barrier is created at the junction. At this interface, the metal nanoparticles act as electron traps and prohibit the recombination of the photo-generated charge carriers. Additionally, plasmonic nanoparticles, specifically Au and Ag, facilitate photocatalysts to harness an extended range of visible light and enhance their photocatalytic performance. Also, the localized surface plasmon resonance induces the injection of hot electrons into the conduction band of the appointed photocatalyst and therefore electron accumulation enhances the CO2 reduction tendency. These exciting features of noble metal co-catalysts are applicable to provide additional benefits in the CO₂ photocatalytic reaction. At the same time, they also enhance the competitive H₂ reduction tendency, which prohibits the CO₂ reduction reaction. But the overall bandgap, as well as the band edge positions, is altered, which provides opportunities to produce different CO₂ photo-reduction products

Materials Advances Review

if it is the case of *ex situ* decoration of noble metals. Another distinctive point to be noted here is that the different affinity towards different interim species over different noble metal nanoparticles truly regulates the product distribution. Since noble metals are costly, their application as a co-catalyst is rather discouraging in ideal reaction conditions. But to obtain better activity and desired selectivity, one can employ such a co-catalyst.

5.1.11 Stoichiometric ratio of reaction consumed electrons and holes against the yield of the products. The stoichiometric involvement of electrons and holes in CO₂ reduction and H₂O oxidation is another important parameter because this will definitely influence the rate of formation of different products after the reaction. For example, the rate of total reactant conversion can be correlated with the rate of the different products formed and the numbers of electrons and holes consumed. For the reduction of 2 CO₂ molecules to produce 2CH₃OH molecules, 12 electrons are required and, at the same instance, 12 holes must be consumed by the water molecules to produce 6O₂ molecules. This is also a feasible thermodynamic concern in the CO₂ photo-reduction reaction, which can provide a meaningful idea about the photo-reduction and light-induced charge consumption during the reaction.

5.2 Graphitic carbon nitride as a CO₂ reduction photocatalyst

The basic phenomenon of CO₂ photo-reduction, especially with respect to heterogeneous catalysis, have already been addressed through several critical, tutorial, perspective, and edge articles by eminent researchers across the globe. Most importantly, CO₂ photoreduction over g-C₃N₄ has also been reviewed recently. Still, various aspects of this material and its further manipulation for CO₂ photoreduction catalytic efficiency improvement remain uncovered.

It is pertinent to mention that g-C₃N₄ has been continuously investigated in different photocatalytic applications since its application as a semiconductor HER photocatalyst by Wang et al. in 2009. However, among the seven different types of polymorphic phases (all are semiconductors), only the g-hheptazine and g-h-triazine phases possess appropriate bandgaps and band straddling to catalyze various photocatalytic reactions. But, a close look at the valence band edge potential and theoretical calculations confirm that only g-h-heptazine fulfills the thermodynamic requirements for water oxidation. 62 Notably, the g-h-heptazine based polymorphic g-C₃N₄ material has been most widely investigated as a photocatalyst with a bandgap of 2.7 eV where the conduction band is situated at (-1.2 V vs. NHE) and the valence band is positioned at (+1.5 V)vs. NHE) at pH = 7. The CB and VB indicate that it is capable of reducing the CO2 molecule and also can oxidize H2O to produce O₂ and H⁺ required for the production of hydrocarbons/ oxygenated hydrocarbons in CO₂ photoreduction. Thus various nanostructured carbon nitrides with diverse morphologies such as nanosheets, microspheres, nanotubes, etc. are proven to be efficient catalysts for CO2 photoreduction. Thermodynamic constraints and optoelectronic limitations are the main bottlenecks of this catalyst for CO2 photoreduction as simultaneous CO2 and H₂ reduction tendencies are observed for this particular catalyst.

Also, the rapid charge recombination and low active surface area are other shortcomings that significantly hamper the efficiency of this catalyst. Strategic improvement of the physicochemical and optoelectronic properties is a pragmatic approach to overcome the poor CO₂ conversion efficiency of pristine g-C₃N₄. In the forthcoming sections, a concise summary of the recent literature reports dealing with CO₂ photoreduction efficiency improvement is compiled to give a clear understanding to researchers actively working in this area.

Dong et al. demonstrated, for the first time, CO2 photoreduction involving porous carbon nitride (PCN) as a catalyst in 2012. 166 In this study, the authors propose that the porosity is introduced in bulk g-C₃N₄ by changing the precursors from melamine to melamine hydrochloride, which exhibits selective CO production of 4.5 mM in 11 h during CO₂ photoreduction. However, on the contrary, the activity of bulk g-C₃N₄ is shown to be better (20.6 mM in 11 h) than porous g-C₃N₄ and this is attributed to the presence of predominant inherent defect sites in PCN compared to bulk g-C₃N₄ that act as charge carrier recombination sites (Table 3, entry 1). 166 However, this adverse trend in the catalytic activity is unfortunately not fully understandable due to inadequate experimental evidence. Microstructure dependent CO2 reduction activity has been reported by Mao et al. The authors have observed that urea derived, mesoporous, flake-like g-C₃N₄ has produced a mixture of oxygenated hydrocarbons (C₂H₅OH and CH₃OH), while melamine derived, non-porous, flaky C₃N₄ has produced CO and CH₄ as products. The varied product selectivity is correlated to the reaction medium NaHCO3 and CO2 gas, where CO2 is available in the activated form (HCO₃⁻), which is more accessible to the catalyst. In this process, O₂ is obtained as a side product and it is established that the holes and electrons are consumed in a close ratio of ~ 1 during the reaction with an apparent quantum efficiency (A.Q.E.) of 0.18% at 420 nm (Table 3, entry 2).¹⁶⁷ The fine-tuning of the product selectivity is also reported in different studies, in which g-C3N4 nanosheets produce CH₄ as a selective product, while the bulk g-C₃N₄ produces CH3CHO. This change in the product selectivity is proposed due to the switching of band edge potentials and also due to the different bandgap values. g-C₃N₄ nanosheets exhibit bandgap enlargement by 0.2 eV, which leads to a more positive valence band edge by 80 meV and a negative shift of the conduction band potential by 120 meV, which are the key reasons behind the different activity and selectivity as compared to bulk g-C₃N₄ (Table 3, entry 3). 168 Thermal polymerization of pre-synthesized urea derived C₃N₄ and red phosphorous (P) has formed a heterojunction and, with the aid of Pt as a co-catalyst, the optimized catalyst (PCN-30) has converted CO₂ to CH₄ with a rate of 295 μ mol h⁻¹ g⁻¹ in the suspension medium. The authors have proposed that the interfacial heterojunction has transferred the electrons from the high position g-C₃N₄ conduction band to a relatively lower position red P conduction band and the holes have been transferred in the reverse direction, which effectively reduces CO2 to CH4 and oxidizes OH to the (OH*) radical, respectively. However, the authors have not emphasized the exact role of Pt involved in the reaction as a co-catalyst

Open Access Article. Published on 15 geassemánnu 2020. Downloaded on 2025-10-16 22:37:22.

BY-NG

This article is licensed under a Creative Commons Attribution-NonCommercial 3.0 Unported Licence.

Table 3 Photocatalytic CO_2 reduction reaction over $g-C_3N_4$ based photocatalysts

		_)										I
		$S_{ m BET} ({ m m}^2 { m g}^{-1}) /$:				13 C					
E. Catalyst no. amount	Catalyst/ amount	precursors and process	Co-catalyst	Reaction conditions and (CO ₂ source)	Light source	Products/rate	Time (h)	isotope CO ₂ tracing pres	isotope CO ₂ tracing pressure Q.E.	Q.E.	Bandgap and band straddling	CO ₂ adsorption	Ref.
1. g-(2. g-($g\text{-}C_3N_4$ (100 mg) — $g\text{-}C_3N_4$ (200 mg) 39.5	39.5	None —	CO_2 gas + H_2O Supercritical fluid grade- CO_2 + NaOH solution		20.6 mM CO in 11 h 11 15.1 µmol CH ₃ OH + 12 10.8 µmol C ₂ H ₅ OH +	111 t + 12 +	No 	1 1	$-$ 0.18% At 420 $\lambda \geq$ nm	8.78 eV $420 \lambda \ge \text{nm} (E_{cb} = -1.23 \text{ eV}, F. \text{not defined})$	1 1	166 167
3. g-C	g-C ₃ N ₄ nano- sheet (100 mg)	(306) dicyandia- mide in thermal oxidation in air	ı	$CO_2 + H_2O$	300 W Xe lamp	$\sim 0.12 \mu \text{mol CH}_4$ and $\sim 0.25 \mu \text{mol}$ CH ₂ CHO	rc	No	0.06 MPa	I	$E_{ m g}=2.97~{ m eV};$ $E_{ m vb}=(+1.85~{ m eV}),$ $E_{ m cb}=(+0.85~{ m eV}),$	ı	168
4. Re g-C (20	Red P doped g-C ₃ N ₄ PCN-30 (20 mg)	(Not provided) urea derived C ₃ N ₄ combined pyrolysis of red P	0.5 wt% Pt	CO_2 gas + H_2O	500 W Xe lamp 295 µmol h ⁻¹	295 μmol h ⁻¹ g ⁻¹	I	No	ı	I	Not mentioned	ı	169
5. CN (8	CN-12-1.5 (8 mg)	(240) (silica hard template/ cyanamide)	Ru co-catalyst CO ₂ gas + (3.9 µmol g ⁻¹) TEOA) sol	Ru co-catalyst CO ₂ gas + (H_2O + (3.9 μ mol g ⁻¹) TEOA) solution	400 W high- pressure Hg lamp	1854 nmol HCOOH	ro	Yes	I	I	$E_{\rm g}$ and $E_{\rm vb}$ not mentioned; $E_{\rm cb} = (-1.29 \text{ V}) vs. \text{Ag/}$ AgCl at pH 6.6	I	170
6. g-C she (30	g-C ₃ N ₄ nano- sheet CNU-BA _{0.03} (30 mg)	(54) thermal polymerization of (urea and barbituric acid)	(CoCl ₂ + 2,2'- bipyridine) as co-catalyst	$(CoCl_2 + 2,2' - CO_2 + H_2O + (TEOA\ 300\ W$ Xe lamp 56.3 μ mol CO bipyridine) as as electron donor) co-catalyst	300 W Xe lamp	56.3 µmol CO	4	Yes	1 atm	I	le	Isotherm provided, binding energy did not mention	171
7. S-I (TC	S-Doped g-C ₃ N ₄ (TCN) (100 mg)	(4.4) thermal poly- 1 wt% Pt merization of thiourea at 520 °C in an ambient environment	1 wt% Pt	(120 mg NaHCO ₃ + 0.25 mL 4 M HCl) \rightarrow (CO ₂ + H ₂ O) vapour	Simulated xenon lamp	Yield 1.12 $\mathrm{CH_3OH}$ µmole g $^{-1}$	м	N _O	1 atm	I	$E_{\rm g} = 2.63$ eV, no data available for band edge potentials	I	172
8. O-l	O-Doped g-C ₃ N ₄ tube (50 mg)	(36) melamine in two-step heating in air and N_2		NaHCO ₃ + H ₂ SO ₄	Not mentioned (420 nm)	Not mentioned 2.6 µmol CH ₃ OH (420 nm)	м	N _O	I	1	$E_{\rm yb} = 2.97 \text{ eV};$ $E_{\rm yb} = \text{not}$ mentioned, $E_{\rm cb} =$ -0.87 eV vs. Ag/	0.045 mmol g^{-1}	173
9. P-Donanananananananananananananananananana	P-Doped g- C ₃ N ₄ nanotube (50 mg)	P-Doped g- C_3N_4 (13.4) melamine nanotube (50 and sodium hypophosphite mono- hydrate in 550 °C $^{\circ}$	I	NaHCO ₃ + H ₂ SO ₄	A high- pressure xenon 7.24 μmol CH ₄ lamp (300 W)	9.48 µmol CO and 7.24 µmol CH ₄	4	S O	1 atm	I	ot	0.39 mmol g^{-1}	174
10. PE g-(10. Phenyl grafted g - C_3N_4 (100 mg)	Phenyl grafted (94.7) thermal g-C ₃ N ₄ (100 mg) polymerization of urea and phenyl urea at 550 °C for 2 h	I	$\begin{array}{l} \mathrm{DMF} + \mathrm{TEOA} + \\ \mathrm{H_2} \mathrm{\ O} + \mathrm{CO_2} \end{array}$	No information available	0.907 μmol CH ₄ + 450 micromole CH ₃ OH + 5 μmol HCOOH	24	No		0.96% using 20 W LED bulb	0.96% using $E_{\rm g} = 2.97$ eV, 20 W LED $E_{\rm cb} = -1.01$ eV, bulb $E_{\rm vb} = +1.65$ calculated from Kulbeka monk	I	175
11. C,	11. C,O co-doped g-C ₃ N ₄ (100 mg)	(50) thermal co- polymerization of (urea + thourea + 2-methyl imidazole)		$(CO_2 + H_2O) + (TEOA Xenon lamp$ – acts as a sacrificial (300 W) electron donor)	Xenon lamp (300 W)	$4.18 \; \mathrm{mmol} \; \mathrm{g}^{-1}$ CH ₃ OH	9	No	1 atm	I		0.69 mmol g^{-1}	110

Open Access Article. Published on 15 geassemánnu 2020. Downloaded on 2025-10-16 22:37:22.

BY-NG

This article is licensed under a Creative Commons Attribution-NonCommercial 3.0 Unported Licence.

Materials Advances

Table 3 (continued)

Ref.	176	177	178	179	180	181	182	183	184	185
CO ₂ adsorption	1	I	Isotherm provided, binding energy did not mention		1	I	1	Isotherm provided, binding energy did not mention	I	Isotherm provided, binding energy did not mention
Bandgap and band straddling	$E_{\rm g} = 2.82 \; { m eV},$ $E_{\rm cb} = -1.10 \; { m eV}$ $\nu_{\rm S.} \; E_{\rm NHE}, E_{\rm vb} = +1.60 \; { m eV}$	$E_{\rm g} = 2.49 \; {\rm eV},$ $E_{\rm cb} = -0.83 \; {\rm eV}$ $\nu_{\rm S}.$ $E_{\rm RHE},$ $E_{\rm vb} = +1.66 \; {\rm eV}$	$E_{\rm g} = 2.63 \; { m eV}$	$E_{\rm g} = 2.53 \text{ eV},$ $E_{\rm vb} = (+1.87 \text{ eV}),$ $E_{\rm cb} = (-0.66 \text{ eV})$	$E_{\rm g} = 2.66 \text{ eV},$ $E_{\rm vb} = (+1.38),$ $E_{\rm cb} = (-1.28 \text{ eV})$	$E_{\rm g} = 2.72 { m eV},$ $E_{ m vb} = (+2.17),$ $E_{ m cb} = (-0.55 { m eV})$	Not provided	Not provided	$E_{\rm g} = 2.35 { m eV}, \ E_{\rm vb} = (+1.45), \ E_{\rm cb} = (-0.90 { m eV})$	$E_{\rm g} = 2.72$ eV, edge potential not mentioned
re Q.E.	(EQE) for CO: 0.11% and 0.03% at $\lambda_{ex} = 360$ and 400 nm	I	I	I	I	0.089%	I	1	I	I
¹³ C isotope CO ₂ tracing pressure Q.E.	I	I	I	1		I		1 bar	2 bar	I
¹³ C isotop tracin	Yes	No.	N _O	o N	No	No	Yes	Yes	No	Yes
Time (h)	24	15	4	Not mentioned	12	∞	÷ +	4	+ rv	4
Products/rate	455 μmol g ⁻¹ CO	284.7 μ mol g^{-1} CO and 51.6 μ mol g^{-1} H ₂	158 µmol CO + 26 µmol H ₂ (86% selectivity)	14 μ mol g^{-1} h + 1.2 μ mol g^{-1} CH ₄ + <1 μ m h^{-1} CH ₃ OH	55.2 μmol CO g ⁻¹	$9.28~\mu mol~g^{-1}~CH_4$	300 W Xe lamp $0.32~\mu mol~g^{-1}$ CH ₄ + 3 with a UV/ 0.45 $\mu mol~g^{-1}$ CO visible cut-off filter	70.63 µmol of CO and 14.99 µmol of H ₂		$300~\mathrm{W}$ Xe lamp $40.3~\mathrm{\mu mol}~\mathrm{g}^{-1}~\mathrm{CO}$
s Light source	$100 \; \mathrm{mW} \; \mathrm{cm}^{-2},$ AM 1.5G, $\lambda > 400 \; \mathrm{nm}$	1 300 W xenon			300 W Xe lamp 55.2 µmol CO) with a UV cut- off filter > 420 nm	a 500 W xenon + arc lamp assembled with a UV cut-off filter (\(\lambda > 400 \text{ nm} \rbrace)		$(\lambda > 420 \text{ nm})$	300 W Xe lamp	
Reaction conditions and (CO ₂ source)	CO ₂ -Saturated (4:1) Xenon lamp, MeCN/TEOA 100 mW cm $^{-2}$ AM 1.5G, $\lambda > 400$ nm	CO ₂ gas saturated in 300 W xenon 5 mL solution (4 mL lamp ACN + 1 mL of TEOA) containing aq. bipyridine (10 mmol L ⁻¹ + 25 (10 mmol L ⁻¹ + 25 CoCl ₂)	CO ₂ gas purged in 300 W xenon 50 mL suspension lamp (420 nr (30 mL ACN + 10 mL cut off filter) TEOA + 10 mL H ₂ O)	(0.084 g NaHCO ₃) + (0.3 mL 2 M H ₂ SO ₄)	CO ₂ gas purged in 300 W Xe lamp (ACN+ TEOA + H ₂ O) with a UV cut- off filter >420 nm	Catalyst coated on a 500 W xenon graphite rod + H ₂ O + arc lamp CO ₂ gas with a UV cut-off filter ($\lambda > 400 \text{ nm}$)	CO_2 and H_2O vapor = $(H_2SO_4$ solution + NaHCO ₃ powder)	CO ₂ gas purged in 5 Visible light mL solution (1 mL $(\lambda > 420 \text{ nm})$ TEOA + H ₂ O)	$H_2O + CO_2$ gas	supercritical fluid- grade CO ₂ gas + H ₂ O
Co-catalyst	СоРРс	Bi-pyridine + CoCl ₂	Co(bpy) ₃ ²⁺ (150 mg 2,2- bipyridine, +10 µmol CoCl ₂)	î 	I	I		Co(bpy) ₃ ² ; 1 μ mol of cobalt chlor- ide (CoCl ₂)+ (15 mg of 2,2- bipyridine)		I
$S_{ m BET} \left({ m m}^2 \ { m g}^{-1} ight) /$ precursors and process	(104) cyandiamide and <i>in situ</i> synthesized cobalt pthalocyanine	(29.5) one step thermal polymerization of cyandiamide and tartaric acid	BA20-CNS-PDA15 (95) silica template nanosphere (not (barbituric acid + mentioned) polydopamine)	(15) (5-amino- tetrazole in a or NaCl/KCl eutectic mixture)	(10.8) (melamine + glucose) water dispersion flowed by heating	(103.1) (melamine and NH ₄ Cl) heating at different temperature	(62.5) one-step calcination boric acid + urea	(109.1) (urea + trimesic acid)	5.3 (dicyandia- mide + KBH ₄) in H ₂ thermal etching	(75) (urea + melamine + DI H ₂ O) hydrothermal treatment at 180 °C for 24 h
 E. Catalyst/ no. amount	12. mpg-CN _x (2 mg) (104) cyandiamide CoPPc and <i>in situ</i> synthesized cobalt pthalocyanine	13. DCN-0.05 (not mentioned)	14. BA20-CNS-PDA15 (95) silica template Co(bpy) ₂ ²⁺ nanosphere (not (barbituric acid + (150 mg 2, mentioned) polydopamine) bipyridine, +10 µmol CoCl.)	15. CN-ATZ-NaK (50 mg)	16. O,C co-doped C ₃ N ₄ (MG ₃) (30 mg)	17. Nitrogen defect- (103.1) (melamine modified g-C ₃ N ₄ and NH ₄ Cl) atomic layers: heating at different (CN ₅₅₀) (amount temperature not mentioned)	18. 1%B/g-C ₃ N ₄ (amount not mentioned)	19. CNU-TM-13.0 (30 mg)	20. B,K-Doped C_3N_4 5.3 (dicyandia- (100 mg) mide + KBH ₄) i H_2 thermal etch	21. Tubular yolk- shell g-C ₃ N ₄ (100 mg)

Table 3 (continued)

Ref.	146	186	187	188	62	189	190	191
CO_2 adsorption	I	I	I	I	<u> </u>	I	No informa- 190 tion available	Theoretical CO_2 adsorption energy $(E_{ads} = -0.0083 \text{ eV})$ at the 100 surfaces of Pd NT
Bandgap and band straddling	$E_{\rm g} = 2.77 \; { m eV},$ $E_{\rm vb} = (+1.67),$ $E_{\rm cb} = (-1.07 \; { m eV})$	$E_{\rm g} = 2.77 { m eV},$ $E_{ m vb} = (+1.68),$ $E_{ m cb} = (-0.54 { m eV})$ ν s. NHE	$E_{\rm g} = 2.83 \text{ eV},$ $E_{\rm cb} = (-1.13 \text{ eV})$ $vs. \text{ NHE, } E_{\rm vb} \text{ not}$ defined	$E_{\rm g} = 2.31 {\rm eV}; E_{\rm vb}$ $= (+1.15), E_{\rm cb} = (-1.16 {\rm eV}) \nu s.$ NHE	$E_{\rm g} = 2.8$ eV, band edge potential not mentioned	No information available	$E_{\rm g} = 2.54$ eV, no information available about g-C ₃ N ₄	$E_{\rm g}=2.75~{ m eV}$
Bs bs	, E.	<u>สู้สุ</u> ฐั	28. P. S. C.	$B_{\rm g} = 0$	$E_{ m g}$	Z &	g a iii. _E	$\mathcal{E}_{\mathcal{E}}$
re Q.E.	I	1		1	1	1	1	
13 C isotope CO_2 tracing pressure Q.E.	1	1	80 kPa	I	I	1 atm	1	
13 C isotope CO_2 tracing pres	N _O	Yes	No	No	S S	No	No	N C
Time (h)	Not mentioned	ಣ	12	4	cs	1	9,	No information available
Products/rate	6.21 μmol h ⁻¹ CO	$1.135~\mu\mathrm{mol~g}^{-1}$ CO	$34.14~{\rm CO~\mu mol~g}^{-1}, 10.42~{\rm \mu mol~g}^{-1}~{\rm H}_2, 1.99~{\rm \mu mol~g}^{-1}~{\rm CH}_4$	\sim 0.7 μ mol CO (using NaHCO ₃ + cyclohexane); \sim 0.15 μ mol CO and \sim 0.23 μ mol CH ₄ (using NaHCO ₃ + 2-methyl-2-butene in toluene)	$\sim 20~\mathrm{ppm}$ CO	\sim 10 μ mol CO, \sim 1.42 μ mol H ₂	CH ₄ 17.09 µmol g ⁻¹ ; CO 4.13 µmol g ⁻¹	2.13 μ mol h ⁻¹ g ⁻¹ No CH ₄ -production rate information of 0.58 μ mol h ⁻¹ g ⁻¹ available
Light source	300 W xenon lamp equipped with a 420 nm cut-off filter	300 W xenon lamp equipped with a $(\lambda = 420 \text{ nm})$	300 W xenon lamp with a UV-cut filter ($\lambda = 420 \text{ nm}$)	lamp	100 W xenon lamp	300 W xenon lamp (\lambda > 420 nm)	300 W xenon lamp	lamp
Reaction conditions and $(\mathrm{CO}_2 \ \mathrm{source})$	(High-purity CO ₂ gas + H ₂ O)	$1M100\;mL$ $NaHCO_3+CO_2\;gas$	CO ₂ gas purged in 300 W xenor (ACN + TEOA + H ₂ O) lamp with a UV-cut filter $(\lambda = 420 \text{ nm})$	Biphasic (1 mL 3 M 300 V aqueous solution of lamp NaHCO ₃) (3 M) and 9 mL cyclohexene (or 9 mL toluene containing 2 mmol of 2-methyl-2-butene)	H ₂ O vapour + CO ₂ gas	1 mL TEOA in 5 mL 300 W xenon solvent (ACN: 3 mL; lamp $_{\rm L_2}$ O, 2 mL), 40 $^{\circ}$ C (λ > 420 nm)	gas) (100 mL $H_2O + CO_2$	(CO ₂ and H ₂ O vapor) 0.084 g of NaHCO ₃ + 0.3 mL of 2 M H ₂ SO ₄ solution
Co-catalyst		1 wt% Au	I	3 wt% Pt	I	eduction (15 mg; 2,2- bipyridine, 1 µmol CoCl ₂)	1	Pd
$S_{ m BET} \left({ m m}^2 \ { m g}^{-1} ight) /$ precursors and process	(89.5) thermal combustion of melamine in air followed by H ₂	annosphole (31.1) urea derived 1 wt% Au C ₃ N ₄ mixed with Na ₂ HPO ₄ followed by heat treatment	(29.4) (melamine + HX) (X = Cl, Br, I) hydrothermal followed by	(2.11) eyanuric choride (CC) + cyanamide (CA) + acetonitrile (ACN) hydrothermal treatment followed by rehydrothemal treatment with 1.14,6-dichloro- 11,3,5-triazin-2-	yilyitetic (rycc) (SA analysis not measured) thermal polymerization of melamine	cd g-C ₃ N ₄ for CO ₂ reduction (133) urea derived (15 mg. 2,2-CN mixed in an bipyridine, 1 ethanolic solution µmol CoCl ₂) of diphenyl diselenide (DDS) followed by	(59.9) urea derived gcG ₃ N ₄ mixed in an ethanolic solution of Mg (NO ₃) ₂ ·GH ₂ O followed by hydro-thermal frequency	urcinia de desirente. Urca derived 9-C ₃ N ₄ followed by seed-mediated polyol-assisted reduction of Na ₂ PdCl ₄
Catalyst/ o. amount	22. Nitrogen (89.5) thermal vacancy combustion of containing C ₃ N ₄ melamine in air (CN-550) atmosuhere	23. Cyano and P-doped g-C ₃ N ₄ (g-C ₃ N ₄ -425) (100 mg)	24. CNX _t (30 mg)	25. Pyrene- (2.11) cyanuric functionalized choride (C.) polymeric cyanamide (C.) carbon nitride acetonitrile (A.) (10% Py-PCN)10 hydrothermal mg treatment follic by rehydrother (1.3,5-triachioro-1.3,5-triachi-2.	26. g-C ₃ N ₄ (catalyst amount not mentioned)	Metal modified/doped g-C ₃ N ₄ for CO ₂ reduction 27. Se-Modified poly- (133) urea derived (15 mg; 2,2-meric earbon CN mixed in an bipyridine, 1 nitride nano- ethanolic solution µmol CoCl ₂) sheets (m-CNNSs of diphenyl diselenide (DDS) followed by	28. Mg-Doped g-C ₃ N ₄ Mg/ PCN-20% (50 mg)	29. CN1/Pd nano- Urea deriver tetrahedron (NT) g-C ₃ N ₄ for (50 mg of the by seed-m catalyst was polyol-ass suspended in reduction 6 mL of DI water Na ₂ PdCl ₄ in a glass
E.	1 6	2	5	4	ē	2 6	2	4

Fable 3 (continued)

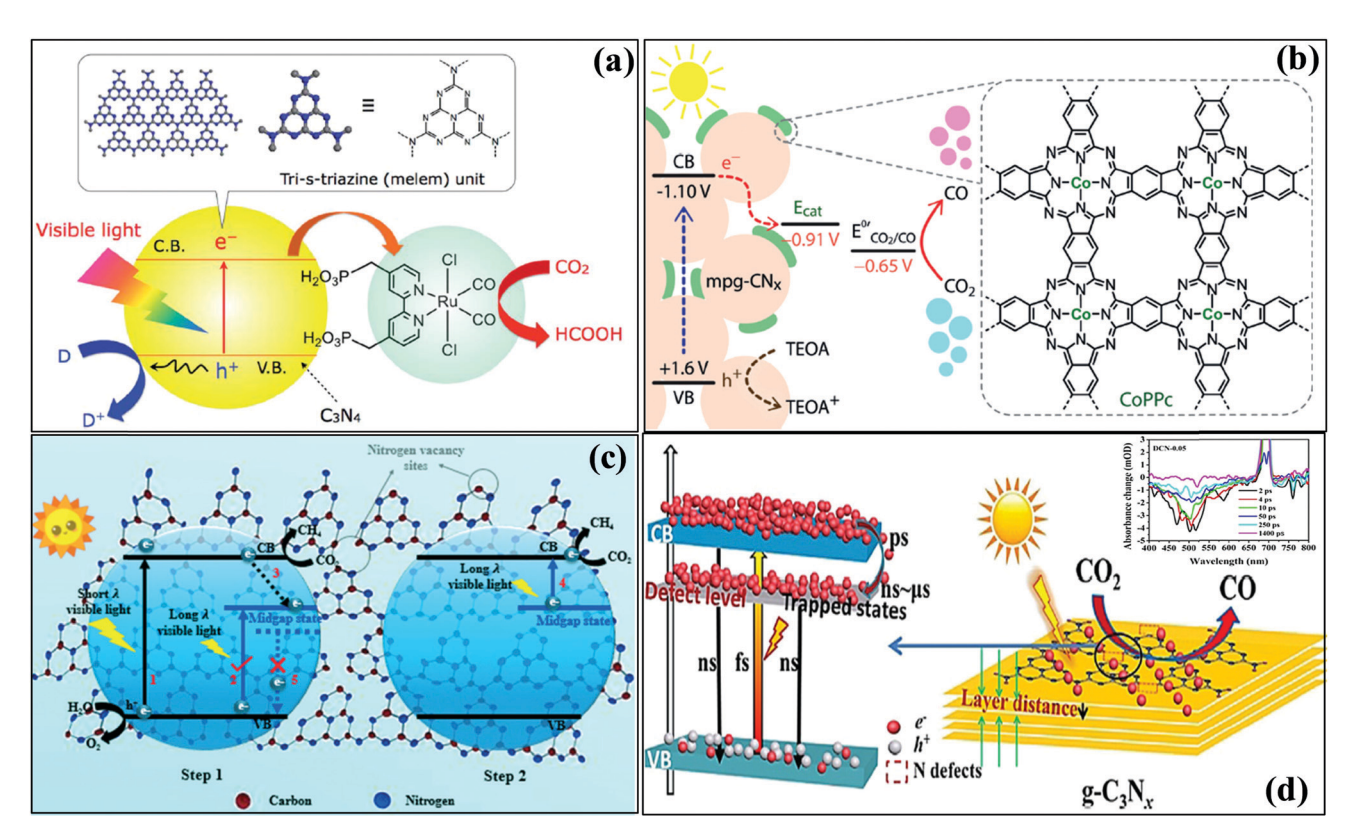
erials Ac	dvances	
Ref.	192	193
Bandgap and CO_2 band straddling adsorption Ref.	$CH_4 \sim E_g = 2.38 \text{ eV}, -2.83\%, E_{\text{th}} = (+1.4 \text{ eV}),$ respectively $E_{\text{ch}} = (-0.98 \text{ eV})$ at $\lambda = 420 \text{ nm}$	$E_{ m g}=2.8$ eV, No information available about $E_{ m cb}$ and $E_{ m bv}$
13 C isotope CO ₂ tracing pressure Q.E.	$CH_4 \sim$ 2.83%, respective at $\lambda =$ 420 nm	I
e CO ₂	1	1
¹³ C isotope CO ₂ tracing press	No	No No
Time (h)	ហេ	10
Products/rate	24 μmol CH ₄	$13.02~\mu\mathrm{mol~g}^{-1}$
s Light source	300 W xe-lamp 24 µmol CH ₄	15 W bulb, the average intensity at the reactor 8.5 mW cm ⁻²
Reaction conditions and $(CO_2 \text{ source})$ Light source Products/rate	$(H_2O + CO_2)$ gas	$(H_2O + CO_2)$ gas
Co-catalyst	ηγ	2 wt% Pt
$S_{ m BET} \left({ m m}^2 { m g}^{-1} ight) /$ precursors and process	Au/P-Doped [lonic liquid g-C ₃ N ₄ (200 mg 1-butyl-3-methyl of the sample imidazoliumhexawas dispersed fluorophosphate in 3 mL H ₂ O) (BmimPF ₆) + dicyandiamide (DCDA)] thermal annealing followed by in situ photoreduction of	translate area 2 wt% Pt was not mentioned) urea derived g-C ₃ N ₄ followed by polyolassisted reduction of H ₂ PtCl ₆
Catalyst/ amount	Au/P-Doped g-C ₃ N ₄ (200 mg of the sample was dispersed in 3 mL H_2 O)	$ ext{Pt/g-C}_3 ext{N}_4$

(Table 3, entry 4). 169 K. Maeda et al. have synthesized high surface area mesoporous g-C₃N₄ using SiO₂ as a hard template and dicyanamide as a precursor by varying the silica/precursor ratio. The dependency of the pore wall geometry on the CO₂ photoreduction activity has been uncovered in this study. Furthermore, the resulting mesoporous C₃N₄ has been grafted with a Ru complex trans (Cl)- $[Ru{4,4'-(CH_2PO_3H_2)_2-2,2'-bipyridine}(CO)_2Cl_2]$, where the electrons from the conduction band of g-C₂N₄ are transferred to the Ru and the bare holes in the valence band of g-C₃N₄ are engaged in the oxidation of water/triethanolamine, thus completing the total redox cycle (Scheme 15a). 170 The best catalyst of this study exhibits the selective formation of 1854 nmol HCOOH in 5 h by involving (H₂O + TEOA + CO₂) in the catalytic system under visible light illumination. The most fascinating outcome of this work is that high surface area is not always beneficial, rather the average surface area (240 m² g⁻¹) with higher pore volume (0.74 cm³ g⁻¹) has minimized the charge carrier recombination and has shortened the electron-hole diffusion to the reactive sites (Table 3, entry 5). 170 J. Qin et al. have investigated the co-polymerization effect of monomer burbutyric acid with urea to synthesize g-C3N4, which eventually extends the pi-conjugated network, engineers the molecular hetero-interface and tailors the optical, surface area and nanostructural properties of g-C₃N₄ semiconductors for CO₂ reduction with the involvement of Co(bpy)₃²⁺ as a co-catalyst and acetonitrile containing triethanolamine solution as a sacrificial electron donor, and CO₂ gas.¹⁷¹ In this study, 56.3 μmol selective CO gas production is achieved in 4 h. ¹³C isotope tracing measurements have confirmed that the CO₂ gas is the sole source of carbon, and, in fact, the control experiment has proved that all the components are essential for triggering CO2 photoreduction (Table 3, entry 6). 171 K. Wang et al. have reported S-doped g-C₃N₄ (TCN) which has been prepared via a simple heat combustion method and first-principles calculations suggest that some of the bi-dentate N atoms of the tris-triazine melem framework are replaced by sulfur during this process, having a narrow gap energy $(E_g = 2.63 \text{ eV})$ as compared to the melamine derived bulk g-C₃N₄ (2.7 eV). The CO₂ photoreduction result demonstrates the selective production of methanol with a yield of 1.25 μ mol g⁻¹ in 3 h from the (NaHCO₃ + HCl) induced (CO₂ + H₂O) vapor medium and Pt co-catalyst (Table 3, entry 7). 172 J. Fu et al. have reported O-doped C₃N₄ nanotubes from controlled thermal oxidation etching which exhibit selective CH₃OH production with a yield of 2.6 µmol in 3 h from a (NaHCO₃ + H₂SO₄) mixture as CO₂ and proton sources, respectively. The oxygen doping causes a lowering of the conduction band by 0.16 eV by substituting the nitrogen atom of the melem unit, as evidenced by theoretical calculations, which is the prime reason for this selectivity control. Moreover, the higher CO2 affinity and CO2 uptake are also supported by CO2-TPD and CO₂-adsorption analysis. The mechanism of methanol formation has also been confirmed by in situ FTIR and GC analysis (Table 3, entry 8). 173 B. Liu et al. have synthesized phosphorus-doped g-C₃N₄ nanotubes through a one-step thermal condensation between melamine and sodium hypophosphite monohydrate, which simultaneously dopes P and introduces surface amino groups. These modifications have led to higher

no.

CO2 uptake and favorable CO2 adsorption, which have been experimentally confirmed by CO2-uptake and zeta potential measurements. The resultant material has converted CO2 to 9.48 µmol CO and 7.24 µmol CH₄ in 3 h. The experimental evidence suggests that phosphorus is interstitially doped into g-C₃N₄ during the synthesis, narrows the bandgap, exhibits a 1D nanotube morphology with high surface area, enhances the visible light absorption, and promotes the separation of charge carriers, which are the inclusive factors for this enhanced catalytic activity (Table 3, entry 9). 174 D. Vidyasagar et al. have synthesized a phenyl grafted g-C₃N₄ scaffold by reacting phenyl urea, melamine, and urea with enhanced pi-pi stacking, which lowers the bandgap and provides a favorable band edge potential for CO₂ photoconversion from (DMF + TEOA + H₂O + CO₂ gas) to produce CH₄, CH₃OH, and HCOOH with a yield of 0.907 µmol CH₄, 450 µmol CH₃OH, and 5 μmol HCOOH in 24 h using a 20 W LED bulb. The achieved apparent quantum yield is calculated to be 0.96% (Table 3, entry 10). 175 S. Samanta et al. have synthesized C, O co-doped C₃N₄ through a thermal poly-condensation of urea, thiourea, and 2-methyl imidazole as starting materials in an air atmosphere. The co-doping has increased the CO₂ uptake, gives a porous cotton-like morphology, lowers the conduction band edge potentials, and also red-shifts the light-harvesting domain. The material converts CO2 gas saturated (TEOA + H2O) solution to methanol with a yield of 4.18 mmol g⁻¹ in 6 h under visible light illumination. More importantly, theoretical calculations have provided favorable evidence about the high CO2 binding energy after C, O co-doping, which is also supported by CO2-TPD and CO2adsorption studies (Table 3, entry 11). 108 In interesting work, A. Roy et al. have synthesized a cobalt phthalocyanine (CoPPC) grafted polymeric graphitic carbon nitride photocatalyst in which the favorable CO₂ electro-reduction capability, as well as the light sensitization properties of cobalt phthalocyanine, has been emphasized. Combining the characteristic features of C₃N₄ and CoPPc enables the material to reduce CO₂ to CO in organic solvents (ACN + TEOA) under UV/vis light (AM 1.5 G, 100 mW cm⁻², $\lambda > 300$ nm) with a cobalt-based turnover number of 90 for CO after 60 h. More interestingly, in complete aqueous phase reaction conditions, the catalyst exhibits 60 µmol CO corresponding to a TON of 5.1 per CO. When the reaction condition is changed by keeping acetonitrile fixed and replacing TEOA with 10% H₂O the activity is reduced to 41%, indicating phase separation in aqueous medium (Table 3, entry 12). Table 3. acts as an electron acceptor and lowers the conduction band edge potential of the overall system (Scheme 15b). A ¹³C isotope experiment fully agrees that CO₂ gas is the only source of CO in the reaction. The external quantum efficiency (E.Q.E) of CO is 0.11% and 0.03% at λ_{ex} = 400 and 360 nm, respectively (Table 3, entry 12). 178 Very recently, a 2D g-C₃N₄ nanosheet has been prepared via one-step tartaric acid-assisted thermal polymerization of dicyandiamide having nitrogen vacancies (g-C₃N_x) with preferential location at both three-coordinate N atoms and uncondensed terminal NH_x species. The material has produced 284.7 μ mol g⁻¹ CO and 51.6 μ mol g⁻¹ H₂ from the CO₂ gas dissolved in (TEOA + ACN) solution and Co(bpy)₃²⁺ as a co-catalyst in 15 h. The charge carrier migration and utilization

are demonstrated with transient absorption spectroscopy (Table 3, entry 13) (Scheme 15d). 179 M. Li et al. have synthesized polydopamine and barbituric acid co-modified carbon nitride nanospheres through thermal silica template-polymerization followed by a post-modification method, which has produced 158 μmol g⁻¹ CO and 28 μmol H₂ from CO₂ gas dissolved in aqueous (TEOA + ACN) solution and Co(bpy)₃²⁺ as a co-catalyst in 4 h using a 300 W xenon lamp (visible light). The co-modification tunes the band edge potentials and favors CO₂-adsorption, which are the key factors for the activity improvement (Table 3, entry 14). 180 J. Zhang et al. have synthesized grain boundary controlled carbon nitride using 5-amino tetrazole as a high nitrogen-containing organic compound and NaCl/KCl. The synthesized catalyst (CN-ATZ-NaK) exhibits 14 μ mol g⁻¹ h⁻¹ CO, 1.2 μ mol g⁻¹ h⁻¹ CH₄, and <1 µmol g⁻¹ h⁻¹ CH₃OH production rates from an activated CO₂ source (NaHCO₃) and H₂SO₄ as a proton donor. The grain boundary tailoring is the main reason for this impressive catalytic activity (Table 3, entry 15).181 Another carbon and oxygen co-doped g-C₃N₄ has been achieved by aqueous dispersion of glucose with melamine followed by thermal treatment. The resultant optimized material has produced 55.2 μ mol CO g⁻¹ with nominal amounts of CH4 and CH3OH under visible light from CO₂ dissolved in a (TEOA + ACN + TEOA) reaction mixture in 12 h. Simultaneous co-doping has improved the visible light absorption and given fast electron extraction, which are responsible for this activity enhancement (Table 3, entry 16). 182 Very recently J.-Y. Tiang et al. have synthesized nitrogen-vacancy enriched carbon nitride by two-step thermal copolymerization between NH₄Cl and melamine in a controlled environment, which induces mid-gap band state dangling between the conduction and valence band edge positions. The material has produced 9.28 µmol g⁻¹ CO in 8 h in the presence of a catalyst-coated graphite rod and (CO₂ + H₂O) vapors under visible light illumination. The main reasons underlying this enhanced CO2 reduction activity are the introduction of dense nitrogen vacancies, extended light absorptivity of visible light leading to a wide range of light wavelength due to the strategic mid-gap arising, and prolonged lifetime of the charge carriers trapped inside the midgap. The obtained apparent quantum efficiency is calculated to be 0.089% (Table 3, entry 17) (Scheme 15c). 183 J. Fu et al. have reported boron as a dopant that induces charge localization inside the cavity of tris tri-azine by the interaction with the two co-ordinated $-(N)_2$ at the interstitial position. This claim is also justified by DFT calculations. The resulting 1%B/C₃N₄ has produced 0.32 μmol g⁻¹ $CH_4 + 0.45 \mu mol g^{-1} CO from (CO_2 + H_2O)$ vapor under visible light irradiation in 3 h. A ¹³C isotope tracing experiment has supported the CO intermediate end product CH₄ formation (Table 3, entry 18) (J. Fu et al., 2019). Trimesic acid-modified g-C₃N₄ (CNU-TMU-13) has been synthesized via a thermal combustion method which produces 70.63 µmol of CO and 14.99 μmol of H₂ in 5 h from aqueous TEOA saturated with CO₂ gas and $Co(bpy)_3^{2+}$ as a co-catalyst. The origin of the carbon in the produced carbon is analyzed by a ¹³C isotope experiment and high CO2 uptake is also in favor of the surface modification



Scheme 15 (a) CO_2 photoreduction over (a) Ru-complex grafted $g-C_3N_4$, reprinted with permission, Copyright Royal Society of Chemistry, ref. 172; (b) $Co(bpy)_3^{2+}/g-C_3N_4$, reprinted with permission, Copyright John Wiley and Sons, ref. 178; (c) N-vacancy containing $g-C_3N_4$ with a midgap state, reprinted with permission, Copyright Royal Society of Chemistry, ref. 183; and (d) defect and trap state containing $g-C_3N_4$, reprinted with permission, Copyright John Wiley and Sons, ref. 179.

by trimesic acid, leading to high catalytic activity (Table 3, entry 19). 185 Simultaneous B, K co-doped g-C₃N₄ has been synthesized using dicyandiamide and KBH4 under an H2 thermal etching process, which has accelerated the CO2 reduction activity with the formation of 5.93 μmol g⁻¹ CH₄ and 3.16 μ mol g⁻¹ CO from CO₂ dissolved in H₂O in the absence of any co-catalyst, electron donor, or CO2 miscibility agent like DMF or acetonitrile in 5 h under visible light. This is also ascribed to the creation of nitrogen-vacancies and the incorporation of B and C together according to the reported theoretical simulation (Table 3, entry 20). 186 The morphology also has a great impact on photocatalytic CO2 reduction. Tubular yolk-shell g-C₃N₄ has been hydrothermally synthesized from melamine and urea at 200 °C. The material has produced 40.3 μ mol g⁻¹ CO in 4 h from super-critical grade CO₂ and H₂O. The formation of CO is also analyzed by a ¹³C isotopic experiment. This catalytic improvement is correlated to the higher CO₂ uptake as evident by the CO₂-uptake profile and also due to the obtained tubular morphology (Table 3, entry 21). 187 Another study reports the synthesis of nitrogen-vacancy containing C₃N₄ through the controlled polymerization of melamine in different atmospheres, which selectively produces 6.21 µmol h⁻¹ CO from the catalyst suspension medium of CO2 and H2O under visible light illumination (Table 3, entry 22).146 The replacement of nitrogen has profoundly controlled selective CO production, which is established via DFT calculations (Table 3, entry 22). 146 In a very strategic approach, X. Liu et al. have synthesized cyano-groups and phosphorus-doped C₃N₄ by treating pre-synthesized carbon nitride with NaH₂PO₂ under an argon atmosphere at different temperatures. The authors have proposed and proved that the thermal decomposition of NaH₂PO₂ produced PH₃ gas, which itself was doped as phosphorus and was also accountable for the conversion of the terminal, uncondensed = C-NH₂ to -CN groups during the synthesis process. In fact, the attachment of -CN groups served as electron-withdrawing groups over the carbon nitride surface, which benefited CO₂ activation. The phosphorus doping has enlarged the light absorption and has inhibited photogenerated charge recombination. The active material (g-C₃N₄-425) has converted NaHCO3 saturated CO2 gas to CO with a yield of \sim 1.14 μ mol g⁻¹ in 3 h using 1 wt% Au as a co-catalyst under a 300 W xenon lamp (Table 3, entry 23). 188 S. Wan et al. have prepared hexagonal tubular carbon nitride by the heat treatment of the supra-molecular organization of the in situ hydrogenbonded melamine cyanuric acid assembly under hydrothermal conditions. Hydrogen fluoride is found to be the best suitable haloic acid (H-X; X = F, Cl, Br, I) that promotes the dissolution of melamine, which eventually facilitated the pi-pi stacking as evidenced by the intense EPR spectra. The light absorption has been blue-shifted and charge separation is maximized with HF. The best active catalyst has produced 34.14 CO μ mol g⁻¹, 10.42 μ mol g⁻¹ H₂, and 1.99 μ mol g⁻¹ CH₄ in 12 h under

visible light from 0.8 bar CO2 gas pressure dissolved in a mixture solution of (acetonitrile + TEOA + H2) (Table 3, entry 24).189 The authors have also calculated the average electron consumption rate (R_{electron}) during the CO₂ reduction reaction as equal to 8.96 mol g^{-1} h⁻¹ on the basis of the equation $R_{\rm E} = (2R_{\rm H_2}) + (2R_{\rm CO}) + (8R_{\rm CH_2})$, where R is the rate, expressed in µmol g⁻¹ h⁻¹ (Table 3, entry 24). 189 For the first time ever, the stability aspect of g-C₃N₄ in the CO₂ photoreduction reaction has been investigated in-depth by F. R. Poimilla et al., in which the authors provide insights about the stability of the melem framework before and after catalytic activity evaluation (Table 3, entry 25).62 They have synthesized g-C₃N₄ by following a two-step thermal polymerization of melamine. For comparison purposes, they have also synthesized O-doped g-C₃N₄ by treating carbon nitride with H₂O₂. They observed a marginal difference in the catalytic activity after repetitive cycles. In gas phase CO2 reduction, the catalyst exhibits 20 ppm selective CO in 5 h under 100 W xenon light (Table 3, entry 25).⁶² But, surprisingly, CO is obtained even in the absence of CO2 gas under light illumination, which raised the question about the origin of carbon from the graphitic carbon nitride photocatalyst. In association with detailed optoelectronic and physicochemical measurements and also with controlled analysis, the authors concluded that the photo-corrosion rather than the thermal decomposition of melamine is responsible for this unexpected behavior of the catalyst under their experimental conditions. In another breakthrough, X. Gong et al. have synthesized pyrene functionalized graphitic carbon nitride, which endows biphasic CO2 reduction combining CO₂ reduction by the electrons in the aqueous phase and hole generated (OH) radical-induced olefin oxidation in the organic phase. The process of accessibility of the organic olefin into the aqueous system is facilitated by the increased lipophilicity of the grafted pyrene-functionality over g-C₃N₄. The authors have achieved ~0.7 μmol CO from (NaHCO₃ + cyclohexane) and $(\sim 0.15 \mu mol CO + \sim 0.23 \mu mol CH₄)$ from (NaHCO₃ + 2-methyl-2butene in toluene) under 300 W xenon light illumination in 4 h

Various noble and non-noble metal modified carbon nitrides also exhibited profound CO₂ reduction catalytic activity. H. Ou et al. have prepared selenium modified thin g-C₃N₄ porous nanosheets (m-CNNS_S) using pre-synthesized g-C₃N₄ in an ethanolic solution of diphenyl diselenide (DDS) followed by thermal polymerization. The evolution of $\sim 10 \mu mol\ CO$ and $\sim 1.42 \mu \text{mol H}_2$ is obtained over this catalyst from a reaction mixture containing (TEOA + acetonitrile + H2O) at 40 °C in 1 h using 420 nm light irradiation using Co(bpy)₃²⁺ as a co-catalyst (Table 3, entry 27). 191 The role of selenium is investigated with density of state calculations, which evidences that selenium has narrowed the conduction band by creating an electronic distribution with the conduction band of CN. But it has not hampered the conduction and valence band composition as its Fermi level exists in the middle of the CB and VB level of g-C₃N₄ J. Tang et al. have synthesized Mg-doped g-C₃N₄ considering the high CO₂ philicity of MgO and the light-harnessing capacity of the Mg²⁺ ions in natural chlorophyll. The synthesized material has produced 17.09 μmol g⁻¹ CH₄ and 4.13 μmol g⁻¹

(Table 3, entry 26). 190

CO from CO₂ gas saturated H₂O under a 300 W xenon lamp in 6 h (Table 3, entry 28). 192 Though the light-harvesting capacity is enhanced, they did not emphasize the CO2 uptake phenomenon with any experimental evidence. S. Cao et al. have prepared Pd nano-tetrahedron doped g-C₃N₄ from urea derived g-C₃N₄ followed by seed-mediated polyol-assisted reduction of Na₂PdCl₄. They focused on the facet dependent CO₂ reduction catalytic activity of Pd NT/g-C₃N₄, which exhibits a CH₃OH and CH₄ production rate of 2.13 μ mol h⁻¹ g⁻¹ and 0.58 μ mol h⁻¹ g⁻¹ respectively, from activated (CO₂ + H₂O) vapor under 300 W visible light illumination (Table 3, entry 29). 193 Furthermore, DFT calculations confirm that the Pd(100) facet over g-C₃N₄ exhibits high CO₂ uptake and high CO₂ binding energy and thus facilitates CH3OH desorption. M. Humayun et al. have synthesized Au NP loaded P-doped g-C3N4 in ionic liquid followed by thermal annealing of a mixture of [1-butyl-3methyl imidazoliumhexafluorophosphate (BmimPF₆) + dicyandiamide (DCDA)] and then finally the *in situ* photoreduction of HAuCl₄ for the decoration of Au NPs. The catalyst exhibits selective CH₄ evolution of 24 µmol in 5 h from CO₂ gas saturated H₂O under 300 W visible light (Table 3, entry 30). 194 The calculated quantum efficiency for CH₄ formation at 420 nm is \sim 2.83%. The impressive catalytic activity is ascribed to the extended visible-light absorption along with the improved charge carrier separation via the phosphorus induced surface states and the Au nanoparticle decoration. The impact of Pt on the CO2 reduction over g-C3N4 is revealed by W.-J. Ong et al., using 2 wt% Pt loaded g-C₃N₄ nanocomposites. The catalyst exhibits the highest CH_4 yield of 13.02 μ mol g^{-1} catalyst $^{-1}$ after 10 h of light irradiation, which is 5.1-fold higher in comparison with pure g-C₃N₄ (2.55 μmol g⁻¹ catalyst⁻¹), from CO₂ gas dissolved in H₂O under a 300 W xenon lamp (Table 3, entry 31). ¹⁹⁵ The enhancement in the photocatalytic activity of the Pt/g-C₃N₄ nanocomposite for CO2 photo-reduction CH4 production can be attributed to the enhanced visible light absorption and smooth interfacial photogenerated electron transfer from g-C₃N₄ to Pt by lowering the Fermi level of Pt in the Pt/g-C3N4 hybrid as evidenced by the UV-vis and photoluminescence studies. The accumulated electron density on Pt facilitates the reduction of CO₂ to CH₄ via a multi-electron transfer process.

5.3 Critical factors regarding catalytic activity assessment and result presentation

Amidst the CO_2 photoreduction reports published in several journals, there is great concern regarding the precise catalytic activity evaluation, supportive characterization, and data presentation. Despite addressing this matter in several perspectives, edge articles, and editorials, this problem still persists. $^{196-200}$ Although the intention is not to indicate or draw attention to any inappropriateness about the results reported on g-C₃N₄ for CO_2 photoreduction, the aim is to emphasize and regulate the standard requirements for a particular report that can be followed precisely by the readers. The following points may be considered during an experiment and result presentation. If g-C₃N₄ is the appointed photocatalyst, the abundance or source of carbon in the resultant product may be ensured with

Materials Advances

a ¹³C isotope tracing experiment since the catalyst itself is a carbonaceous material which eventually may be contributing as a carbon source. The amount of catalyst and co-catalyst may be clearly mentioned; otherwise, it is hard to follow since only the amount of catalyst can decide the rate of product formation and TON/TOF calculation. For obtaining the CO2 reduction mechanism, in situ/DRIFT IR, HPLC, and GC-MS are the standard requirements that may be carried out. Since the activity is solely dependent on the CO₂-uptake capacity, therefore as a matter of fact CO2-adsorption and CO2-TPD analysis may be considered. The binding energy of CO₂ over the catalyst surface will also provide useful information. Pre-requisite knowledge about the applied light source and especially the cut-on/off filter is also a vital factor. A cut-off filter implies the upward wavelength above the specified wave-length and vice versa in the case of a cut-on filter. The apparent quantum yield may be reported using monochromatic light only otherwise it is not appropriate to report as per the definition of the quantum yield. On many occasions, it has been reported by considering a range of wavelengths, which has no real scientific significance. For comparative purposes, only the quantum yield is a parameter suitable for consideration, since the activity and rate are definitely variable factors depending on the type of the photo-reactor and the amount of the catalyst used. Also, when the quantum yield is mentioned, the time must be mentioned as with the progress of the reaction the yield also increases and thus it is a collective parameter. Consequently, the product yield may not be reported like $\mu/\text{mmol g}^{-1}$ h⁻¹ as the amount and time are two variable factors. Also, the catalytic activity is not always linearly enhanced with time or amount. For example, catalysts which are close to the surface of the exposed site of incoming light illumination will exhibit better activity than a bulk amount settled at the bottom of the reactor. It is always advisable to report only the amount of product formed along with specifying the other reaction parameters. Also for comparison purposes, the solid-gas phase induced CO2 reduced products may not be compared with the suspension medium even in the case of the same catalyst since the entire reaction condition is different, and thus it is not at all comparable. A minor alteration can change the entire catalytic investigation, which would mislead the readers. Therefore, these cumulative

5.4 Device fabrication using g-C₃N₄-based materials in photocatalysis

points may be considered during and after performing any CO₂

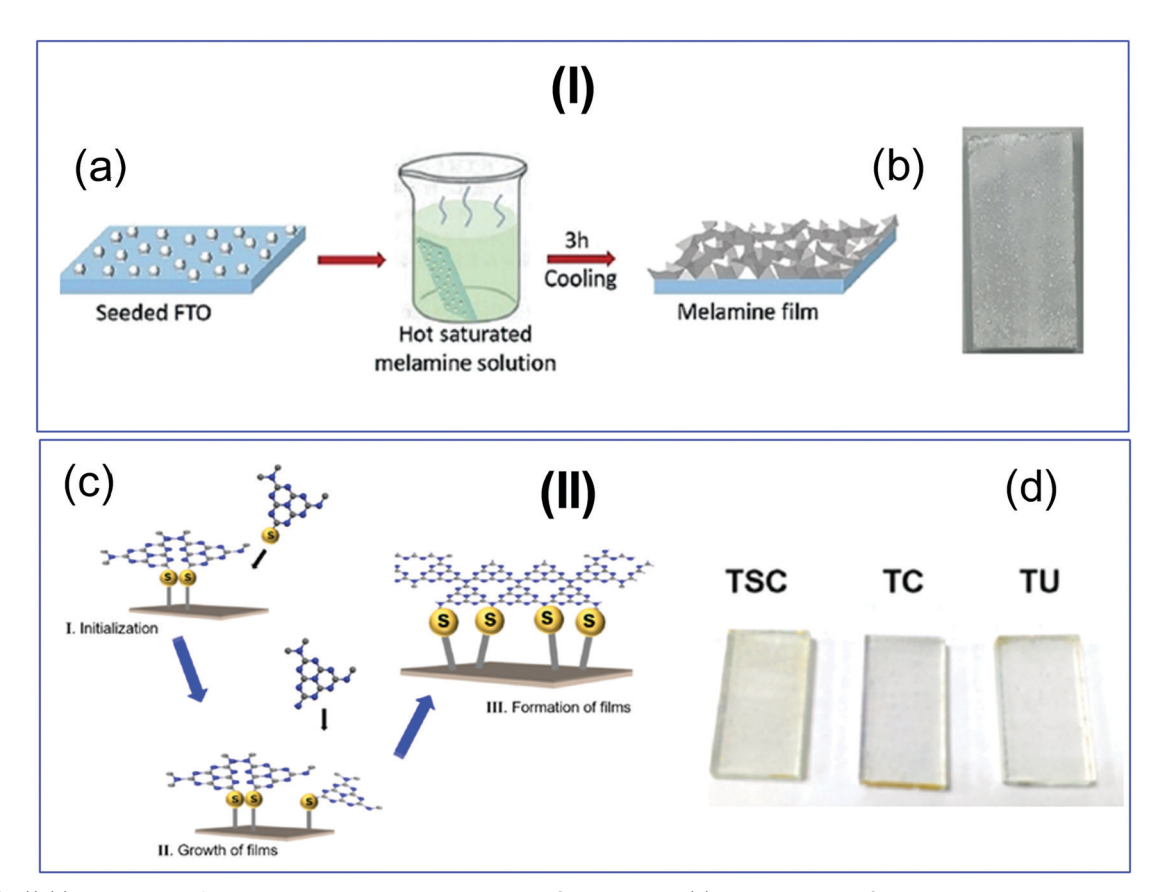
Miniaturization of the photocatalytic process via device fabrication is an important step towards industrial deployment that fulfills social demands. The progress in this direction over g- C_3N_4 catalysts is very little explored. Moreover, a g- C_3N_4 based device for the photocatalytic CO_2 conversion to C_1 fuel is not yet reported to the best of our knowledge. The effective device ideally should have provisions for (a) CO_2 capture and (b) its conversion to C_1 fuels under natural sunlight, on-board, in the same unit. Powder g- C_3N_4 -induced suspension photocatalysis may not be suitable for this purpose. The catalyst effectively

captures solar photons when it is fabricated as a film. Therefore, coating g-C₃N₄ powder over a conducting surface like fluorine-doped-tin oxide (FTO) or synthesis of a layer by layer free-standing g-C₃N₄ thin film can accomplish this requirement. Therefore, significant efforts are required to develop a prototype for the industrial-scale conversion of CO₂ to fuel. However, one can get some insight from the already developed g-C₃N₄ based devices for photoelectrochemical (PEC) watersplitting. 201-204 G. Peng et al. have reported a robust seedgrowth method for the synthesis of a layer-packed crystalline g-C₃N₄ film on FTO using melamine as a precursor for carbon nitride followed by heating at high temperature (Scheme 16(I)). 201 The fabricated device exhibited an outstanding photocurrent density of 116 A cm⁻² vs. RHE without any sacrificial agent in a wide pH range (0-13). The same author has reported a free-standing g-C₃N₄ paper-based electrode for hole-driven photoelectrochemical dye degradation at the anode and electron-driven H2 gas production in a single setup. Here, the authors have used carbon paper instead of FTO, and this is considered to be a proof of concept for the simultaneous utilization of holes and electrons to perform disproportionation reactions.202 The very same group reported a graphene oxide (GO) coupled crystalline carbon nitride film in an FTO photoelectrochemical cell for the water splitting reaction. This time, different amounts of GO and melamine were mixed in ethylene glycol by varying the contents, and then the resulting paste was thermally annealed at high temperature. The fabricated cell produced a photocurrent density of 124 μ A cm⁻² vs. RHE in the absence of a sacrificial agent under alkaline solution. Moreover, the fabricated cell has performed with long-standing durability, which could be attributed to the smooth junction formation between GO and g-C₃N₄, efficient charge separation, high electronic conductivity, and sizeable electrochemical surface area. 203 In other exciting work, Y. Feng et al. have reported an adhesive interface containing a polymeric g-C3N4 film-based device for solar water splitting (Scheme 16(II)). 204 The authors found that both sulfur and non-sulfur precursors are necessary to achieve a high current density of 100 μA cm⁻² vs. RHE in NaOH electrolyte. g-C₃N₄ based device fabrication for PEC has recently been reviewed, and this could be very helpful in designing a prototype for photocatalytic CO₂ conversion to C₁ fuel or related applications. 205,206

6. Electrocatalytic CO₂ reduction reaction (e-CO₂RR)

The electrocatalytic reduction of carbon dioxide into clean fuels is not fairly straightforward. In the last two decades, several research groups have studied purely metallic electrodes for this purpose and have segregated them based on the products that are obtained during the electrocatalytic CO₂ reduction reaction (e-CO₂RR) and the photoelectrocatalytic CO₂ reduction reaction (pe-CO₂RR). There are three major steps involved during the heterogeneous catalytic conversion of CO₂ on the electrode surface: (i) adsorption of the originally linear CO₂ molecule

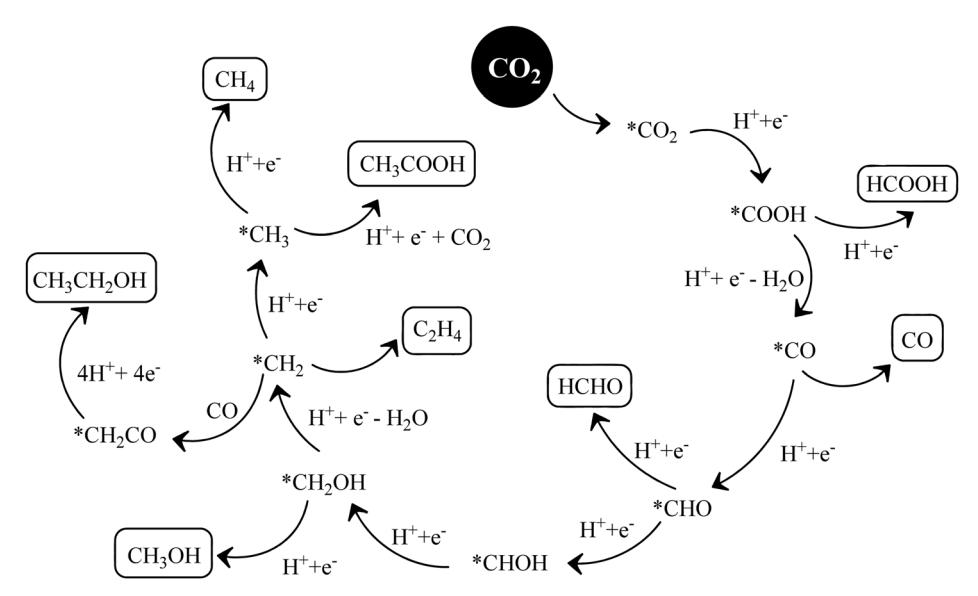
photoreduction reaction.



Scheme 16 (I) (a) Fabrication of a crystalline carbon nitride based-PEC device, and (b) the resultant FTO based device, reprinted with permission, Copyright John Wiley and Sons, ref. 201; and (II) (c) a polymeric carbon nitride-based adhesive connected-PEC device, and (d) corresponding images of the FTO coated PEC devices synthesized from different precursors: TSC-thiosemicarbazide, TC-tri-thiocyanuric acid, TU-thiourea and urea, respectively, reprinted with permission, Copyright American Chemical Society, ref. 204.

on an electrode material with the loss of its absolute linearity; (ii) cleavage of the C-O bonds to form C-H bonds by electron transfer and/or proton migration processes; and (iii) desorption of the product preceded by configurational rearrangement and

followed by diffusion into the electrolyte. 207 Further, it is found that both the e-CO₂RR and pe-CO₂RR involve multiple steps with overall two-, four-, six-, or eight-electron transfer processes (Scheme 17).208 Naturally, the range of products that form



Scheme 17 Various products formed due to multi-step processes during electrochemical CO2 reduction.

Materials Advances Review

during such processes is diverse. They include carbon monoxide, formic acid or formate, formaldehyde, methanol, ethanol, methane, ethylene etc. The half-cell reactions involved in these processes along with their standard electrode potentials have already been listed in Section 5.1.1.

6.1 The various rudiments of an e-CO₂RR experiment

Based on the mechanistic pathways of the abovementioned processes, electrocatalysts can be tailored for efficient performance and high selectivity. The performance of various electrocatalysts can be judged by electrochemical techniques such as linear sweep voltammetry (LSV), cyclic voltammetry (CV) and electrochemical impedance spectroscopy (EIS). While the overpotentials can be calculated for different products at various current densities directly from the LSV and CV profiles, the kinetics can be understood using the Tafel slopes that can be derived from the relevant voltammograms and/or the impedance spectra. All experiments should be performed using a two-compartment H-shaped electrochemical cell separating the cathode and the anode. This separation can be achieved using a thin frit glass membrane or a semi-permeable conducting membrane such as that of Nafion. A detailed gasleak-proof setup design has been proposed by Pander et al. 209 Since e-CO₂RR involves the reduction of CO₂, the working electrode is always a cathode which is capable of reducing other gaseous contaminants such as O₂ and N₂. Therefore, the e-CO₂RR process should be preceded by the removal of air from the cathodic chamber. Subsequently, to accurately determine the products formed during the e-CO₂RR, it is inevitable to saturate the cathodic chamber with high purity CO2. The electrolyte is generally KHCO3 and the counter-electrode (anode in this case) is graphite or a carbon electrode. In several cases, researchers have demonstrated the e-CO2RR in KOH medium in order to elevate the pH, and, thereby, suppress the reduction of protons/water (hydrogen evolution). However, saturation of the KOH electrolyte with CO2 reduces its pH due to the spontaneous formation of K2CO3 and KHCO3. Although the pH is maintained between 6.8 and 7.5 under normal conditions, the exact pH of the medium should be monitored to correctly convert the potential vs. reference electrode (commonly, a pre-calibrated Ag/AgCl or SCE) to the potential vs. reversible hydrogen electrode (RHE). The reference electrode is placed in the cathode chamber of the H-cell. The working electrode should be kept protected from metal impurities present in the electrolyte, such as that of Fe and Zn, in order to avoid poisoning and severe deterioration of the catalytic performance. For this, the aqueous electrolyte can be preelectrolyzed so as to eradicate the contaminants by depositing them on a sacrificial cathode.210 Chelex is another option to prevent metal ion deposition due to its chelating action. The current densities that are reported for electrochemical experiments such as CV, LSV etc. should be normalized with respect to the electrochemical surface area (ECSA), which can be calculated as per an earlier report.211 To evaluate the faradaic efficiencies (FE) of various electrocatalysts, the aforesaid electrochemical measurements are generally correlated with the

chromatograms obtained from GC (gas chromatography) and/ or HPLC (high-performance liquid chromatography) of the product mixtures. A bulk-electrolysis experiment should be carried out for about an hour to obtain products that are enough for further analysis.²¹² It is wise to carry out experiments under potentiostatic conditions to avoid deviations from the product selectivity. Galvanostatic experiments are likely to generate potentials that are not suitable for the e-CO₂RR, or can generate a variety of products. However, the latter may be preferred only under certain special conditions where the working electrode is studied well in advance and the applied current is precise for scaling up e-CO₂RR processes.²⁰⁹ The complexity of e-CO₂RR experiments, therefore, lies in the varied physical states of the products that are generated in the reaction medium. In the separate evaluation of the FE for various products, the faradaic selectivity or faradaic yield, defined as the fraction of the FE for a given product with respect to the total FE for all products, should also be calculated and reported. For the analysis of the H2 gas which is invariably evolved during e-CO2RR experiments due to very close potentials, the evolving gases should be directly delivered to the sampling loop of an online gas chromatograph equipped with a thermal conductivity detector (TCD) using argon as the inert carrier gas. Besides, a flame ionization detector (FID) should be used to analyze the possible carbon-containing gaseous products such as CO, CH₄, C₂H₄, and C₂H₆ as described in the mechanistic pathway (Scheme 17). On identification of the constituents present in the liquid (e.g., HCOOH, CH₃OH, and C₂H₅OH) and gaseous mixtures, the selectivity of the product can be evaluated. Relevantly, nuclear magnetic resonance (NMR) spectroscopy and mass spectroscopy (MS) are often used to confirm the associated products. However, to minimize interfering proton signals arising from the aqueous electrolyte, a solvent-suppression method (suppresses the solvent peak, such as water) and deuterium locking (usually done to every NMR sample before acquisition of the spectra) should be necessarily adopted during NMR measurements. 209 As the mechanistic pathway involved in the catalysis over a given heterogeneous surface may be completely changed with the change in the nanoarchitecture of various carbon-based electrodes, structural characterizations of the electrode materials are also important. These include Fourier transform-infrared (FT-IR) spectroscopy, Raman spectroscopy, X-ray diffraction measurements (XRD), X-ray photoelectron spectroscopy (XPS), X-ray absorption near-edge spectroscopy (XANES), X-ray absorption fine structure (XAFS), scanning electron microscopy (SEM), transmission electron microscopy (TEM) and aberrationcorrected-scanning transmission electron microscopy (AC-STEM). Even when coupled with active metallic catalyst nanoparticles, various carbon materials may often be seen generating very different products than what can be expected from the purely metallic catalysts. Hence, it is important to understand the structure-activity relationships of the active catalysts with the reactant and product molecules. For detailed analyses of these processes, in situ techniques are often used. To understand the source of CO2 especially with carbon-based electrocatalysts or

Table 4 Electrocatalysts and electrocatalytic parameters of the CO₂ reduction reaction

E. no.	Electrocatalyst	Electrolyte	Major product (F.E.%, optimal potential)	Onset potential	Ref.
1.	2D-pg-C ₃ N ₄	2 M NaHCO ₃	CO (~80%, −0.35 V νs. RHE)	−0.13 V (vs. RHE)	214
2.	Au–BCN _{3.0} (gold decorated boron-doped carbon nitride)	0.5 M NaHCO ₃	Ethanol (78%)	0.15 V (νs. Ag/AgCl)	215
3.	BCN _{3.0} (boron-doped carbon nitride)	0.5 M NaHCO ₃	Ethanol (47%)	0.15 V (vs. Ag/AgCl)	217
4.	$g-C_3N_4/MWCNT$	0.5 M NaHCO ₃	CO (\sim 60%, -0.75 V vs. RHE)	_	217
5.	Cu-C ₃ N ₄	0.1 M KHCO_3	_ `	_	219
6.	Au/C_3N_4	0.5 M KHCO_3	CO (90%, -0.45 V vs. RHE)		220
7.	Au-CDot-C ₃ N ₄	0.5 M KHCO_3	CO (79.8%)	-0.3 V	221
8.	OA-PCN (hydroxyl and amino functionalized polymeric carbon nitride)	0.5 M NaHCO ₃	CO (40.1%)	-0.56 V	222

electrode materials/substrates, it is often important to carry out isotopic ¹³C-labelling experiments where ¹³CO₂ is used as the feed gas instead of CO₂. Since the focus of this article is on C₃N₄-based electrodes that have been studied for CO₂ utilization to date, a relevant discussion in the said direction is imperative. Studies related to other carbon-based materials or carbon-free catalysts have however been regarded to exist beyond the scope of the present article.

6.2 Impact of g-C₃N₄ as an interesting e-CO₂RR catalyst

In recent times, heteroatom doping in carbon materials has evolved as an interesting domain of research to fine-tune their catalytic performances. For example, Sagara et al. have reported a boron-doped g-C₃N₄ photocathode catalyst that produces ethanol as the major product from CO2 in an aqueous phase with or without the loading of metal nanoparticle co-catalysts Au, Ag or Rh for activity enhancement. It has been generally understood through this study that the enhanced production of ethanol is an outcome of restrained recombination of C1 moieties and the increased selectivity owing to metal nanoparticle loading could be due to the multi-electron reduction by electron capture on metal particles. 213 However, CO is generally the major product when Au or Ag is used as the catalyst, whereas alcohols are formed over Cu electrocatalysts. 214 Zhang et al. have reported a polarized few-layer metal-free g-C3N4 electrocatalyst that can selectively form CO (with trace HCOOH) from CO₂ with a high faradaic efficiency (F.E.) of ~80% (Table 4, entry 1).214 This electrocatalyst has been prepared using hydrothermal pre-treatment of dicyandiamide followed by thermal exfoliation to reduce the number of stray basic sites. This catalyst is able to suppress the hydrogen evolution reaction and, thereby, efficiently catalyze CO₂ reduction. The authors have argued that the large surface area and mesoporous structure of the benchmark photocatalyst mpg-C₃N₄ (mesoporous graphitic carbon nitride) are not capable of electroreduction of CO2 whereas the hierarchical structure of the foam-like monolith composed of 2D-pg-C3N4 is proven to facilitate the diffusion of carbon dioxide molecules to the active surface of the catalyst. Electrochemical impedance spectroscopy, further, has justified the improved mass transfer efficiency of 2D-pg-C₃N₄ exhibiting a larger slope in the low-frequency range (Table 4, entry 2). 215 This result is better than an earlier report on a metal-free g-C₃N₄/MWCNT electrocatalyst that converts CO₂ to CO. Of the total 98% faradaic efficiency obtained for H2 and CO,

H₂ accounts for 58% of the total FE, while that of CO is only 41% (Table 4, entry 3). 216 Zhao et al. on the other hand have reported a ternary Au-CDot-C₃N₄ electrocatalyst with 4 wt% Au that can reduce CO_2 to CO selectively with an F.E. of ~79.8% at a potential of -0.5 V (vs. RHE). Employing theoretical calculations, the authors have proven the importance of the interaction between the CDots and C₃N₄. The authors have suggested the enhancement of the catalytic activity to be a direct outcome of the superior adsorption capability of CDots for both H⁺ and CO₂. A narrower bandgap of 1.35 eV due to the newly introduced valence band maximum has been observed in CDot-C3N4 in contrast to pure g-C₃N₄ (1.92 eV). Again, with the introduction of AuNPs, the electrocatalyst Au-CDot-C₃N₄ has shown a further decrease in the bandgap to 0.32 eV (Table 4, entry 3). 216 Also, adsorption studies have shown better capability of the 4 wt% Au-CDot-C₃N₄ electrocatalyst to adsorb both CO₂ (~ 0.34 mmol g⁻¹ at 1.2 atm) and H^+ (0.37 g g^{-1} , on the basis of HCl) in comparison to 4 wt% Au-C₃N₄ (~ 0.22 mmol g⁻¹ at 1.2 atm of CO₂ and 0.18 mmol g⁻¹ of H⁺ on the basis of HCl) affirming the necessity of CDot incorporation (Table 4, entry 3).217 Employing Cu as the most widely investigated probe for CO₂ reduction, Jiao et al. have studied g-C₃N₄ as a molecular scaffold that appropriately modifies the electronic structure of Cu in the resultant Cu-C₃N₄ complex. Through a combination of DFT computation and experimental justification, their work contributes to understanding the high selectivity of the e-CO2RR toward hydrocarbons/alcohols. The existence of 'mock chemisorption' on the nitrogen atom of the C₃N₄ scaffold is suggested in the study, where CO2 is adsorbed through a carbon-nitrogen bond on Cu-C₃N₄. This is believed to afford Cu-C₃N₄ to activate CO₂ with the application of a suitable electrode potential. Further, the C-centres of the C₃N₄ framework are shown to have a higher ability to bind with species that ligate using oxygen atoms such as *OCH₂, *OCH₃, *O, and *OH. This is due to the electrophilicity in the C-atoms of C₃N₄, which are connected to nitrogen atoms with high electronegativity. Moreover, the Cu active site is shown to have a higher preference to bind with intermediates, *COOH, *CO and *CHO, that use the C-centre for coordination. This kind of dual active center model has been demonstrated to uplift copper's d-orbital position toward the Fermi level, which is critical in adsorbing the intermediate for CO2 activation. Their work successfully validates the formation of C2 products with the presence of two catalytically active centers (Table 4, entry 4).218 In contrast to this mechanism for CO2 activation,

Materials Advances

et al. have unraveled the intriguing role of nitrogen species (Table 4, entry 8). From the perspective of consistency, the carbon framework during the electroreduction of CO_2 reproducibility and ease of synthesis, C_3N_4 -based materials

Xu et al. have unraveled the intriguing role of nitrogen species in the carbon framework during the electroreduction of CO2 (Table 4, entry 5).219 They have enumerated the activity of four types of N-species present in N-doped carbon nanotubes: pyrrolic, pyridinic, and quaternary nitrogen. A conjugated outcome of systematic DFT calculations and experimental observations suggested that the improved activity in N-doped CNTs, in contrast to undoped CNTs, is due to the stabilization of the key intermediate $CO_2^{-\bullet}$. The best correlation is found to be the presence of quaternary N-species (Table 4, entry 5).²¹⁹ Recently, Zhang et al. have corroborated that carbon nitride supported Au nanoparticles (Au/C₃N₄) are better for CO₂ electroreduction than carbon-supported Au nanoparticles (Au/C). This is consistent with an earlier report²²⁰ and the study has been extended to the interaction of Ag with C₃N₄. Experimental and theoretical data prove that C₃N₄ intensifies the electron-density over the Au surface, strengthening the adsorption of key reaction intermediate *COOH. The F.E. for CO is found to be maintained above 90% over a wide potential window of -0.45 V to -0.85 V vs. RHE for Au/C₃N₄, while that for Au/C is always lesser than 80% in this range (Table 4, entry 6).²²⁰ This result is comparable to a recently reported electrocatalyst Au-Py-CNT-O which reportedly reduces CO2 to CO with 93% F.E. over a wide potential range (-0.58 to -0.98 V) (Table 4, entry 7). 221 Meng et al., in a recent report, have shown that a surface-modification strategy to introduce hydroxyl and amino groups on polymeric carbon nitride (PCN) can successfully be used to develop a metal-free electrocatalyst which is able to enhance the CO yield rate 17.1-fold as compared to its unmodified counterpart. The modification process has been carried out by treating PCN at 520 °C for 6 h in a controlled airflow to obtain O-PCN (PCN containing only hydroxyl species). Further, for 1 h O-PCN has been annealed in an NH₃ atmosphere to obtain OA-PCN (containing amino groups along with hydroxyl groups). The catalytic efficiency of OA-PCN towards CO₂ electroreduction is compared with that of A-PCN (containing only amino groups), O-PCN, and PCN. It is observed that the introduction of surface hydroxyl or amino groups alone cannot boost the e-CO2RR rate but the one with both functional groups has been found to suppress hydrogen evolution, thereby enhancing the rate of CO production. The CO/H2 ratio for the OA-PCN electrocatalyst is determined to be 0.67, which is in the range for the Fischer-Tropsch reaction (0.25-3.34). To investigate the ostensibly magical role of dual functionalization of PCN in the e-CO₂RR, density functional theory (DFT) calculations have been carried out. It is revealed that the conversion of CO2 to COOH* possessed the highest energy barrier of 0.62 eV at the NH₂ terminal. Furthermore, a higher barrier of 0.83 eV is required, at the -OH terminal, to desorb the CO product. Therefore, mono-functionalization does not boost the overall performance. However, according to the theoretical calculations, it is possible to infer that a proton-electron transfer process initiates the generation of the *COOH intermediate at the -OH terminal, which is transferred to the -NH2 terminal and, then, converted to *CO. The more facile desorption of the CO product is believed to occur at the -NH2 terminal, thereby exhibiting a fascinatingly high performance of the dual functionalized OA-PCN electrocatalyst

(Table 4, entry 8).²²² From the perspective of consistency, reproducibility and ease of synthesis, C₃N₄-based materials should, therefore, be advocated as efficient potential electrocatalysts for CO₂ reduction.

7. Overall summary, conclusions, and future perspectives

In summary, this article covered three important CO_2 conversion processes, thermal CO_2 activation, photocatalytic CO_2 conversion, and electrochemical CO_2 reduction, focused on the rising star carbonaceous material 'g-C₃N₄'. A summary indicating the general characteristics, advantages, and disadvantages of the thermocatalytic/photocatalytic/electrocatalytic CO_2 conversion process is provided in Table 5.

The merits of g-C₃N₄ for the above mentioned processes are: (a) It is a thermally stable, non-toxic, easy to synthesize material at moderate temperature (550 °C), whereas other carbon-based catalysts need high temperature (1200-1400 °C) and also require chemical activation. (b) In contrast to other carbon materials, N-doped carbon materials, especially g-C₃N₄, are more effective for acidic CO2 activation and conversion. Tailored synthesis parameters, varied carbon and nitrogen precursors, and different synthesis strategies allowed us to synthesize g-C₃N₄ with different types of N species having Lewis and Brønsted basic sites (uncondensed -NH2) suitable for CO2 activation and utilization. Moreover, it is also possible to incorporate other functional sites in g-C₃N₄ so that a multifunctional catalyst for the appointed CO₂ activation reactions can be designed to deliver a designated product. (c) g-C₃N₄ is the only carbon catalyst having a bandgap energy with appropriate valence and conduction band edge potentials for the utilization of visible light of the solar spectrum. It can reduce CO₂ and oxidize H₂O simultaneously and thus effectively serve in the CO2 photoreduction reaction. Except for carbon dots, all other carbons do not have any bandgap and, therefore, are photocatalytically inactive for the CO2 reduction reaction. However, carbon dots cannot themselves trigger CO₂ reduction; instead, they need another support material eventually to exhibit their up-conversion photoluminescence property. (d) It is easy to functionalize g-C3N4 to improve the visible-light harnessing capability, which is not possible with other carbonaceous materials.

Some of the demerits of g- C_3N_4 are: (a) It is thermally stable, but it is prone to light-induced framework oxidation/decomposition. If CO_2 is a reactant, then it requires deep investigation because the framework oxidation/decomposition product and CO_2 derived product could give misleading information. Therefore, integrating g- C_3N_4 with another semiconductor is necessary to stop its framework degradation caused by light absorption. (b) It contains less oxygen in the form of hydroxyl groups, which is not enough to make it a steam reforming chemical looping catalyst. (c) It has low electrochemical conductivity and thus exhibits inferior activity for electrocatalytic CO_2 reduction. Moreover, in the absence of an

 Table 5
 Summary of the thermocatalytic/photocatalytic/electrocatalytic CO₂ conversion process

Process	General characteristics	Advantages	Disadvantages
Thermocatalytic	(1) Thermal energy is the driving force to disrupt the stable atomic and molecular bonds of CO ₂ and other reactants over a bi-functional catalyst to produce various platform chemicals and fuels.	(1) Easy to implement in large scale production.	(1) Not sustainable due to the involvement of a non-renewable energy source.
	(2) Industrially available high-pressure liquid phase and gas phase reactors can be employed to convert CO ₂ to important feedstock chemicals and fuels under the influence of mild to high CO ₂ pressure (1–500 bar or so).	(2) A variety of chemicals and building blocks can be produced.	(2) The trade-off between conversion and energy efficiency is very low.
	(3) Catalysts can be easily designed for the appointed applications.	(3) Catalyst recovery is easy.	(3) The requirement of high pressure and temperature.
		(4) More than 90% of CO_2 is converted <i>via</i> this process.	(4) Pure CO ₂ gas is required.
		(5) Can be applied in a broad range of pressure (1-500 bar or so).(6) Thermodynamic and kinetic parameters can be easily tuned.	(5) Atmospheric CO_2 gas cannot be converted.
Photocatalytic	(1) The driving force is light-energy under ambient conditions to bring down the thermodynamic constraint of stable CO ₂ molecules over a semiconductor photocatalyst having efficient photon capturing ability.	(1) Light energy is available abundantly.	(1) A custom-made catalytic reactor coupled with a suitable light source makes the process less user-friendly.
	(2) It depends on the chemisorption magnitude of CO_2 at $[P/P_0 = 1]$.	(2) Eco-friendly and sustainable process.	(2) Low light-harnessing and quick charge carrier recombination of the photocatalyst are a major drawback.
	(3) The design of a photocatalyst is more-challenging than the thermocatalytic process.	(3) A selective product can be achieved since one-pot CO ₂ reduction and H ₂ O oxidation takes place.	(3) Product isolation and separation are comparatively tough.
	process.	(4) The source of CO ₂ can be varied and, accordingly, different products can be achieved.	(4) Mechanistic investigation is somewhat difficult.
		(5) Recyclability is high if a powder suspension system is employed.	(5) The competitive reduction tendency between CO ₂ and H ⁺ by the light-induced electrons suppresses the overall activity. (6) Large-scale implementation and night time operation are not possible due to the absence of sunlight. (7) Only low CO ₂ pressure can be employed (<10 bar). (8) Atmospheric CO ₂ gas cannot be converted.
Electrocatalytic	(1) A suitable external potential is a driving force (under ambient conditions) to bring down the thermodynamic constraint of a stable CO ₂ molecule over a highly electrochemically conductive electrocatalyst.	(1) Easy to operate.	(1) It is extremely difficult to design the electrocatalytic reactor.
	(2) Mainly carried out under alkaline solution as a CO ₂ source.	(2) Eco-friendly and sustainable process.	(2) An appropriate membrane is difficult to synthesize.
	(3) Electrolyte and potential bias both play a key role.	(3) Highly economic.	(3) A redox-active metal is required owing to its inherent redox properties.
	(4) The design of an electrocatalyst is highly challenging.	(4) The trade-off between conversion and energy efficiency is very high.(5) Product selectivity can be finely tuned.	(4) Catalyst recovery is very difficult if a thin-film is used.(5) Product quantification from a basic medium by GC, GC-MS, and HPLC leads to low yield.
		 (6) Less dependent on the CO₂ chemisorption process. (7) The liquid phase reaction medium is primarily followed. (8) High turnover number (TON) and turnover frequency (TOF). 	 (6) Only low CO₂ pressure can be employed (<10 bar). (7) Atmospheric CO₂ gas cannot be converted. (8) Mechanistic investigation is difficult.

Materials Advances Review

active metal, it exhibits limited redox activity in electrochemical CO₂ reduction. Other carbonaceous materials, primarily N-doped carbons, are more suitable for electrochemical CO2 reduction owing to their superior electronic conductivity. (d) Porous carbon can be derived from any natural resources, but specific carbon and nitrogen-containing precursors are required for g-C₃N₄ synthesis. Moreover, it is a visible light active catalyst and cannot cover the UV and NIR regions of the solar spectrum, which is also a drawback for its limited photocatalytic CO2 reduction activity.

The most crucial feature of g-C₃N₄ is its facile synthesis, which can be performed without any complex synthesis setup. But plenty of research is required to improve its catalytic CO₂ conversion efficiency. g-C₃N₄ exhibited activity in all these three processes but with limited efficiency. For example, thermal CO₂ activation needs high temperature and pressure, which is not sustainable. Moreover, the involvement of an added co-catalyst raises the question of its effectiveness. Integrating an alkali metal oxide with the g-C₃N₄ framework can enhance CO₂ adsorption and activation. Therefore, further improvement of g-C₃N₄ based catalysts is required for CO₂ ambient condition activation and utilization. Since g-C₃N₄ does not have enough oxygen content, integrating it with transition metal oxides like CeO₂ and MnO₂, or spinel based oxides like NiCo₂O₄ with high oxygen exchange capacity can make it an active catalyst for steam reforming of methane coupled with the CO2 splitting reaction. In the case of photocatalytic CO₂ reduction, the target of mole scale product yield is not yet achieved. Moreover, selectivity control and inclusion of additional organic additives like acetonitrile and dimethylformamide, and sacrificial agents like triethanolamine along with a co-catalyst are the serious drawbacks of this photocatalytic process. It is noteworthy that an ideal CO₂ photoreduction system involves a light-harvesting material, CO₂ gas, and H₂O only. But very rarely has this target been served by this catalyst to date. Another controversial aspect is the source of carbon in the converted product during CO₂ photo-reduction, especially when the catalyst itself is a carbonbased material. Utilization of suitable precursors during thermal polymerization (or other synthesis strategies) can incorporate required C, N, O, or S functionalities that have the capability to alter its solar light harnessing capability and can improve the charge carrier separation suitable for high photocatalytic CO₂ reduction reaction activity. Another vital area is the configuration of thin-film based-device fabrication for practical CO₂ photoreduction. g-C₃N₄ has a triazine skeleton, and therefore single-metal-atoms can be entrapped in the framework via wet impregnation followed by thermal annealing in a reducing environment. It will minimize attrition and deactivation, which are advantages for catalyst long term stability. High overpotential, low current densities, and limited redox-tunability are the shortcomings in its electrochemical CO₂ reduction application. Therefore these concerns should be carefully considered for its further efficiency improvement. Carbon nitride-based singleatom-catalysts can be a viable solution to improve photocatalytic, electrocatalytic, or photoelectrocatalytic CO₂ reduction.

We have concisely covered almost all the parameters starting from the synthesis of materials to fundamentals of CO2

activation, followed by critical operational parameters for collective 'thermo-photo-electro'-chemical CO₂ conversion focusing on the g-C₃N₄ catalyst. The conclusion section has provided the details of the merits and demerits of g-C3N4 along with a concise perspective on the application of carbon nitride for CO₂ conversion. We envisage that this review will be helpful for beginners in their early stage of research on heterogeneous CO2 conversion reactions for further technological advancement in the 21st century.

Author contributions

The theme of the review article was proposed by SS and RS jointly. The manuscript was co-written by S. S. and R. S. The authors thank Mr Aniruddha Mukherjee for the preparation of some figures and helpful discussion and drafting the electrochemical section. All the authors proofread and approved the final version of the manuscript.

Conflicts of interest

The authors state that no competitive and non-competitive conflicts of interest exist to declare. The authors also declare that some of the figures included in this manuscript have been prepared by themselves with the appropriate citations wherever it is applicable. Copyright permission has been obtained for the required figures of this manuscript.

Acknowledgements

RS is grateful to the Director IIT Ropar for the Mid-career Excellence in Research through grant number 9-35/2009/IITRPR/ 3121. SS acknowledges the research fellowship received from the Ministry of Human Resource Development, New Delhi, and Director's Fellowship, IIT Ropar. We also thank the anonymous reviewers for their critical comments for the quality improvement of our review article.

References

- 1 G. Savulich, F. H. Hezemans, V. G. Grothe, J. Dafflon, N. Schulten, A. B. Brühl, B. J. Sahakian and T. W. Robbins, Transl. Psychiatry, 2019, 9, 296.
- 2 https://www.ipcc.ch/report/2019-refinement-to-the-2006-ipccguidelines-for-national-greenhouse-gas-inventories/.
- 3 P. W. Barnes, C. E. Williamson and R. M. Lucas, et al., Nat. Sustainability, 2019, 2, 569-579.
- 4 M. G. Lawrence, S. Schäfer, H. Muri, V. Scott, A. Oschlies, N. E. Vaughen, O. Boucher, H. Schmidt, J. Haywood and J. Scheffran, Nat. Commun., 2018, 9, 3734.
- 5 A. V. Herzog, T. E. Lipman and D. M. Kammen. Renewable energy sources, Encyclopedia of life support systems (EOLSS) forerunner volume-perspectives and overview of life support systems and sustainable development, 2001.

Review Materials Advances

- 6 Environmental Impact Comparison of Steam Methane Reformation and Thermochemical Processes of Hydrogen Production G. F. Naterer, O. Jaber, I. Dincer, Detlef Stolten, Thomas Grube (ed.): 18th World Hydrogen Energy Conference 2010 - WHEC 2010 Parallel Sessions Book 3: Hydrogen Production Technologies - Part 2 Proceedings of the WHEC, May 16.-21. 2010, Essen Schriften des Forschungszentrums J,lich/Energy & Environment, Vol. 78-3 Institute of Energy Research-Fuel Cells (IEF-3) Forschungszentrum J,lich GmbH, Zentralbibliothek, Verlag, 2010 ISBN: 978-3-89336-653-8.
- 7 T. P. Senftle and Emily A. Carte, Acc. Chem. Res., 2017, 50, 472-475.
- 8 E. S. Sanz-Perez, C. R. Murdock, S. A. Didas and C. W. Jones, Chem. Rev., 2016, 116, 11840-11876.
- 9 S. A. Didas, S. Choi, W. Chaikittisilp and C. W. Jones, Acc. Chem. Res., 2015, 48, 2680-2687.
- 10 B. Dutcher, M. Fan and A. G. Russell, ACS Appl. Mater. Interfaces, 2015, 7, 2137-2148.
- 11 D. M. Reiner, Nat. Energy, 2016, 1, 15011.
- 12 F. A. Rahman, M. M. A. Aziz, R. Saidur, W. A. Bakar, M. R. Hainin, R. Putrajaya and N. A. Hassan, Renewable Sustainable Energy Rev., 2017, 71, 112-126.
- 13 R. S. Haszeldine, Science, 2009, 325, 1647-1652.
- 14 Q. Wang, J. Luo, Z. Zhong and Z. A. Borgna, Energy Environ. Sci., 2011, 4, 42-55.
- 15 F. Akhtar, Q. Liu, N. Hedin and L. Bergström, Energy Environ. Sci., 2012, 5, 7664-7673.
- 16 D. Bonenfant, M. Kharoune, P. Niquette, M. Mimeault and R. Hausler, Sci. Technol. Adv. Mater., 2008, 9, 013007.
- 17 R. Banerjee, H. Furukawa, D. Britt, C. Knobler, M. O'Keeffe and O. M. Yaghi, J. Am. Chem. Soc., 2009, 131, 3875-3877.
- 18 S. Xiang, Y. He, Z. Zhang, H. Wu, W. Zhou, R. Krishna and B. Chen, Nat. Commun., 2012, 3, 954.
- 19 J. Liu, P. K. Thallapally, B. P. McGrail, D. R. Brown and J. Liu, Chem. Soc. Rev., 2012, 41, 2308-2322.
- 20 J. Wang, A. Heerwig, M. R. Lohe, M. Oschatz, L. Borchardt and S. Kaskel, J. Mater. Chem., 2012, 22, 13911-13913.
- 21 J. Gong, M. Antonietti and J. Yuan, Angew. Chem., Int. Ed., 2017, 56, 7557-7563.
- 22 F. Inagaki, C. Matsumoto, T. Iwata and C. Mukai, J. Am. Chem. Soc., 2017, 139, 4639-4642.
- 23 M. Oschatz, M. Leistner, W. Nickel and S. Kaskel, Langmuir, 2015, 31, 4040-4047.
- 24 V. Presser, J. McDonough, S.-H. Yeon and Y. Gogotsi, Energy Environ. Sci., 2011, 4, 3059-3066.
- 25 W. G. Tu, Y. Zhou and Z. G. Zou, Adv. Mater., 2014, 26,
- 26 J. Lee, D. C. Sorescu and X. Deng, J. Am. Chem. Soc., 2011, 33, 10066-10069.
- 27 E. Karamian and S. Sharifnia, J. CO2 Util., 2016, 16, 194-203.
- 28 R. Srivastava, D. Srinivas and P. Ratnasamy, J. Catal., 2005, 233, 1-15.
- 29 R. Srivastava, D. Srinivas and P. Ratnasamy, Catal. Lett., 2003, 91, 133-139.

- 30 N. Keller, G. Rebmann and V. Keller, J. Mol. Catal. A: Chem., 2010, 317, 1-18.
- 31 J. E. Hallgren, US Pat., US4410464A, 1983.
- 32 S. Fukuoka, M. Kawamura, K. Komiya, M. Tojo, H. Hachiya, K. Hasegawa, M. Aminaka, H. Okamoto, I. Fukawad and S. Konnog, Green Chem., 2003, 5, 497–507.
- 33 Z. Marković, S. Marković, N. Manojlović and J. Predojević-Simović, J. Chem. Inf. Model., 2007, 47, 1520-1525.
- 34 K. C. Waugh, Catal. Today, 1992, 15, 51-75.
- 35 L.-H. Zhang, W.-C. Li, L. Tang, Q.-G. Wang, Q.-T. Hu, Y. Zhang and A.-H. Lu, J. Mater. Chem. A, 2018, 6, 24285–24290.
- 36 G.-P. Hao, Z.-Y. Jin, Q. Sun, X.-Q. Zhang, J.-T. Zhang and A.-H. Lu, Energy Environ. Sci., 2013, 6, 3740.
- 37 Y. Xia, R. Mokaya, G. S. Walker and Y. Zhu, Adv. Energy Mater., 2011, 1, 678-683.
- 38 F. Rodŕguez-reinoso, Carbon, 1998, 36, 159-175.
- 39 X. Shao, Z. Feng, R. Xue, C. Ma, W. Wang, X. Peng and D. Cao, AIChE J., 2011, 57, 3042-3051.
- 40 R. Wang, P. Wang, X. Yan, J. Lang, C. Peng and Q. Xue, ACS Appl. Mater. Interfaces, 2012, 4, 5800-5806.
- 41 J. Chen, J. Yang, G. Hu, X. Hu, Z. Li, S. Shen, M. Radosz and M. Fan, ACS Sustainable Chem. Eng., 2016, 4, 1439-1445.
- 42 R. J. White, V. Budarin, R. Luque, J. H. Clark and D. J. Macquarrie, Chem. Soc. Rev., 2009, 38, 3401-3418.
- 43 C. Robertson and R. Mokaya, Microporous Mesoporous Mater., 2013, 179, 151-156.
- 44 M. Sevilla and A. B. Fuertes, Energy Environ. Sci., 2011, 4, 1765.
- 45 Z. Liu, Z. Zhang, Z. Jia, L. Zhao, T. Zhang, W. Xing, S. Komarneni, F. Subhan and Z. Yan, Chem. Eng. J., 2018, 337, 290-299.
- 46 T.-Y. Ma, L. Liu and Z.-Y. Yuan, Chem. Soc. Rev., 2013, 42, 3977-4003.
- 47 Y. Meng, D. Gu, F. Zhang, Y. Shi, H. Yang, Z. Li, C. Yu, B. Tu and D. Zhao, Angew. Chem., Int. Ed., 2005, 44, 7053-7059.
- 48 Z. Xing, N. Gao, Y. Qi, X. Ji and H. Liu, Carbon, 2017, 115,
- 49 T. Kim, J. Lee and K.-H. Lee, RSC Adv., 2016, 6, 24667–24674.
- 50 Y. Zhao, H. Ding and Q. Zhong, Appl. Surf. Sci., 2012, 258, 4301-4307.
- 51 C. Lu, H. Bai, B. Wu, F. Su and J. F. Hwang, Energy Fuels, 2008, 22, 3050-3056.
- 52 R. Vaidhyanathan, S. S. Iremonger, G. K. H. Shimizu, P. G. Boyd, S. Alavi and T. K. Woo, Science, 2010, 330, 650-653.
- 53 W. Xing, C. Liu, Z. Zhou, L. Zhang, J. Zhou, S. Zhuo, Z. Yan, H. Gao, G. Wang and S. Z. Qiao, Energy Environ. Sci., 2012, 5, 7323-7327.
- 54 D. Qian, C. Lei, E.-M. Wang, W.-C. Li and A.-H. Lu, ChemSusChem, 2014, 7, 291-298.
- 55 J. V. Liebig, Ann. Pharm., 1834, 10, 10.
- 56 F. Goettmann, A. Fischer, M. Antonietti and A. Thomas, Chem. Commun., 2006, 4530-4532.
- 57 X. Wang, K. Maeda, A. Thomas, K. Takanabe, G. Xin, J. M. Carlsson, K. Domen and M. Antonietti, Nat. Mater., 2009, 8, 76-80.

58 D. M. Teter and R. J. Hemley, Science, 1996, 271, 53-55.

Materials Advances

- 59 A. Thomas, A. Fisher, F. Goettmann, M. Antonietti, J. O. Muller, R. Schlogl and R. Carlsson, *J. Mater. Chem.*, 2008, 18, 4893–4908.
- 60 E. Kroke, M. Schwarz, E. Horath-Bordon, P. Kroll, B. Noll and A. D. Norman, *New J. Chem.*, 2002, **26**, 508–512.
- 61 B. Jurgens, E. Irran, J. Senker, P. Kroll, H. Muller and W. Schnick, *J. Am. Chem. Soc.*, 2003, **125**, 10288–10300.
- 62 F. R. Pomilla, M. A. L. R. M. Cortes, J. W. J. Hamilton, R. Molinari, G. Barbieri, G. Marcì, L. Palmisano, P. K. Sharma, A. Brown and J. A. Byrne, *J. Phys. Chem. C*, 2018, 122, 28727–28738.
- 63 C. Chen, J. Kim and W.-S. Ahn, Fuel, 2012, 95, 360-364.
- 64 B. Zhu, K. Li, J. Liu, H. Liu, C. Sun, C. E. Snape and Z. Guo, *J. Mater. Chem. A*, 2014, **2**, 5481–5489.
- 65 P. P. Sharma, J. J. Wu, R. M. Yadav, M. J. Liu, C. J. Wright, C. S. Tiwary, B. I. Yakobson, J. Lou, P. M. Ajayan and X. D. Zhou, *Angew. Chem., Int. Ed.*, 2015, 54, 13701–13705.
- 66 S. Ni, Z. Y. Li and J. L. Yang, Nanoscale, 2012, 4, 1184-1189.
- 67 M. Sevilla, P. Valle-Vigon and A. B. Fuertes, *Adv. Funct. Mater.*, 2011, **21**, 2781–2787.
- 68 J. Zhou, W. Li, Z. Zhang, W. Xing and S. Zhuo, *RSC Adv.*, 2012, 2, 161–167.
- 69 X. Wang, K. Maeda, A. Thomas, K. Takanabe, G. Xin, J. M. Carlsson, K. Domen and M. Antonietti, *Nat. Mater.*, 2009, 8, 76–80.
- 70 S. C. Yan, Z. S. Li and Z. G. Zou, *Langmuir*, 2009, 25, 10397–10401.
- 71 Y. Zhang, J. Liu, G. Wu and W. Chen, *Nanoscale*, 2012, 4, 5300–5303.
- 72 Z. Mo, X. She, Y. Li, L. Liu, L. Huang, Z. Chen, Q. Zhang, H. Xu and H. Li, *RSC Adv.*, 2015, 5, 101552–101562.
- 73 D. Hollmann, M. Karnahl, S. Tschierlei, K. Kailasam, M. Schneider, J. Radnik, K. Grabow, U. Bentrup, H. Junge and M. Beller, *Chem. Mater.*, 2014, 26, 1727–1733.
- 74 F. Dong, Z. Wang, Y. Sun, W.-K. Ho and H. Zhang, J. Colloid Interface Sci., 2013, 401, 70-79.
- 75 P. Niu, L. Zhang and G. Liu, Adv. Funct. Mater., 2012, 22, 4763-4770.
- 76 F. He, G. Chen, Y. Zhou, Y. Yu, Y. Zheng and S. Hao, *Chem. Commun.*, 2015, 51, 16244–16246.
- 77 B. Long, J. Lin and X. Wang, J. Mater. Chem. A, 2014, 2, 2942–2951.
- 78 P. Niu, L.-C. Yin, Y.-Q. Yang, G. Liu and H.-M. Cheng, *Adv. Mater.*, 2014, **26**, 8046–8052.
- 79 S. Yang, Y. Gong, J. Zhang, L. Zhan, L. Ma, Z. Fang, R. Vajtai, X. Wang and P. M. Ajayan, *Adv. Mater.*, 2013, 25, 2452–2456.
- 80 T. Sano, S. Tsutsui, K. Koike, T. Hirakawa, Y. Teramoto, N. Negishi and K. Takeuchi, *J. Mater. Chem. A*, 2013, **1**, 6489–6496.
- 81 J. Tong, L. Zhang, F. Li, M. Li and S. Cao, *Phys. Chem. Chem. Phys.*, 2015, **17**, 23532–23537.
- 82 K. S. Lakhi, D.-W. Park, K. Al-Bahily, W. Cha, B. Viswanathan, J.-H. Choy and A. Vinu, *Chem. Soc. Rev.*, 2017, **46**, 72–101.

- 83 F. Goettmann, A. Fischer, M. Antonietti and A. Thomas, *Angew. Chem., Int. Ed.*, 2006, 45, 4467–4471.
- 84 Y.-S. Jun, W. H. Hong, M. Antonietti and A. Thomas, *Adv. Mater.*, 2009, **21**, 4270–4274.
- 85 J. Zhang, F. Guo and X. Wang, Adv. Funct. Mater., 2013, 23, 3008–3014.
- 86 Y. Wang, X. Wang and M. Antonietti, *Angew. Chem., Int. Ed.*, 2012, **51**, 68–89.
- 87 J. Wang, C. Zhang, Y. Shen, Z. Zhou, J. Yu, Y. Li, W. Wei, S. Liu and Y. Zhang, J. Mater. Chem. A, 2015, 3, 5126–5131.
- 88 W. Shen, L. Ren, H. Zhou, S. Zhang and W. Fan, *J. Mater. Chem.*, 2011, 21, 3890–3894.
- 89 Y. Wang, X. Wang, M. Antonietti and Y. Zhang, *Chem-SusChem*, 2010, 3, 435–439.
- 90 Y. Wang, J. Zhang, X. Wang, M. Antonietti and H. Li, *Angew. Chem., Int. Ed.*, 2010, **49**, 3356–3359.
- 91 Y.-S. Jun, E. Z. Lee, X. Wang, E. W. Hong, G. D. Stucky and A. Thomas, *Adv. Funct. Mater.*, 2013, 23, 3661–3667.
- 92 M. Shalom, M. Guttentag, C. Fettkenhauer, S. Inal, D. Neher, A. Llobet and M. Antonietti, *Chem. Mater.*, 2014, 26, 5812–5818.
- 93 Y. Liao, S. Zhu, J. Ma, Z. Sun, C. Yin, C. Zhu, X. Lou and D. Zhang, *ChemCatChem*, 2014, **6**, 3419–3425.
- 94 T. Jordan, N. Fechler, J. Xu, T. J. K. Brenner, M. Antonietti and M. Shalom, *ChemCatChem*, 2015, 7, 2826–2830.
- 95 J. Li, B. Shen, Z. Hong, B. Lin, B. Gao and Y. Chen, *Chem. Commun.*, 2012, **48**, 12017–12019.
- 96 Z.-F. Huang, J. Song, L. Pan, Z. Wang, X. Zhang, J.-J. Zou, W. Mi, X. Zhang and L. Wang, *Nano Energy*, 2015, 12, 646–656.
- 97 Z. Zhao, Y. Sun, F. Dong, Y. Zhang and H. Zhao, *RSC Adv.*, 2015, 5, 39549–39556.
- 98 S. Hu, L. Ma, J. You, F. Li, Z. Fan, F. Wang, D. Liu and J. Gui, *RSC Adv.*, 2014, **4**, 21657–21663.
- 99 Y. Zhou, L. Zhang, J. Liu, X. Fan, B. Wang, M. Wang, W. Ren, J. Wang, M. Li and J. Shi, *J. Mater. Chem. A*, 2015, 3, 3862–3867.
- 100 J. Ran, T. Y. Ma, G. Gao, X.-W. Du and S. Z. Qiao, Energy Environ. Sci., 2015, 8, 3708–3717.
- 101 G. Liu, P. Niu, C. Sun, S. C. Smith, Z. Chen, G. Q. Lu and H.-M. Cheng, J. Am. Chem. Soc., 2010, 132, 11642–11648.
- 102 K. Wang, Q. Li, B. Liu, B. Cheng, W. Ho and J. Yu, *Appl. Catal.*, *B*, 2015, **176–177**, 44–52.
- 103 J. Zhang, J. Sun, K. Maeda, K. Domen, P. Liu, M. Antonietti, X. Fu and X. Wang, *Energy Environ. Sci.*, 2011, 4, 675–678.
- 104 S. C. Yan, Z. S. Li and Z. G. Zou, *Langmuir*, 2010, 26, 3894–3901.
- 105 Y. Wang, H. Li, J. Yao, X. Wang and M. Antonietti, *Chem. Sci.*, 2011, 2, 446–450.
- 106 H. Li, Y. Liu, X. Gao, C. Fu and X. Wang, *ChemSusChem*, 2015, **8**, 1189–1196.
- 107 S. Samanta and R. Srivastava, Sustainable Energy Fuels, 2017, 1, 1390-1404.
- 108 S. Samanta, R. Yadav, A. Kumar, A. K. Sinha and R. Srivastava, *Appl. Catal., B*, 2019, **259**, 118054.
- 109 Y. Gao, K. Qian, B. Xu, Z. Li, J. Zheng, S. Zhao, F. Ding, Y. Sun and Z. Xu, *Carbon Resour. Convers.*, 2020, 3, 46–59.

110 A. Akhundi, A. Habibi-Yangjeh, M. Abitorabi and S. R. Pouran, *Catal. Rev.*, 2019, **61**, 595–628.

- 111 M. Shen, L. Zhang and J. Shi, *Nanotechnology*, 2018, **29**, 412001.
- 112 C. H. Bartholomew, Chem. Eng., 1984, 91, 96-112.
- 113 J.-S. Chang, V. P. Vislovskiy, M.-S. Park, D. Y. Hong, J. S. Yoo and S.-E. Park, *Green Chem.*, 2003, 5, 587–590.
- 114 M.-O. Sugino, H. Shimada, T. Turuda, H. Miura, N. Ikenaga and T. Suzuki, *Appl. Catal.*, *A*, 1995, **121**, 125–137.
- 115 V. Ansari and S.-E. Park, *Energy Environ. Sci.*, 2012, 5, 9419–9437.
- 116 F. Goettmann, A. Thomas and M. Antonietti, *Angew. Chem., Int. Ed.*, 2007, **46**, 2717–2720.
- 117 M. B. Ansari, B.-H. Min, Y.-H. Mo and S.-E. Park, *Green Chem.*, 2011, 13, 1416–1421.
- 118 X. Lan, Y. Li, C. Du, T. She, Q. Li and G. Bai, *Chem. Eur. J.*, 2019, **25**, 8560–8569.
- 119 A. J. Kamphuis, F. Picchioni and P. P. Pescarmona, *Green Chem.*, 2019, 21, 406–448.
- 120 Z. Huang, F. Li, B. Chen and G. Yuan, *Catal. Sci. Technol.*, 2016, **6**, 2942–2948.
- 121 M. B. Ansari, B.-H. Min, Y.-H. Mo and S.-E. Park, *Green Chem.*, 2011, **13**, 1416–1421.
- 122 Z. Huang, F. Li, B. Chen, T. Lu, Y. Yuan and G. Yuan, *Appl. Catal.*, *B*, 2013, **136–137**, 269–277.
- 123 J. Xu, F. Wu, Q. Jiang, J.-K. Shang and Y.-X. Li, *J. Mol. Catal. A: Chem.*, 2015, **403**, 77–83.
- 124 Q. Su, J. Sun, J. Wang, Z. Yang, W. Cheng and S. Zhang, *Catal. Sci. Technol.*, 2014, 4, 1556–1562.
- 125 J. Xu, F. Wu, Q. Jiang and Y.-X. Li, *Catal. Sci. Technol.*, 2015, 5, 447–454.
- 126 D.-H. Lan, H.-T. Wang, L. Chen, C.-T. Au and S.-F. Yin, *Carbon*, 2016, **100**, 81–89.
- 127 Q. Su, X. Yao, W. Cheng and S. Zhang, Green Chem., 2017, 19, 2957–2965.
- 128 X. Li, B. Lin, H. Li, Q. Yu, Y. Ge, X. Jin, X. Liu, Y. Zhou and J. Xiao, *Appl. Catal.*, *B*, 2018, **239**, 254–259.
- 129 J. Zhu, T. Diao, W. Wang, X. Xu, X. Sun, S. A. C. Carabineiroc and Z. Zhao, *Appl. Catal.*, *B*, 2017, **219**, 92–100.
- 130 T. Biswas and V. Mahalingam, New J. Chem., 2017, 41, 14839–14842.
- 131 Z. Sun, N. Talreja, H. Tao, J. Texter, M. Muhler, J. Strunk and J. Chen, *Angew. Chem., Int. Ed.*, 2018, 57, 7610–7627.
- 132 A. A. Tountas, X. Peng, A. V. Tavasoli, P. N. Duchesne,
 T. L. Dingle, Y. Dong, L. Hurtado, A. Mohan, W. Sun,
 U. Ulmer, L. Wang, T. E. Wood, C. T. Maravelias,
 M. M. Sain and G. A. Ozin, Adv. Sci., 2019, 6, 1801903.
- 133 M. Khalil, J. Gunlazuardi, T. A. Ivandini and A. Umar, Renewable Sustainable Energy Rev., 2019, 113, 109246.
- 134 Z. Wang, C. Li and K. Domen, *Chem. Soc. Rev.*, 2019, **48**, 2109–2125.
- 135 M.-H. Vu, M. Sakar, S. A. Hassanzadeh-Tabrizi and T.-O. Do, *Adv. Mater. Interfaces*, 2019, **6**, 1900091.
- 136 J. Kou, C. Lu, J. Wang, Y. Chen, Z. Xu and R. S. Varma, *Chem. Rev.*, 2017, 117, 1445–1514.

- 137 R. N. Compton, P. W. Reinhardt and C. D. Cooper, *J. Chem. Phys.*, 1975, **63**, 3821–3827.
- 138 N.-N. Vu, S. Kaliaguine and T.-O. Do, *Adv. Funct. Mater.*, 2019, **29**, 1901825.
- 139 K. Li, B. Peng and T. Peng, ACS Catal., 2016, 6, 7485–7527.
- 140 T. Inoue, A. Fujishima, S. Konishi and K. Honda, *Nature*, 1979, 277, 637–638.
- 141 J. Fu, K. Jiang, X. Qiu, J. Yu and M. Liu, *Mater. Today*, 2019, 32, 222–243.
- 142 N. Sasirekha, S. J. S. Basha and K. Shanthi, *Appl. Catal., B*, 2006, **62**, 169–180.
- 143 K. Mori, H. Yamashita and M. Anpo, *RSC Adv.*, 2012, 2, 3165–3172, DOI: 10.1039/C2RA01332K.
- 144 I. A. Shkrob, T. W. Marin, H. Y. He and P. Zapol, *J. Phys. Chem. C*, 2012, **116**, 9450–9460.
- 145 L. B. Hoch, P. Szymanski, K. K. Ghuman, L. He, K. Liao, Q. Qia, L. M. Reyes, Y. Zhu, M. A. El-Sayed, C. V. Singh and G. A. Ozin, *Proc. Natl. Acad. Sci. U. S. A.*, 2016, 113, E8011–E8020.
- 146 W. Tu, Y. Xu, J. Wang, B. Zhang, T. Zhou, S. Yin, S. Wu, C. Li, Y. Huang, Y. Zhou, Z. Zou, J. Robertson, M. Kraft and R. Xu, ACS Sustainable Chem. Eng., 2017, 5, 7260–7268.
- 147 S. C. Bhatia, Advanced Renewable Energy Systems, 2014, pp. 32-67.
- 148 G. M. Hasselman, D. F. Watson, J. R. Stromberg, D. F. Bocian, D. Holten, J. S. Lindsey and G. J. Meyer, *J. Phys. Chem. B*, 2006, 110, 25430–25440.
- 149 S. N. Habisreutinger, L. Schmidt-Mende and J. K. Stolarczyk, *Angew. Chem., Int. Ed.*, 2013, 52, 7372–7408.
- 150 H. Lang, S. Zhang and Z. Liu, *Phys. Rev. B*, 2016, 94, 235306.
- 151 L. Liu, H. Zhao, J. M. Andino and Y. Li, ACS Catal., 2012, 2, 1817–1828.
- 152 X. Chang, T. Wang and J. Gong, *Energy Environ. Sci.*, 2016, **9**, 2177–2196.
- 153 Z. Sun, H. Wang, Z. Wu and L. Wang, *Catal. Today*, 2018, **300**, 160–172.
- 154 J. Chen, Y.-F. Li, P. Sit and A. Selloni, *J. Am. Chem. Soc.*, 2013, **135**, 18774–18777.
- 155 O. Ola and M. M. Maroto-Valer, *J. Photochem. Photobiol., C*, 2015, **24**, 16–42.
- 156 K. Li, X. An, K. H. Park, M. Khraisheh and J. Tang, *Catal. Today*, 2014, **224**, 3–12.
- 157 X. Li, J. Yu, M. Jaroniec and X. Chen, *Chem. Rev.*, 2019, **119**, 3962–4179.
- 158 J. Ran, M. Jaroniec and S.-Z. Qiao, Adv. Mater., 2018, 30, 1704649.
- 159 N. Syed, J. Huang, Y. Feng, X. Wang and L. Cao, *Front. Chem.*, 2019, 7(713), 1–7.
- 160 J. Z. Y. Tan and M. M. Maroto-Valer, *J. Mater. Chem. A*, 2019, 7, 9368–9385.
- 161 L. Wang, W. Chen, D. Zhang, Y. Du, R. Amal, S. Qiao, J. Wu and Z. Yin, Chem. Soc. Rev., 2019, 48, 5310-5349.

162 J. Fu, J. Yu, C. Jiang and B. Cheng, *Adv. Energy Mater.*, 2018, **8**, 1701503.

Materials Advances

- 163 J. K. Stolarczyk, S. Bhattacharyya, L. Polavarapu and J. Feldmann, *ACS Catal.*, 2018, **8**, 3602–3635.
- 164 M. M. Kandy, Sustainable Energy Fuels, 2020, 4, 469-484.
- 165 S. Ye, R. Wang, M.-Z. Wu and Y.-P. Yuan, *Appl. Surf. Sci.*, 2015, **358**, 15–27.
- 166 G. Dong and L. Zhang, J. Mater. Chem., 2012, 22, 1160–1166.
- 167 J. Mao, T. Peng, X. Zhang, K. Li, L. Ye and L. Zan, *Catal. Sci. Technol.*, 2013, 3, 1253–1260.
- 168 P. Niu, Y. Yang, J. C. Yu, G. Liu and H.-M. Cheng, *Chem. Commun.*, 2014, 50, 10837–10840.
- 169 Y.-P. Yuan, S.-W. Cao, Y.-S. Liao, L.-S. Yin and C. Xue, *Appl. Catal.*, *B*, 2013, **140–141**, 164–168.
- 170 K. Maeda, R. Kuriki, M. Zhang, X. Wang and O. Ishitani, *J. Mater. Chem. A*, 2014, **2**, 15146–15151.
- 171 J. Qin, S. Wang, H. Ren, Y. Hou and X. Wang, *Appl. Catal.*, *B*, 2015, **179**, 1–8.
- 172 K. Wang, Q. Li, B. Liu, B. Cheng, W. Ho and J. Yu, *Appl. Catal.*, *B*, 2015, **176–177**, 44–52.
- 173 J. Fu, B. Zhu, C. Jiang, B. Cheng, W. You and J. Yu, *Small*, 2017, **13**, 1603938.
- 174 B. Liu, L. Ye, R. Wang, J. Yang, Y. Zhang, R. Guan, L. Tian and X. Chen, ACS Appl. Mater. Interfaces, 2018, 10, 4001–4009.
- 175 D. Vidyasagar, N. Manwar, A. Gupta, S. G. Ghugal, S. S. Umare and R. Boukherroub, *Catal. Sci. Technol.*, 2019, **9**, 822–832.
- 176 S. Roy and E. Reisner, Angew. Chem., Int. Ed., 2019, 58, 12180-12184.
- 177 H. Shi, S. Long, J. Hou, L. Ye, Y. Sun, W. Ni, C. Song, K. Li, G. G. Gurzadyan and X. Guo, *Chem. Eur. J.*, 2019, 25, 5028–5035.
- 178 M. Li, S. Zhang, X. Liu, J. Han, X. Zhu, Q. Ge and H. Wang, *Eur. J. Inorg. Chem.*, 2019, 2058–2064.
- 179 G. Zhang, G. Li, T. Heil, S. Zafeiratos, F. Lai, A. Savateev, M. Antonietti and X. Wang, *Angew. Chem., Int. Ed.*, 2019, 58, 3433–3437.
- 180 S. Wan, M. Ou, X. Wang, Y. Wang, Y. Zeng, J. Ding, S. Zhang and Q. Zhong, *Dalton Trans.*, 2019, 48, 12070–12079.
- 181 J.-Y. Tang, X. Y. Kong, B.-J. Ng, Y.-H. Chew, A. R. Mohamed and S.-P. Chai, *Catal. Sci. Technol.*, 2019, **9**, 2335–2343.
- 182 J. Fu, K. Liu, K. Jiang, H. Li, P. An, W. Li, N. Zhang, H. Li, X. Xu, H. Zhou, D. Tang, X. Wang, X. Qiu and M. Li, Adv. Sci., 2019, 6, 1900796.
- 183 A. Hayat, J. Khan, M. U. Rahman, S. B. Mane, W. U. Khan, M. Sohail, N. U. Rahman, N. Shaishta, Z. Chi and M. Wu, J. Colloid Interface Sci., 2019, 548, 197–205.
- 184 K. Wang, J. Fu and Y. Zheng, *Appl. Catal.*, *B*, 2019, **254**, 270–282.
- 185 N. Tian, K. Xiao, Y. Zhang, X. Lu, L. Ye, P. Gao, T. Ma and H. Huang, *Appl. Catal.*, *B*, 2019, 253, 196–205.

- 186 X. Liu, P. Wang, H. Zhai, Q. Zhang, B. Huang, Z. Wang, Y. Liu, Y. Dai, X. Qin and X. Zhang, *Appl. Catal., B*, 2018, 232, 521–530.
- 187 S. Wan, M. Ou, Q. Zhong and W. Cai, *Carbon*, 2018, 138, 465–474.
- 188 X. Gong, S. Yu, M. Guan, X. Zhu and C. Xue, *J. Mater. Chem. A*, 2019, 7, 7373–7379.
- 189 H. Ou, C. Tang, Y. Zhang, A. M. Asiri, M.-M. Titirici and X. Wang, J. Catal., 2019, 375, 104–112.
- 190 J.-Y. Tang, W.-G. Zhou, R.-T. Guo, C.-Y. Huang and W.-G. Pan, *Catal. Commun.*, 2018, **107**, 92–95.
- 191 S. Cao, Y. Li, B. Zhu, M. Jaroniec and J. Yu, *J. Catal.*, 2017, 349, 208–217.
- 192 M. Humayun, Q. Fu, Z. Zheng, H. Li and W. Luo, *Appl. Catal.*, *A*, 2018, **568**, 139–147.
- 193 W.-J. Ong, L.-L. Tan, S.-P. Chai and S.-T. Yong, *Dalton Trans.*, 2015, **44**, 1249–1257.
- 194 K. Takanabe, J. Catal., 2019, 370, 480-484.
- 195 P. V. Kamat and S. Jin, ACS Energy Lett., 2018, 3, 622–623.
- 196 Q. Wang and K. Domen, Chem. Rev., 2020, 120, 919-985.
- 197 P. V. Kamat and J. M. Buriak, ACS Energy Lett., 2019, 4, 2473–2474.
- 198 J. M. Buriak, P. V. Kamat and K. S. Schanze, *ACS Appl. Mater. Interfaces*, 2014, **6**, 11815–11816.
- 199 M. Melchionna and P. Fornasiero, *ACS Catal.*, 2020, **10**, 5493–5501.
- 200 J. Albero, Y. Peng and H. García, ACS Catal., 2020, 10, 5734–5749.
- 201 G. Peng, J. Albero, H. Garcia and M. Shalom, *Angew. Chem.*, Int. Ed., 2018, 57, 15807–15811.
- 202 G. Peng, J. Qin, M. Volokh and M. Shalom, ACS Appl. Mater. Interfaces, 2019, 11, 29139–29146.
- 203 G. Peng, J. Qin, M. Volokh, C. Liu and M. Shalom, J. Mater. Chem. A, 2019, 7, 11718–11723.
- 204 Y. Fang, X. Li and X. Wang, ACS Catal., 2018, 8, 8774–8780.
- 205 W. Xiong, F. Huang and R.-Q. Zhang, Sustainable Energy Fuels, 2020, 4, 485–503.
- 206 J. Safaei, N. A. Mohamed, M. F. M. Noh, M. F. Soh, N. A. Ludin, M. A. Ibrahim, W. N. R. W. Isahak and M. A. M. Teridi, J. Mater. Chem. A, 2018, 6, 22346–22380.
- 207 D. D. Zhu, J. L. Liu and S. Z. Qiao, *Adv. Mater.*, 2016, 28, 3423-3452.
- 208 R. J. Lim, M. Xie, M. A. Sk, J. M. Lee, A. Fisher, X. Wang and K. H. Lim, *Catal. Today*, 2014, 233, 169–180.
- 209 J. E. Pander, D. Ren and B. S. Yeo, *Catal. Sci. Technol.*, 2017, 7, 5820–5832.
- 210 Y. Hori, H. Konishi, T. Futamura, A. Murata, O. Koga, H. Sakurai and K. Oguma, *Electrochim. Acta*, 2005, 50, 5354–5369.
- 211 S. Trasatti and O. A. Petrii, *J. Electroanal. Chem.*, 1992, **327**, 353–376.
- 212 A. J. Bard and L. R. Faulkner, *Electrochemical Methods:* Fundamentals and applications, John Wiley & Sons, Inc., 2nd edn, 2001.

213 N. Sagara, S. Kamimura, T. Tsubota and T. Ohno, *Appl. Catal.*, *B*, 2016, **192**, 193–198.

- 214 C. M. S-Sánchez, V. Montiel, D. A. Tryk, A. Aldaz and A. Fujishima, *Pure Appl. Chem.*, 2001, 73, 1917–1927.
- 215 B. Zhang, T.-J. Zhao, W.-J. Feng, Y.-X. Liu, H.-H. Wang, H. Su, L.-B. Lv, X.-H. Li and J.-S. Chen, *Nano Res.*, 2018, 11, 2450–2459.
- 216 X. Lu, T. H. Tan, Y. H. Ng and R. Amal, *Chem. Eur. J.*, 2016, 22, 11991–11996.
- 217 S. Zhao, Z. Tang, S. Guo, M. Han, C. Zhu, Y. Zhou, L. Bai, J. Gao, H. Huang, Y. Li, Y. Liu and Z. Kang, ACS Catal., 2017, 8, 188–197.
- 218 Y. Jiao, Y. Zheng, P. Chen, M. Jaroniec and S.-Z. Qiao, *J. Am. Chem. Soc.*, 2017, **139**, 18093–18100.
- 219 J. Xu, Y. Kan, R. Huang, B. Zhang, B. Wang, K. H. Wu, Y. Lin, X. Sun, Q. Li, G. Centi and D. Su, *ChemSusChem*, 2016, 9, 1085–1089.
- 220 L. Zhang, F. Mao, L. R. Zheng, H. F. Wang, X. H. Yang and H. G. Yang, *ACS Catal.*, 2018, **8**, 11035–11041.
- 221 Z. Ma, C. Lian, D. Niu, L. Shi, S. Hu, X. Zhang and H. Liu, *ChemSusChem*, 2019, **12**, 1724–1731.
- 222 N. Meng, W. Zhou, Y. Yu, Y. Liu and B. Zhang, *ACS Catal.*, 2019, **9**, 10983–10989.